8-2017

Deformation Behavior of Al/a-Si Core-shell Nanostructures

Robert Andrew Fleming
University of Arkansas, Fayetteville

Deformation Behavior of Al/a-Si Core-shell Nanostructures

A dissertation submitted in partial fulfillment
of the requirements for the degree of
Doctor of Philosophy in Engineering

by

Robert Fleming
University of Arkansas
Bachelor of Science in Mechanical Engineering, 2009
University of Arkansas
Master of Science in Mechanical Engineering, 2012

August 2017
University of Arkansas

This dissertation is approved for recommendation to the Graduate Council.

_____
Dr. Min Zou
Dissertation Director

_____
Dr. Douglas Spearot
Committee Member

_____
Dr. Arun Nair
Committee Member

_____
Dr. Po-Hao Adam Huang
Committee Member

_____
Dr. R. Panneer Selvam
Committee Member

ABSTRACT

Al/a-Si core-shell nanostructures (CSNs), consisting of a hemispherical Al core surrounded by a hard shell of a-Si, have been shown to display unusual mechanical behavior in response to compression loading. Most notably, these nanostructures exhibit substantial deformation recovery, even when loaded much beyond the elastic limit. Nanoindentation measurements revealed a unique mechanical response characterized by discontinuous signatures in the load-displacement data. In conjunction with the indentation signatures, nearly complete deformation recovery is observed. This behavior is attributed to dislocation nucleation and annihilation events enabled by the 3-dimensional confinement of the Al core. As the core confinement is reduced, either through an increase in confined core volume or a change in the geometrical confinement, the indentation signatures and deformation resistance are significantly reduced.

Complimentary molecular dynamics simulations show that a substantial amount of dislocation egression occurs in the core of CSNs during unloading as dislocations annihilate at the core/shell interface. Smaller core diameters correlate with the development of a larger back-stress within the core during unloading, which further correlates with improved dislocation annihilation after unloading. Furthermore, dislocations nucleated in the core of core-shell nanorods are not as effectively removed as compared to CSNs.

Nanostructure-textured surfaces (NSTSs) composed of Al/a-Si CSNs have improved tribological properties compared surfaces patterned with Al nanodots and a flat (100) Si surface. NSTSs have a coefficient of friction (COF) as low as 0.015, exhibit low adhesion with adhesion

forces on the order of less than 1 μN, and are highly deformation resistant, with no apparent surface deformation after nanoscratch testing, even at contact forces up to 8000 μN. In comparison, (100) Si has substantially higher adhesion and COF (~10 μN and ~0.062, respectively), while the Al nanodots have both higher friction (COF ~0.044) and are deformed when subjected to contact loads as low as 250 μN.

This integrated experimental and computational study elucidates the mechanisms that contribute to the novel properties of Al/a-Si CSNs and characterizes the tribological properties of surface composed of these nanostructures, which provides a foundation for the rational design of novel technologies based on CSNs.

ACKNOWLEDGEMENTS

This dissertation is the culmination of over 5 years' work to understand the novel mechanical behavior of Al/a-Si core-shell nanostructures, which were initially discovered in the Nanomechanics and Tribology Laboratory (NMTL) in 2009. This work would not have been possible without my advisor, Dr. Min Zou, who provided an incalculable amount of support during my graduate career. Special thanks are also due to Corey Thompson and Sam Beckford, who formed the research core of the NMTL along with myself during much of my studies, and with whom I have been fortunate enough to pursue many other fruitful opportunities in engineering. I would also like to thank Dr. Douglas Spearot, Dr. Arun Nair, Dr. Adam Huang, and Dr. Panneer Selvam for serving on the dissertation committee.

The NMTL has been a vibrant research environment, where I have had access to world-class nanomechanical characterization tools, including nanoindentation and AFM. The nanofabrication work in this study was made possible by Errol Porter and the staff at the High Density Electronic Center, who diligently maintained and provided training on the cleanroom equipment, most notably electron beam lithography and PECVD. Training on the materials characterization equipment by Dr. Mourad Benamara at the Arkansas Nano & Bio Materials Characterization Facility is also greatly appreciated. Much of the sophistication in the molecular dynamics modeling in this work is due to Dr. Spearot, who provided many helpful discussions and ideas over the course of my graduate studies.

Funding support for this work was partially provided by the US National Science Foundation (NSF) under Grant Nos. CMMI-1463306, DGE-0957325, and from the Center for

Advanced Surface Engineering under Grant No. OIA-1457888 and the Arkansas EPSCoR Program, ASSET III. Major equipment funding from the Arkansas Biosciences Institute and the University of Arkansas is acknowledged. This work used the Extreme Science and Engineering Discovery Environment (XSEDE), which is supported by NSF Grant No. ACI-1053575, as well as the Arkansas High Performance Computing Center, under NSF Grant Nos. ARI-0963249, MRI-0959124, and EPS-0918970.

TABLE OF CONTENTS

LIST OF TABLES

LIST OF FIGURES

CHAPTER 1

INTRODUCTION

Core-shell nanostructures (CSNs) are a unique type of nanomaterial composed of a nanoscale internal core surrounded by a shell with a distinct material composition. In principle, both the core and shell components of a CSN can be created from any material, including metals, ceramics, semiconductors, or polymers. This broad range of material combinations allows for the design and fabrication of CSNs that combine the material properties of both the core and shell components. With the right material combinations, CSNs can exhibit improved functional properties compared to single-material nanostructures. Much research interest has been directed toward designing CSNs with properties that are desirable for a variety of applications.

1.1 Background and Motivation

CSNs offer the opportunity to potentially engineer nanostructures with unique mechanical properties. Notable examples of interesting mechanical phenomena enabled by nanoscale materials include strengthening mechanisms in nano-grained metals [1,2], multilayer nanolaminate composites with enhanced hardness [3-5], size effects [6-13], and mechanical annealing and dislocation starvation processes [14,15]. However, nearly all nanomaterials suffer from permanent plastic deformation when subjected to contact loading that reduces their effectiveness in applications. This is due to the nanoscale sizes of these structures and the resulting small contact areas during loading, which allows very high contact pressures to be generated, even at moderate contact loads.

For example, nanopatterned poly(methyl methacrylate) (PMMA) surfaces have been shown to have reduced friction compared to smooth polymer surfaces when subjected to microscale friction tests, but the polymer nanostructures were found to be significantly damaged after testing [16,17]. Similar behavior has also been reported for nanotextured Al surfaces [18], Ni nanodot patterned surfaces [19,20], and amorphous carbon surfaces [21]. In all of these examples, the desirable material properties are compromised by a lack of structural integrity of the individual nanostructures. While this is most commonly an issue when nanostructures are used in nanotextured surfaces for low-friction applications, it is clearly an issue for all nanostructures subjected to contact loading. This severely limits the implementation of nanostructures in applications where the mechanical integrity of the nanostructures is important.

Recently, Al/a-Si CSNs have been discovered to have unique deformation-resistant properties [22]. These CSNs were fabricated from a nanotextured Al thin film that was then conformably coated with a-Si, forming a surface populated with an ensemble of Al/a-Si CSNs. The individual nanostructures were composed of ~200 nm diameter polycrystalline Al nanodots protruding from the Al thin film, which were then coated with a 300 nm a-Si shell. When the CSNs were subjected to load-controlled nanoindentation up to 300 μN, it was found that the structures had a higher yield strength than either Al or a-Si natively and could sustain up to 23% engineering strain without fracture. In addition, these structures exhibited an unconventional mechanical response, consisting of discontinuous indentation signatures referred to as “pop-ins” and “pop-outs” during loading and unloading, respectively. Furthermore, despite the large indenter displacement compared to the size of the CSN, the load-displacement curve shows no residual displacement, which suggests that the nanostructure deformation is completely

recovered during unloading. This recovery is further confirmed by scanning probe microscopy imaging that shows no structure height change after indentation. Nanotribological testing on nanotextured surfaces composed of Al/a-Si CSNs have further confirmed these deformation-resistant properties [18]. When subjected to nanoscratch testing, these surfaces were found to have no detectable nanostructure deformation at contact loads up to 8000 μN, while still maintaining a low coefficient of friction.

Exploratory experiments strongly indicate that dislocation activities within the Al core must be responsible for the unique mechanical behavior exhibited by these structures. More specifically, it is hypothesized that the deformation behavior of these structures is critically dependent on the confinement of the Al core and its effects on the dislocation activities within the core. Additional research is warranted because of the unique mechanical behavior observed in Al/a-Si CSNs. However, the previously reported fabrication method provides little control over the size, shape, location, and density of the nanostructures. To overcome this limitation, a new fabrication method using electron beam lithography (EBL) has been developed to fabricate well-ordered arrays of nanostructures. The deformation behavior of the CSNs has been characterized using instrumented nanoindentation and further characterized with a combination of scanning probe and electron microscopy. The role that geometric confinement of the Al core – defined in terms of either the size of the confined core volume or the "dimensionality" of the confinement – plays on the mechanical behavior of these structures is studied through comparative experiments on hemispherical CSNs with different core sizes and experiments on horizontally-aligned core-shell rods and layered thin films. Complimentary to the experimental investigations, molecular dynamics simulations have been performed to provide insight into the

underlying dislocation dynamics that occur during nanoindentation. The results show that core confinement critically influences the deformation behavior of the CSNs, both in terms of the size of the confined core volume as well as the "dimensionality" of confinement. Deformation-resistant behavior is only observed in hemispherical CSNs with 100 nm core diameters, while an attendant loss of deformation resistance is noted as the core confinement decreases. This integrated experimental and computational investigation clarifies the mechanisms that contribute to the unique deformation-resistant behavior of Al/a-Si core-shell nanostructures.

1.2 Objectives

The objective of this study is to gain a fundamental understanding of the deformation-resistant mechanical behavior of Al/a-Si core-shell nanostructures through a combination of experiments and atomistic modeling. This knowledge will enable the rational design of deformation-resistant nanostructures that can be used in a variety of nanomechanical applications. The specific goals are:

1. Experimentally investigate the role that core confinement, defined by the size of the confined core volume, plays on the mechanical deformation behavior of hemispherical Al/a-Si CSNs.
2. Experimentally investigate how the "dimensionality" of core confinement affects the mechanical behavior of these nanostructures through experiments on horizontally-aligned core-shell rods and layered thin films.
3. Use atomistic modeling to gain insight into the dislocation-based mechanisms that govern the mechanical behavior of these nanostructures.

4. Characterize the friction, adhesion, and surface deformation of surfaces patterned with Al/a-Si CSNs.

1.3 Layout of Dissertation

This dissertation is divided into 7 chapters, including the introductory chapter. Chapter 2 is a comprehensive literature review on the mechanical properties and behavior of nanomaterials, focusing on unique mechanical behaviors that are evident in small-scale material volumes. Chapter 3 covers the relevant experimental methods and simulation techniques used to investigate the novel properties of Al/a-Si CSNs. Chapters 4 and 5 explore the ways that core confinement affects the mechanical behavior of these structures, with an emphasis on core size effects and core confinement dimensionality, respectively. Chapter 6 presents a nanotribological characterization of friction, adhesion, and surface deformation of surfaces patterned with CSNs. Finally, Chapter 7 contains the conclusions and an outlook on future research directions for CSNs.

CHAPTER 2

LITERATURE REVIEW

CSNs have primarily been studied in terms of the enhancement of optical [23-27], magnetic [25,28-30], and catalytic properties [31-33], with an emphasis on emergent behavior that occurs due to the nanoscale structure size and related confinement effects. Examples include tunable photoluminescence in metal/semiconductor nanoparticles [27], improved dielectric properties of perovskite composite nanoparticles [30], and size-dependent catalytic efficiencies in bimetallic core-shell nanostructures [33]. These enhanced properties are the result of a combination of the familiar size effects observed in nanomaterials [34] due to the large surface-to-volume ratios and the non-trivial role the core-shell structure plays in the applicable photonic, electronic, plasmonic, magnetic spin, band-gap, and other interactions within the CSN. Recently, CSNs have also been investigated for use in biomedical applications [35-37], particularly as platforms for drug delivery [38], gene therapy [39], and contrast agents for magnetic imaging [40,41]. Clearly, the wide range of improved material properties that CSNs exhibit can benefit a variety of fields.

Despite the large number of studies on the enhanced properties of CSNs, very little research exists on the mechanical behavior of these structures. Knowledge of both the mechanical properties and deformation behavior of CSNs is becoming increasingly important as these structures are implemented into a wider range of practical applications, especially those where the CSNs will be active mechanical components, such as nanotribology and micro/nano-electro-mechanical systems (MEMS/NEMS).

2.1 Mechanical Behavior of Nanomaterials

It is well known that the mechanical properties of thin films, nanostructures, and other nanomaterials can greatly differ from those of bulk materials as the dimensions of these structures are sufficiently reduced below the sub-micron length scale. For crystalline and polycrystalline materials, the mechanical behavior becomes much more dependent on the dynamics of the included dislocations [9,42-44], leading to unique mechanical behaviors that are not observed in bulk materials. These enhanced mechanical properties provide avenues for engineering structures with desirable properties [45], potentially benefiting diverse fields such as MEMS/NEMS [46-49], nanotribology [50,51], and biomedical applications [17,52].

The earliest embodiments of materials with nanoscale features include both nano-grained metals and solid thin films. The familiar Hall-Petch relationship, known since the 1950s, predicts that the yield strength of a metal increases with decreasing grain size down to ~10 nm [53]. For these materials, the closely-spaced grain boundaries act as obstacles for dislocation motion, and the associated dislocation pile-ups that occur result in material strengthening. As the grain size decreases below 10 nm, this strengthening mechanism gives way to grain boundary sliding and rotation [54]. This interplay between macroscale mechanical properties, grain size, dislocation dynamics, and grain boundary motion serves as one of the most prominent examples of the unexpected and usually non-intuitive way that nanoscale features can affect material properties.

Thin film systems have also been widely studied to better understand the mechanical behavior enabled by their quasi-2-dimensional structure [42]. Residual stress develops due to the

lattice mismatch between the substrate and film, which is potentially thickness-dependent and can vastly alter the microstructure and cohesiveness of the film. When a lattice mismatch exists, a strained dislocation-free thin film can only exist up to a specific critical thickness, above which stress relaxation occurs in the film in the form of misfit dislocations at the film-substrate interface. Residual stress developed in the thin film can have a marked effect on the mechanical properties of the thin film layer [55]. Furthermore, for materials that can accommodate dislocations, the thin film geometry is subject to the dislocation channeling mechanism, in which the film acts as channel in which the motion of dislocations is constrained [56]. In this way, the behavior of dislocations in the thin film, and thus the mechanical properties, are altered simply through geometry.

Utilizing this layer confinement effect, multilayer composites have been investigated in order to engineer layered nanocomposites with improved mechanical properties. Chawla *et al.* studied the indentation behavior of multilayer Al/SiC composites [4]. The composites were fabricated from alternating layers of magnetron sputtered Al and SiC, with individual layer thicknesses of 25-50 nm and 41 total layers for each sample (21 A1 layers, 20 SiC layers). Improved hardness was noted in composites with thinner individual layers, which was attributed to constrained plasticity in the Al layers. Yielding of the multilayer film occurred as a result of cracking of the SiC layers and void formation due to plastic deformation in the Al layers. Notably, delamination or fracture of the Al/SiC interface was not observed, implying that the interfacial strength is stronger than the cohesive strength of either the Al or SiC.

Shao *et al.* investigated the role that interfaces play on the work hardening behavior of multilayer Cu/Ni, Cu/Nb, and Cu/Ni/Nb metallic nanocomposites using molecular dynamics simulations [57]. The results show that stronger work hardening is observed at the incoherent FCC/BCC Cu/Nb and Ni/Nb interfaces compared to the coherent FCC Cu/Ni interface, underscoring the role that interfacial effects can have on the behavior of dislocations in layered thin films. Brandl *et al*. further analyzed the role of metallic/amorphous interfaces, specifically the interface between FCC Cu and a Cu-Zr bulk metallic glass [58]. In this case, the presence of an amorphous material promotes the absorption of lattice dislocations by the crystalline/amorphous interface, in contrast to the previously referenced Cu/Ni/Nb interfaces that instead resulted in dislocation pile-up at the interfaces. The influence of interfacial effects provides a fascinating vantage point for engineering materials that can take advantage of controlled dislocation behavior.

More recently, studies on the mechanical behavior of 1-dimensional nanostructures such as nanopillars and nanorods have become more prevalent, especially since shear strengths approaching theoretical limits have been demonstrated in metallic nanowhiskers [59]. Jennings and Greer performed uniaxial compression tests on electroplated single-crystal Cu nanopillars with diameters ranging from 25-525 nm [44,60]. During the tests, they found a size-dependent strength for nanopillar diameters down to 100 nm, while for pillar diameters smaller than this value, the mechanical behavior transitioned to a size-independent regime. This transition is mediated by a preference for homogeneous dislocation nucleation of perfect dislocations in large pillars and for heterogeneous dislocation nucleation of partial dislocations from surfaces and defects in smaller pillars.

The dependence of material properties on nanostructure size are a manifestation of so-called "size effects" in nanomaterials. Although these size effects are described as a purely geometric effect, the underlying mechanism is more subtly related to statistically decreased defect content in nano-sized material volumes. Rinaldi *et al.* performed compression tests on Ni pillars with different initial dislocation densities and claim that increased defect content can substantially suppress the expected size dependence on yield strength [9]. Ni nanopillars were fabricated using focused ion beam (FIB) milling from two different samples of bulk Ni: polished cold-rolled Ni plate, which represented a relatively higher initial dislocation density, and polished, well-annealed Ni plate, which represented a relatively lower initial dislocation density. For the Ni pillars fabricated from the well-annealed material, the power-law scaling that accompanies material strengthening was observed, as expected. However, for the nanopillars fabricated from the disordered material, no size dependence on yield strength/hardness was noted, even for relatively large pillar diameters of 200-300 nm. Because of the discrete nature of dislocations, a lower initial dislocation density in the bulk material corresponds to a higher statistical probability that differently sized nanostructures machined from this material will have statistically different dislocation content, resulting in emergent size effects. This result largely underscores the role that not only nanostructure size, but also defect content, plays in tailoring the mechanical behavior of nanostructures.

The idea that the "smaller is stronger" phenomenon is related to statistical differences in dislocation content in pillars with different diameters has also been employed to study the mechanical properties of Ni nanobuttons, i.e., pillars with very short lengths [43]. Compared to

nanopillars, nanobuttons exhibit increased hardness as a result of plasticity confinement to increasingly smaller volumes. Whereas the Ni nanopillars fail by shear-slip at an applied stress between 500 and 1000 MPa, depending on diameter, the nanobuttons were found to withstand applied stresses in excess of 2 GPa without failure.

The role material "dimensionality" can have on the mechanical behavior of materials with sub-micron dimensions has been studied by Mordehai *et al*., who performed indentation experiments on several different Au nanomaterials, including symmetric single-crystal nanoparticles, laterally-elongated nanostructures, and thin films [61]. Au nanoparticles were fabricated from a Au thin film on a sapphire substrate using solid-state dewetting, resulting in an ensemble of both faceted equiaxial nanoparticles and elongated nanostructures. Mechanically, both the equiaxial nanoparticles and elongated particles are more compliant than the Au thin films due to the proximity of lateral free surfaces. Atomistic modeling further suggests that the mechanical behavior of the nanoparticles was dominated by dislocation annihilation events at the free surfaces, while indentation of the thin films resulted in dislocation pile-up beneath the indenter. Furthermore, the laterally-elongated structures exhibited an intermediate behavior, due to competition between dislocation annihilation at free surfaces and the formation of sessile dislocation structures.

2.1.1 Material Insights from *in situ* Transmission Electron Microscopy Experiments

Recent advances in nanomechanical transducer technology have enabled the possibility of novel *in situ* contact mechanics and nanoindentation experiments within a transmission electron microscope (TEM) [62]. This technique allows for real-time imaging of the mechanical

behavior and manipulation of nanostructures with unprecedented resolution and magnification. Materials that can be characterized by *in situ* TEM are subject to the limitations of TEM sample preparation, namely that the materials must be sufficiently thin to be electron transparent. Currently, this restricts *in situ* TEM experiments primarily to nanoparticles and thin film lamellae. Furthermore, difficulties in precisely aligning both the indenting tip and sample relative to the electron beam, and maintaining this alignment during the entirety of the experiment, can convolute the analysis, especially if the sample rotates out of the focal plane during testing [48]. Despite these limitations, *in situ* TEM experiments have been performed on a wide variety of materials, with significant insights into the small-scale behavior of materials obtained.

Minor *et al.* investigated the onset of plasticity in an Al thin film [63], specifically looking at the discontinuous indentation signatures that correspond to incipient plasticity in metals. In this experiment, a dislocation-free Al grain was indented with a sculpted diamond indenter with a radius of curvature of 100 nm. Conventionally, it is believed that ductile metals will exhibit a continuous, smooth rise in indentation load up to the elastic limit. At this point, a substantial load relaxation occurs, corresponding to the dislocation burst that accompanies the onset of plasticity. However, in this experiment, an indentation signature corresponding to plasticity was observed almost immediately after contact, even before a sustained rise in indentation load. Notably, this minor load relaxation occurred at shear stresses very close to the theoretical maximum for Al. This result clarifies the understanding of the onset of incipient plasticity in nanomaterials, namely that dislocation nucleation can potentially occur at much

lower loads than the load required to initiate a discontinuous indentation signature after a sustained rise in contact load.

Deneen *et al.* studied the deformation of single-crystal Si nanospheres during compression with a boron-doped diamond tip [64]. Both elastic and plastic deformation was observed, as well as particle fracture. Nowak *et al.* specifically studied the fracture behavior of a single-crystal Si nanosphere [65]. The nanoparticle radius was 108 nm, with a 5.4 nm native oxide film. After compressing the particle 29 nm (which corresponds to 13% engineering strain), fracture occurred. Analysis of the real-time images indicated that fracture likely began as a crack that was nucleated in the native oxide layer and advanced along the (111) crystallographic plane. In addition to identification of the orientation of the fracture plane, it was also possible to directly calculate the plane strain fracture toughness, K_{Ic}, which is an important fracture parameter.

In a study by Shan *et al.*, ultrahigh stress and strain were measured in hollow CdS nanoparticles, based on hierarchical effects related to nanoparticle diameter, shell thickness, and grain size [66]. Individual nanoparticles were observed to sustain up to 20% compressive strain and a contact pressure of over 1 GPa before fracture, which is a substantial amount of stress and strain for a normally brittle material. In addition, finite element modeling shows that local stresses within the shell can approach the ideal shear strength of CdS. The exact deformation mechanism is unknown, but theorized to be due to a combination of grain boundary diffusion, small-scale crack initiation, and dislocation plasticity. Based on these mechanisms, it is perhaps

possible to further tune the mechanical properties of these nanostructures by modifying the ratio of shell thickness to particle diameter, as well as the grain size of the shell.

Carlton and Ferreira studied the deformation behavior of nanoparticles and assessed various TEM contrast modes for identifying dislocations [67]. Notably, this experiment did not utilize any load-sensing capabilities of the *in situ* transducer. Diffraction contrast imaging was undertaken to study the deformation of a Ag nanoparticle when compressed with a diamond tip. A contrast band was observed in the nanoparticle immediately after contact, with more contrast bands forming as the strain on the particle was increased. Although these contrast bands can be attributed to dislocations, they can also be the result of diffraction artifacts. Unambiguous identification of dislocations in this imaging mode requires accurate knowledge of the diffraction conditions, which is not trivial during nanoindentation. Phase contrast experiments were also performed on a Ag nanoparticle indented by a W tip. In this mode, the atomic structure of the nanoparticle is imaged as lattice fringes. As a result, dislocations appear as an additional lattice fringe corresponding to the additional half-plane of atoms, meaning that the presence of dislocations is much more readily apparent compared to diffraction contrast imaging. In both of these experiments, the contrast signals that form during indentation disappear after the particle was unloaded, implying that the dislocations annihilated during unloading.

Direct observation of large reverse dislocation motion and associated dislocation annihilation was confirmed by Mompiou *et al.* in tensile-loaded ultrafine grained (UFG) Al [68], which was further correlated with large elastic back-strains during unloading. In this experiment, a tensile strain was applied to an electron transparent UFG Al foil (grain size ~500

nm) *in situ*, and the resulting dislocation dynamics were captured in real time. During loading, dislocations were heterogeneously nucleated at grain boundaries and traverse across the interior of the grain. Upon reaching the boundary of a neighboring grain, the dislocations either became partially inserted into the grain boundary or simply pile-up at the grain boundary, depending on the magnitude of applied stress. The repulsive stress fields generated by these dislocations create a substantial back-stress large enough to cause reverse dislocation motion upon unloading. In a coarse-grained material, the extent of this reverse dislocation motion would be negligible; however, due to the small grain size of UFG Al, dislocations can actually move back across the entire width of the grain and annihilate at the original source. This behavior is more prevalent with decreasing grain size, due to a more rapid build-up of dislocation pile-ups at adjacent grain boundaries, a larger stress concentration, and a higher likelihood that the reverse dislocation motion will be sufficient for the dislocations to move back to their source and annihilate.

Dislocation annihilation at surfaces and interfaces has also been shown to result in a phenomenon known as mechanical annealing, as studied by Shan *et al.* in FIB-milled Ni nanopillars [15]. Nanocompression experiments with a flat diamond punch were performed on an initially defect-filled nanopillar, with a dislocation density of $\sim 10^{15}$ m^{-2}. After compression, the pillar was found to be free of dislocations due to the existing defects annihilating at the free surfaces of the nanopillar, albeit with significant plastic deformation at the apex of the pillar. The now dislocation-free pillar was found to have improved strength, in accordance with the hardening behavior that occurs due to dislocation starvation in small material volumes.

2.1.2 Mechanical Behavior of Core-shell Structures

Compared to the broad range of studies on both the physiochemical properties of CSNs [69] and the nanomechanical behavior of single material nanostructures, very little information exists about the mechanical properties of CSNs. Often, mechanical investigations of CSNs rely extensively on computational modeling, using both atomistic and continuum methods.

Li *et al.* used the elasto-plastic finite element method to simulate yielding of a hemispherical shell during compression loading [70]. In this study, the authors developed a universal shell parameter that predicts the spatial location of yielding as a function of shell thickness, shell radius, elastic modulus, and yield strength. Notably, this model predicts that, above a critical shell parameter value, a hemispherical shell will behave identically to a solid hemisphere.

This analysis was extended by Goltsberg *et al.* to model yielding in hemispheres coated with hard shells [71]. An improved universal coating parameter was developed to predict the location of yield in core-shell hemispheres. Depending on shell thickness, yield was primarily found to occur in either the shell (for thicker shells) or at the core/shell interface (for thinner shells), with yield occurring within the core only in the limit of very thin shell thicknesses. In this limit, a weakening effect was predicted in spheres coated with very hard, thin shells, which was experimentally validated for steel and brass spheres coated with TiN [72].

Zheng *et al.* used atomistic modeling to study uniaxial compression of core-shell Cu/Ag nanoparticles, with an emphasis on the dislocation behavior in these structures [73]. Compared

to bare Cu nanoparticles, the presence of the Ag shell was found to substantially modify the behavior of dislocations within the Cu core. The core-shell interface acts as a nucleation site for Shockley partial dislocations with four different Burgers vectors in the <112> family within the Cu core; however, whenever a dislocation with one of the four Burgers vectors was nucleated, nucleation of partial dislocations with the other three Burgers vectors was suppressed. This suppression was not observed in the bare Cu nanoparticles, which resulted in the formation of dislocation tangles.

Experimentally, it has been shown that it is possible to indirectly calculate material properties such as Young's modulus and shear modulus of CSNs through the excitation of elastic vibrational modes using either pump-probe optical methods or inelastic light scatting [74,75]. By tuning the frequency of the excitation source, both the core and shell can be separately excited, allowing independent measurement of the constituent materials of the CSN. Both of these techniques are generally limited to isotropic, linear-elastic materials that also have coherent vibrational modes, i.e., they not applicable to amorphous materials. Due to this limitation, the application of these methods is limited to a fairly small subset of CSN material systems, and they further provide no information about the actual deformation behavior of CSNs. In order to more completely characterize the mechanical deformation of CSNs, a more direct approach is required.

One of the few studies to directly investigate the deformation behavior of CSNs involved nanoindentation of CSNs composed of CoB_2 cores with very thin (~10 nm) SiO_2 shells [76,77]. Three different regimes of particle deformation - one elastic and two plastic regimes with

different hardening rates - were observed as a function of indentation depth. This type of indentation behavior was hypothesized to be the result of a combination of interactions of pre-existing defects in the core with the SiO_2 shell and irreversible strain hardening. Clearly, the core-shell structure resulted in demonstrable changes in material behavior.

2.2 Deformation Recovery Observed in Nanomaterials

Anomalous deformation recovery has been observed in a handful of nanomaterials, which is desirable for the development of nanostructures with deformation-resistant properties. To be clear, the deformation recovery observed in these materials is unambiguously beyond what would be expected for elastic recovery, nor can it be attributed to true viscoelastic effects. Several authors have used the term "reverse plasticity" to describe this phenomenon, although it may be more accurately described as "deformation recovery beyond the elastic limit."

Gerberich *et al.* studied reverse plastic strain in single-crystal Si nanospheres in two separate studies [78,79]. In these studies, additional height recovery of the nanospheres was measured from scanning probe microscopy (SPM) after unloading, as compared to the cumulative residual displacement calculated from the load-displacement data from a nanoindentation test. For example, a nanosphere with a 50.3 nm diameter was sequentially indented 6 times, with a cumulative residual displacement of 30 nm as calculated from the load-displacement data. However, when the nanosphere height was measured using SPM, it was found to be 37.4 nm tall, which is 17.1 nm taller than would be calculated from the residual displacement. Ostensibly, this height recovery happened after unloading, and corresponds to 34% strain recovery. The percentage of recovery was found to increase with increasing

indentation load and decreasing nanosphere radius, in some cases reaching nearly 50%. This mechanical response was hypothesized to be the result of dislocations retracing their paths due to a high internal back-stress generated during nanosphere compression. It should be noted that the largest reverse strains corresponded with the most severe indentations, meaning that a substantial amount permanent deformation still accompanied the strain recovery.

Zou and Yang also observed reverse plastic deformation in amorphous silica nanoparticles with particle radii of 35-40 nm [80]. In this case, the recovery of plastic deformation was more directly observed using SPM. Immediately after a 30 μN indent, consecutive SPM images were taken to assess the deformation of the nanostructure. After the first image, a depression of 5 nm depth was observed at the apex of the nanoparticle. However, after a second consecutive image, the depth in the depression decreased by approximately 2 nm. In contrast to the theory by Gerberich that this recovery is mediated by dislocations, these nanoparticles are amorphous and therefore cannot support dislocations. Instead, it was theorized that the recovery of plastic deformation in these nanoparticles might be activated by thermal fluctuations or some other perturbation by the SPM tip.

A limited amount of reverse plasticity has also been observed in the CoB_2/SiO_2 core-shell structures mentioned previously [76,77]. Much like silica nanoparticles, the core of these nanoparticles is also amorphous, which precludes dislocation-based strain recovery mechanisms. Instead, the deformation recovery is attributed to possible mechanical-magnetic coupling effects in the CoB_2 core. Like the Si nanospheres and silica nanoparticles, the deformation recovery is not complete.

Vlassov *et al.* reported on the mechanical behavior of Ag/SiO_2 core-shell nanowires in response to bending deformation [81]. These nanowires exhibited enhanced fracture resistance and nearly complete recovery of bending deformation during *in situ* SEM bending experiments, even with bending deflections approaching 90°. This behavior was shown to only occur in the core-shell nanowires, and not in identically prepared Ag nanowires and hollow SiO_2 nanotubes, which indicates that this phenomenon is an explicit result of the core-shell structure. However, it was also found that this shape recovery is a purely extrinsic effect related to electron beam irradiation. That is, shape recovery of the nanowires did not occur without direct exposure to the electron beam after deformation. Both the bending ductility and the deformation recovery were postulated to be the result of e-beam induced viscosity in the SiO_2 shell, which allowed the elasticity of the Ag core to dominate the nanowire deformation behavior.

In a study by Tidwell *et al.*, complete deformation recovery was identified in Al/a-Si core-shell nanostructures, fabricated from a nanotextured Al thin film that was conformably coated with a-Si [22]. The individual nanostructures were composed of ~200 nm diameter polycrystalline Al dots protruding from an Al film that were coated with a 300 nm a-Si shell, which produced hemispherical core-shell structures. When subjected to load-controlled nanoindentation up to 300 μN, these structures display unusual load-displacement behavior, most notably a complete lack of residual deformation in the load-displacement data. This suggests that the nanostructure experienced no permanent deformation after indentation, a conclusion that was further supported by scanning probe microscope images that show no structure height change after indentation. These structures were found to have a yield strength higher than either

Al or a-Si alone, and were able to sustain up to 23% engineering strain during loading, with nearly 100% recovery of this deformation after unloading. This combination of high strain-bearing capacity and deformation recovery far exceeds anything else reported in the literature. However, the mechanisms that contribute to this behavior were not determined.

2.3 Tribological Properties of Nanotextured Surfaces

Surface nano-texturing is an effective method for designing surfaces with improved tribological properties such as friction, adhesion, and wear. This is especially true for applications where the contact interactions occur on the micro- or nanoscale. In these systems, adhesion and friction issues are exacerbated due to the large surface-to-volume ratios compared to macroscale systems [82], which frequently cause device reliability issues when contact interactions are involved [83]. Nanotextured surfaces (NTSs) have demonstrated significantly reduce adhesion and friction in polymers [16,84], metals [19,20,85], and other materials [86,87]. Despite these improved tribological properties, a common weakness of NTSs is a lack of structural integrity of the individual nanotextures when subjected to contact loading. This results in permanent deformation of the surface at even moderate contact forces, as well as an associated loss of desirable tribological properties, such as reduced friction or adhesion.

Yoon *et al.* studied the tribological properties of patterned PMMA films with topography based on the lotus leaf [16]. This surface exhibited improved friction and adhesion behavior compared to a non-patterned PMMA thin film due to a combination of a hydrophobic surface chemistry and nanoscale surface topography that serves to reduce the contact area during loading, although the PMMA nanotextures were significantly deformed during microscale

friction testing. In turn, this deformation results in an increase in real area of contact during subsequent frictional contact and an attendant increase in friction. Beyond the simple geometric aspect of contact area, surface topography contributes to the surface free energy, which governs solid-solid adhesion. The surface free energy, in turn, determines the surface wettability (hydrophilicity/hydrophobicity) that governs capillary (solid-liquid) adhesion [84]. Therefore, the implications of surface deformation go beyond mechanical damage and can potentially result in more comprehensive surface property degradation.

The tribological properties of Ni nanodot patterned surfaces have been studied by Zou *et al.* [19] and Wang *et al.* [20]. The nanodot patterned surfaces were fabricated by thermal evaporation of Ni through an anodized aluminum oxide membrane, which created large area hexagonal arrays of Ni nanodots. Ni nanodot patterned surfaces exhibited superior friction and adhesion performance compared to single crystal Si, primarily due to a reduction of contact area with the nanotextured surface. Even still, the mechanical durability was found to be lacking. Although the individual Ni nanodots were shown to have a higher hardness compared to bulk Ni [85], when subjected to nanoscratch testing with a 1 μm diamond tip, deformation occurred at normal loads as low as 4 μN. Hertzian contact theory calculations indicate that the shear stress at this normal load is over 3 times larger than the theoretical shear strength of Ni, which explains why the nanodots deformed at such a low load. Based on this data, it is possible to conclude that purely metallic nanostructures may not be sufficiently resistant to surface deformation for use in practical applications.

Park *et al.* studied the tribological behavior of nano-undulated diamond-like carbon (DLC) films, fabricated by deposition of DLC onto a surface patterned with Ni nanodots. The study found them to have favorable microscale frictional properties compared to smooth DLC films [88]. The improved tribological properties were attributed to a reduced area of contact due to the nano-undulated surface, as well as a suppression of the tribochemical reaction with the environment with increasing roughness in the presence of humidity [89]. In these studies, there is no stated influence from the underlying Ni nanodots on the mechanical behavior of these surfaces, and the formation of wear debris was still observed during ball-on-disk tribometer experiments. These surfaces have also been evaluated for possible use in MEMS devices [90], and have been found to have reduced friction, as well as reduced solid-solid and capillary adhesion, compared to smooth DLC films. Microtribometer experiments using a 0.5 mm soda lime ball and 3000 μN normal load, which corresponds to an extremely low contact pressure, showed no evidence of microscale surface deformation after 150 cycles, although it was not determined if any deformation occurred at the nanoscale.

Morton *et al.* investigated the nanotribological properties of NTSs composed of both Al nanodots and Al/a-Si CSNs [18], the latter of which have been shown by Tidwell *et al.* [22] to have interesting deformation-resistant properties. Compared to a smooth Si wafer, the Al nanodots effectively decreased the measured coefficient of friction at low normal loads when characterized by nanoscratch testing with a 100 μm diamond tip. Surface deformation of the nanodots was detected at normal loads as low as 750 μN, causing a notable increase in plowing friction. At higher loads (4000 μN and above), the plowing friction became so severe that the Al nanodots performed worse than smooth Si. Far superior frictional properties were obtained from

the CSNs, which showed a reduction in coefficient of friction of 56-74% compared to smooth Si, depending on normal load. In addition, no observable surface deformation occurred, even for normal loads as high as 8000 μN. This combination of reduced friction and improved deformation resistance is unusual, especially at relatively large contact pressures. Typically, there will be a tradeoff between these attributes.

2.4 Summary

Clearly, a plurality of unique mechanical phenomena is observed in nanomaterials. Based on a survey of the relevant literature, it is plausible that the unique deformation-resistant properties of Al/a-Si CSNs could be facilitated by a number of nanoscale material behaviors, including conventional size effects; dislocation interactions within the Al core, including interactions with grain boundaries and the core-shell interface; and core-shell mechanics. Determination of the exact mechanisms that contribute to the mechanical behavior of the CSNs will further enable the development of nanomaterials with desirable mechanical properties, potentially benefiting a number of high-tech fields.

CHAPTER 3

EXPERIMENTAL METHODS AND SIMULATION TECHNIQUES

In this chapter, an overview of the techniques used to design, fabricate, and characterize the properties of Al/a-Si core-shell nanostructures are presented. In addition, modeling methods utilizing molecular dynamics simulations are also described.

3.1 Nanostructure Fabrication

The fabrication method used in the foundational studies on the properties of Al/a-Si CSNs [18,22] resulted in a textured surface populated with a random ensemble of CSNs, with minimal control over the CSN size, shape, location, or density. This lack of spatial control severely limited the characterization and comparative analysis of multiple structures and prevented the detailed analysis of a single structure by multiple characterization techniques. To rectify this limitation, a new fabrication method employing electron beam lithography (EBL) and a metal lift-off procedure has been developed. This method can produce regular arrays of nanostructures with great control over the size, shape, and location of the individual metallic cores. From these metallic nanostructure arrays, core-shell structures are fabricated by depositing a-Si using plasma-enhanced chemical vapor deposition.

3.1.1 Electron Beam Lithography and Metal Lift-off

EBL is a maskless lithographic technique in which a pattern is written into an electron resist (an electron-sensitive polymer) by rastering an electron beam over the desired area of a sample surface, typically with nanometer resolution [91]. The attainable size and resolution of patterns written by EBL are strongly dependent on electron beam parameters, such as

voltage/dose and spot size, and the resist chemistry. Analogous to photoresists used in conventional photolithography, both positive and negative electron resists exist. For positive resists, electron beam exposure induces scission reactions in the exposed polymer, resulting in higher dissolution sensitivity to the development solvent compared to the unexposed polymer. Conversely, negative resists become cross-linked during electron exposure, resulting in lower dissolution sensitivity during development.

The process for fabricating metallic nanostructure arrays on a conductive substrate is outlined in Fig. 3.1. First, 4% concentration of 495k MW PMMA (a positive electron resist with a suitable undercut for metal liftoff applications) is spin-coated onto the substrate at 3000 rpm. At this concentration and speed, the resulting PMMA film is ~200 nm thick. Patterned areas are then written into the PMMA film by selective electron beam exposure (a). After exposure, the samples are developed in a 1:3 mixture of methyl isobutyl ketone (MIBK) and isopropyl alcohol (IPA) for 30-45 s, and then rinsed in pure IPA for 15 s (b). This can be followed by an optional low-power plasma etch to help smooth the rough edges of the features developed in the PMMA film. After development, a thin film of metal is deposited onto the patterned PMMA arrays, resulting in metal infill into the holes in the PMMA film (c). In principle, this can be accomplished with almost any low temperature deposition technique, such as physical vapor deposition (PVD), metal plating, or chemical vapor deposition (CVD) methods that utilize substrate temperatures below the glass transition temperature of PMMA (~105 °C). For best lift-off performance, the deposited metal film should be no thicker than half the electron resist thickness. The remaining PMMA is then selectively removed by immersion in a solvent

(Remover PG, MicroChem Corp.) at 70-80°C (d), resulting in regular metallic nanostructure arrays (e).

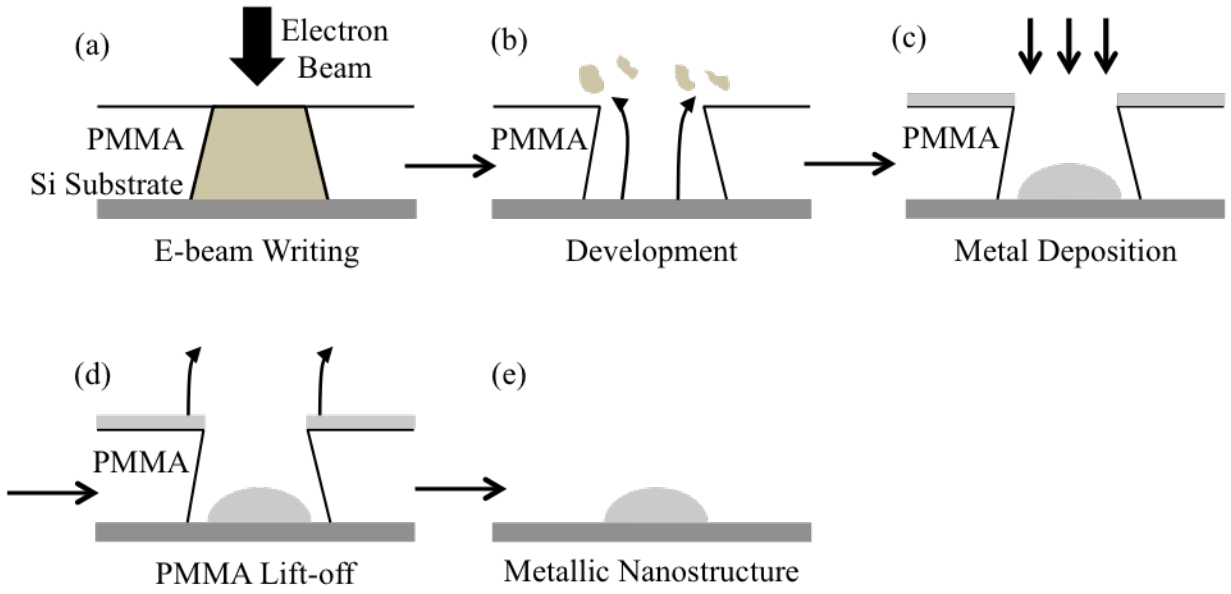

Fig. 3.1: Flowchart of the EBL and metal lift-off procedure for fabricating metallic nanostructures.

A dedicated electron beam writer (JBX-9300FS, JEOL Ltd.) was used to produce templates for fabricating metallic nanodots and horizontally-aligned nanorods. The exposure parameters were 1 nA of current, a 50 kV accelerating voltage, and a size dependent beam dose: 775 $\mu C/cm^2$ for 100 nm hole diameters and 1000 $\mu C/cm^2$ for 200-300 nm hole diameters. The metallic nanostructures were deposited using thermal evaporation (Auto 306D, Edwards Vacuum). Ingots of Al (99.99% purity) were loaded into a resistively-heated tungsten boat inside an evacuated bell jar. The current passed through the evaporation boat was increased until the Al source material melted and then vaporized, with the deposition thickness monitored by a quartz crystal microbalance (QCM) sensor. To fabricate the cores for the CSNs, 100 nm of Al was evaporated onto the patterned PMMA films at a rate of 0.4 nm/s. Using this method, Al nanodots with base diameters of 100, 200, and 300 nm, as well as Al nanorods with diameters of 100 nm and lengths of 100 nm, 500 nm, and 10 μm, have been produced.

3.1.2 Plasma-enhanced Chemical Vapor Deposition

CVD is frequently used in the microelectronics industry for fabricating semiconductor or ceramic thin films on substrates. In contrast to PVD methods, in which material is deposited through vaporization or atomization of a source material that then condenses on a substrate, thin film deposition using CVD techniques occurs via chemical reactions and/or chemical decomposition of precursor gasses at elevated temperatures [92]. Plasma-enhanced chemical vapor deposition (PEVCD) is a CVD process that allows for deposition of semiconductor and ceramic materials at substantially lower temperatures than conventional CVD. In this method, the sample and precursor gasses are contained between parallel plate electrodes that are biased to

create either a radio frequency or direct current plasma. This plasma serves to considerably increase the reaction rate of the deposition reaction at lower temperatures.

To fabricate the shells of the CSNs, a-Si was directly deposited onto the patterned Al nanodot arrays using PECVD (Plasma-Therm SLR730). The substrate temperature, radio frequency power, and silane flow rate were 250° C, 20 W, and 85 sccm, respectively, during a-Si deposition. The a-Si deposition rate was characterized by depositing a-Si thin films on Si wafers for various durations, and then measuring the resulting film thicknesses as a function of deposition time with an optical spectrometer (aRTie, Filmetrics). The thickness-time relationship, which is sufficiently linear in the time range under investigation, is shown in Fig. 3.2. From this relationship, the necessary deposition times to produce a-Si films with 100 nm and 300 nm thickness were determined.

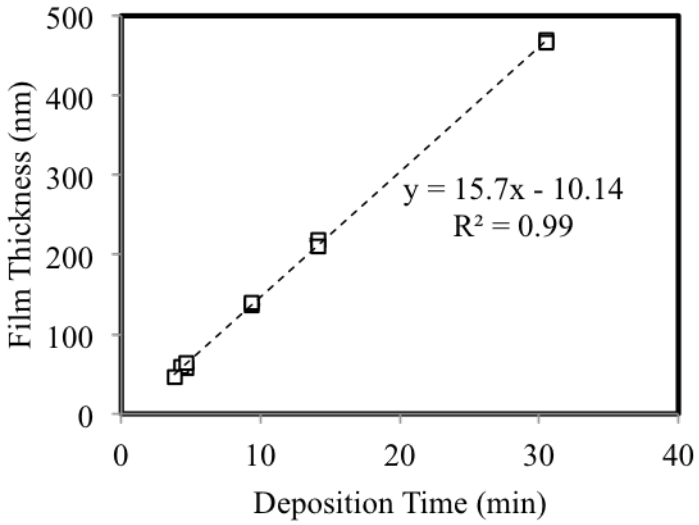

Fig. 3.2: Characterization of PECVD a-Si film thickness as a function of deposition time.

3.2 Instrumented Nanoindentation

Nanoindentation is a powerful nanomechanical technique for probing the mechanical properties of small material volumes [93]. Originally developed to quantitatively measure elastic moduli and hardness in isotropic solids [94-96], the field of nanoindentation research has expanded to include nanomechanical measurements on thin films [97-99], nanoparticles [78,80], nanocomposites [12,100,101], biomaterials [102,103], and polymers [104,105].

3.2.1 Load- and Displacement-controlled Indentation

In a typical nanoindentation experiment, a hard (usually diamond) tip with a well-defined shape is pushed into a sample surface while simultaneously measuring load and displacement of the indenter, with force and displacement resolution that could reach nN and sub-nm levels, respectively. Through the use of feedback control, tests can be conducted with a wide range of load/displacement profiles and loading rates. In load-control mode, the nanoindenter transducer is controlled to apply load at a specified loading rate, while measuring the resulting displacement. In displacement-control mode, the load is measured in response to a specified displacement profile.

The resulting load-displacement curves obtained from nanoindentation experiments offer a wealth of material behavior information. Schematics of typical load-displacement curves are shown in Figure 3.3, for both load-controlled and displacement-controlled modes. Aside from characterizing indentation parameters such as maximum load, maximum indenter displacement, contact stiffness, and residual displacement after unloading, discontinuous indentation signatures, which represent microscopic events occurring in the material volume beneath the

indenter tip, are also characterized. For load-controlled indents, these signatures appear as displacement excursions at constant load, often called "pop-ins" and "pop-outs" when the signatures appear in the loading and unloading portions of the load-displacement curve, respectively. In displacement-control mode, the analogous signature to the pop-in, known as a "load-drop," appears as a sudden relaxation in the indentation load. Likewise, the displacement control analog of the pop-out, called a "load-jump," appears as an anomalous increase in contact load during unloading. Physically, these signatures represent a discontinuity in the stiffness of the material being indented, which can be attributed to a variety of material behaviors, such as plasticity, phase transformations, and fracture. For multi-component materials, such as CSNs, the physical origin of the indentation signatures is potentially ambiguous and substantial additional characterization is required.

An instrumented nanoindenter (TriboIndenter, Hysitron) was used to characterize the deformation behavior of individual core-shell nanostructures, using a conical diamond tip with a 1 μm tip radius of curvature. The TriboIndenter features a 0.2 nm displacement resolution and a 3 nN indentation force resolution, feedback control modes for both force-controlled and displacement-controlled indentation, and an integrated scanning probe microscope for accurately locating and indenting individual nanostructures. A schematic of the TriboIndenter transducer setup is shown in Fig. 3.4. The sample under investigation is placed on the XY stage and then maneuvered under the transducer assembly. The indenter tip is then brought into contact with the sample. During the indentation experiment, the indentation load is applied electrostatically by biasing the bottom driving plate relative to the center plate (which is attached to the tip), and the resulting displacement is measured from the capacitance of the three-plate capacitor

composed of the center plate and the two electrostatic driving plates. Feedback algorithms are used to control the transducer motion to follow either a specified loading/unloading rate or a specified linear displacement profile, and the resulting load-displacement data is logged. The load-displacement behavior of CSNs, CSRs, and layered thin films have been characterized primarily using displacement-controlled nanoindentation, which is more sensitive to the transient events that correspond to the discontinuous indentation signatures [106].

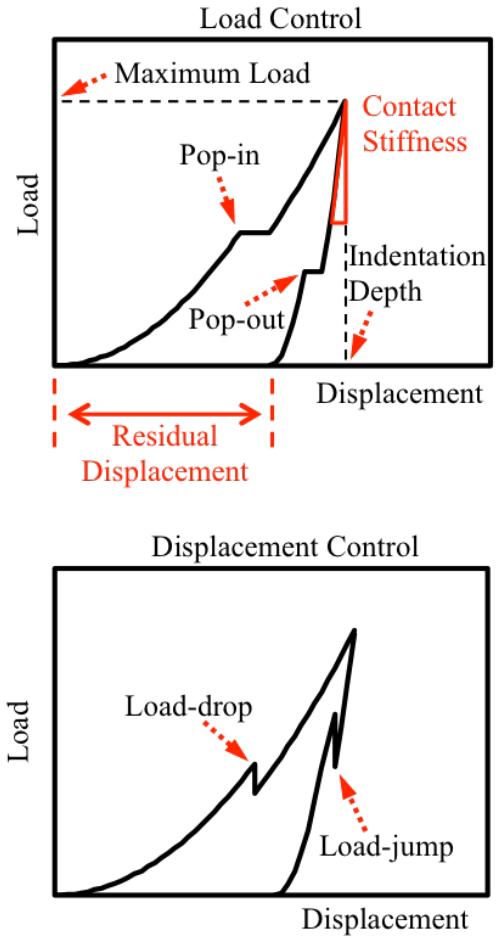

Fig. 3.3: Schematics of load-displacement curves for load-controlled and displacement-controlled indentations.

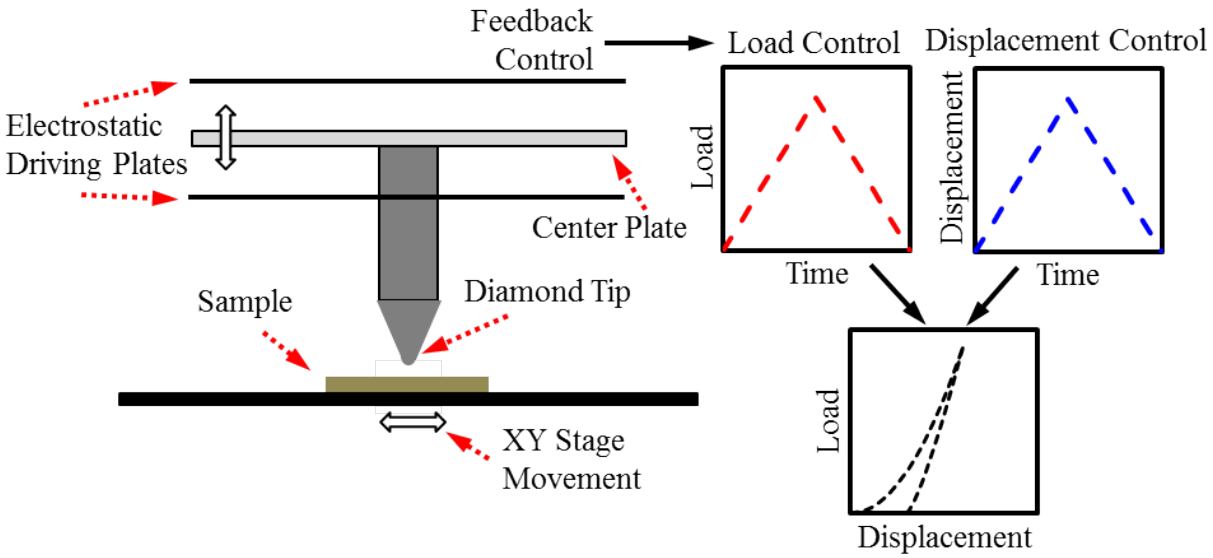

Fig. 3.4: Schematic of the nanoindenter transducer. The transducer can be feedback controlled to follow a specified normal load or displacement profile, with the resulting displacement or load response logged, respectively.

3.3 Nanoscale Imaging Characterization

Since the deformation behavior of CSNs is of interest, imaging techniques with nanoscale resolution are required to characterize the geometric properties of the nanostructures before and after deformation of the nanostructures. Detailed nanostructure morphology is characterized by scanning electron microscopy (SEM) and atomic force microscopy (AFM). In addition, an *in situ* scanning probe microscope (SPM) integrated with the nanoindenter allows for comparative measurements of nanostructure height immediately before and after nanoindentation.

3.3.1 Scanning Electron Microscopy

SEM is a common technique for imaging surface features of conducting or semiconducting materials in vacuum, usually with nanometer resolution. In a typical SEM, a beam of electrons is produced with either a field emission or thermionic emission electron gun and is accelerated toward the specimen with a specified accelerating voltage. The incident beam of electrons penetrates into the sample, causing secondary electrons to be emitted. These secondary electrons are then collected by an electron detector as the beam rasters over the sample surface to produce a spatial intensity map, which is then digitized to form an image.

The surface morphology of the Al nanostructures, CSNs, CSRs, and thin films were imaged using a field-emission SEM (Nova NanoLab, FEI), with acceleration voltages of 5-15 kV and beam currents of 0.2-2.2 nA. The Nova is a dual-beam unit that also includes a focused ion beam (FIB) for preparing cross-sectional images of individual nanostructures. Cross-sectioning in accomplished by first using electron or ion beam-assisted deposition to deposit a protective Pt layer over the area of interest, followed by milling a suitable depth into the sample surface at

normal incidence with the FIB. The exposed cross-sections are then imaged by the SEM at oblique incidence.

3.3.2 Atomic Force Microscopy

AFM is a scanning probe technique in which small-scale surface topography is physically measured by the deflection of a piezoelectric tube as it is scanned over the surface, with sub-nanometer resolution. In a typical AFM set-up, a micromachined cantilever with a sharp pyramidal tip (radius of curvature <10 nm), generally fabricated from crystalline Si or Si_3N_4, is affixed to the piezoelectric scanning tube. The motion of the cantilever beam is measured as the tip is scanned over the sample surface, and feedback controls are used to modulate the piezo voltage such that it accurately follows the surface topography. Three different imaging modes – contact, tapping, and peak-force tapping, each with different feedback metrics - are prominently used for measuring topography.

In contact mode, the tip is brought into intimate contact with the sample surface until a specified cantilever deflection is reached, and the piezo voltage is then modulated to maintain this deflection value. This mode provides the most direct measurement of topography; however, there is a high risk of tip and/or surface damage due to prolonged contact. In addition, this mode is very susceptible to tip-sample adhesion, which can significantly degrade image quality. In tapping mode AFM, the cantilever is oscillated such that it only makes intermittent contact with the sample, with the driving frequency typically just below the resonance frequency. This frequency becomes damped as the tip interacts with the sample, and the piezo is feedback-controlled to maintain the target oscillation frequency. Peak-force tapping mode operates

similarly, except the target set point is instead the tapping force exerted by the tip as it comes into contact with the sample, rather than the oscillation frequency.

The surface topography of Al nanostructures, CSNs, and CSRs was imaged using AFM (Dimension Icon, Bruker), primarily in peak-force tapping mode. The Dimension Icon features a proprietary imaging algorithm (ScanAsyst) that dynamically optimizes the peak-force set point and set point gain to achieve high-quality image fidelity with minimal operator input. Triangular Si_3N_4 cantilevers (SCANASYST-AIR) with a nominal tip radius of 2 nm were used to image at a scan rate of 1 Hz.

3.3.3 *In situ* Scanning Probe Microscopy

The TriboIndenter is equipped with a piezoelectric transducer that functions as a SPM. Fundamentally, this imaging technique operates similarly to an AFM, except that the feedback metric is the normal load measured by the electrostatic transducer on the nanoindenter. The transducer is mounted to the piezoelectric scanner head, and the diamond tip is lowered onto the sample surface until a user-defined normal force is reached. As the scanner rasters over the surface, the topography is tracked by modulating the piezo voltage to maintain a constant normal force as measured by the force transducer. Since topography measurements are performed with the same tip as the nanoindentation experiments, tip convolution effects can potentially result in substantially exaggerated lateral dimension measurements compared to AFM, especially for large tip radii. However, height resolution is largely unaffected by tip convolution, so highly accurate height measurements can still be achieved with this technique.

The mechanical stage on the nanoindenter has a positioning resolution on the order of 0.5 μm, so the *in situ* SPM is instrumental for precisely locating and indenting individual nanostructures. After coarsely positioning the nanoindenter transducer with the XY stage, SPM imaging mode was engaged, and piezo offsets were applied to bring the nanostructured desired for investigation directly under the transducer. SPM topography images were acquired before and after each indentation, with a force set point of 1 μN.

3.4 Molecular Dynamics Simulations

Molecular dynamics (MD) is a widely used computational method for modeling material behavior on the atomistic scale. Specifically, MD has proven to be a very effective method for simulating dislocation activities and interfacial phenomena [73,107-112]. In an MD simulation, atoms are represented as point masses that obey Newton's laws of motion, with the mutual interactions between atoms described by a specified interatomic potential. Numerically integrating the equations of motion, subject to appropriate initial and boundary conditions, allows atomic trajectories to be calculated and tracked. Additional thermodynamic boundary conditions, such as thermostats [113] and barostats [114] that approximate canonical (NVT) and isobaric-isothermal (NPT) ensembles [115], can be introduced by appropriately modifying the equations of motion to couple the atomistic system to the surrounding environment [116].

Large-scale simulations of nanoindentation processes in atomic systems are now quite common [117-119] and can provide insight to the nanoscale mechanisms that determine material behavior during nanoindentation. Such simulations have elucidated the role of tip-surface interactions [120-123], dislocation nucleation at surfaces and interfaces [124-126], elastic-plastic

transitions [6], film-substrate interactions [127], and surface defect effects [128,129] on mechanical behavior, among other relevant nanoscale mechanical phenomena that are not typically experimentally accessible. The utility of MD nanoindentation modeling allows for simulation of nanoindentation experiments on core-shell nanostructures, with the goal of determining the microscopic mechanisms that contribute to the observed deformation-resistant behavior in these structures.

3.4.1 The Modified Embedded Atom Method

The embedded atom method (EAM) describes the interatomic potential, and thus the atomic potential energy, as a many-body functional of the background electron density of a system [130]. More plainly, EAM calculates the potential energy of an atom as the energy required to "embed" the atom into the background electron cloud. The most salient feature of EAM is its ability to successfully model cohesive interactions and defects in metals. While EAM is suitable for simulating metallic systems, it is unsuitable for modeling materials with directional bonding interactions, such as Si. The modified embedded atom method (MEAM) corrects this deficiency by replacing the spherically averaged electron density used in EAM with an angularly dependent electron density [131], which allows simulation of metallic and non-metallic elements within the same theoretical framework. Recent efforts by Jelinek *et al.* have produced a MEAM potential that includes combinatorial parameters for Al-Si interactions [132], which should be suitable for modeling the interfacial interactions between the core and shell in Al/a-Si core-shell structures.

3.4.2 Dislocation Extraction Algorithm

As long as an appropriate interatomic potential is used, molecular dynamic simulations can model dynamic changes in crystal structure, such as phase transformations and defect nucleation, without additional constitutive laws. However, changes in crystal structure are potentially difficult to identify simply by atomic positions, especially at system temperatures where thermal vibrations can be significant. To remedy this, a number of metrics to quantitatively assess changes in crystal structure have been developed, each with their own strengths and weaknesses.

Common neighbor analysis (CNA) [133] is an effective method of discriminating different crystal structures within a lattice, making it ideal for identifying phase transformations. This method assigns a crystal structure (i.e., FCC, BCC, or HCP) to an atom by analyzing the number of nearest neighbors to the atom as well as the bonding topology of these neighbors. To this end, CNA can identify the presence of defects through atoms that do not have the appropriate bonding that corresponds to a known crystal structure, but yields little other information about the type of defect. Another method, the centrosymmetry parameter (CSP), quantifies the local deviations from centrosymmetry that often accompany defects in centrosymmetric lattices [134]. Characteristic values of this parameter can be used to identify bulk atoms, atoms within a dislocation core, stacking faults, and surface atoms. Conversely, this method is only applicable to centrosymmetric lattices, and even then, it cannot distinguish between multiple crystal structures. Other structure identification methods, such as bond order analysis, bond angle analysis, and Voronoi decomposition, also exist [135]. A major limitation

of all of these methods is that they do not directly characterize the defect, but rather the effect that the defect causes on the surrounding atoms.

For dislocations, this limiting weakness means that no information about dislocation type or Burgers vector can be obtained from these methods. In order to study in-depth dislocation dynamics from atomistic simulations, a method of analyzing and representing complete dislocation lines is preferable. The dislocation extraction algorithm (DXA) provides defect identification in cubic and hexagonal lattices, including dislocations, grain boundaries, free surfaces, and pores [136]. DXA uses CNA to identify "defected" atoms that are not in a perfect lattice configuration, generates a closed 2-dimensional mesh to separate crystalline atoms from defect atoms, and then systematically constructs a Burgers circuit around the defected material to identify individual dislocation lines. The functionality of this algorithm provides a very complete quantitative characterization of atomic distortion, making it useful for studying dislocation dynamics. For example, in FCC Al, DXA can effectively distinguish between perfect FCC and Shockley partial dislocations, as well as identify unperturbed atoms in an FCC configuration and the HCP atoms in the stacking faults bounded by Shockley partials.

3.4.3 MD Nanoindentation Simulation of Core-shell Nanostructures

MD simulations of nanoindentation of Al/a-Si core-shell nanostructures and core-shell nanorods were performed using the Large-scale Atomic/Molecular Massively Parallel Simulator (LAMMPS) [137] to determine the effects of core confinement on the dislocation behavior of these structures. A schematic of a CSN simulation domain is shown in Fig. 3.5. The simulation domain consists of a single-crystal (001) FCC Al core on a 1 nm rigid substrate of frozen FCC

Al atoms, covered by a shell of a-Si. A rigid Al substrate was chosen to provide a commensurate core/substrate interface to prevent the formation of misfit dislocations at the core/substrate interface due to the lattice mismatch between Al and Si. The nanostructure is indented along the *y*-axis, and periodic boundary conditions are applied in the *x*- and *z*-directions. The a-Si shell was constructed by calculating the number of Si atoms that would be contained in the shell region if it were composed of crystalline Si with a diamond cubic crystal structure, and then randomly populating the shell region with this number of Si atoms to form a fully-dense a-Si shell. The biggest limitation to using MEAM to model a-Si is the unrealistic densities obtained from the classical method of slowly quenching a Si melt [138]. To rectify this, the density of the a-Si shell was corrected by systematically removing Si atoms that were within 1.5 Å of another Si atom in order to achieve an experimentally validated shell density of 2.28 g/cm^3 [139] after equilibration.

In these simulations, the indenter is modeled as a spherical repulsive potential of 100 nm radius, which is more computationally efficient than explicitly modeling the indenter tip as a collection of atoms or a rigid body. The force exerted on an atom by the indenter is calculated as:

$$\begin{aligned} F(r) &= -K(r-R)^2, \quad r < R \\ F(r) &= 0, \quad r > R \end{aligned} \tag{3.1}$$

where K is a constant describing the "strength" of the indenter, R is the radius of the indenter, and r is the distance of the atom from the center of the indenter. To model the nanoindentation process, a spherical indenter (K = 10 eV/Å^3) is controlled to move into the CSN a specified depth with a constant velocity of 0.5 Å/ps while maintaining a system temperature of 300 K. This process closely mimics a displacement-controlled nanoindentation experiment, albeit with a

displacement rate that is 9-12 orders of magnitude larger than is used in typical nanoindentation experiments. Examples of LAMMPS scripts for CSN and CSR nanoindentation simulations are located in Appendix 1. Dislocation activities within the cores of the CSNs are visualized using DXA within the Open Visualization Tool (OVITO) [140]. DXA enumerates the length of each dislocation segment, which allows the dislocation density within the Al core to be calculated according to the formula:

$$\rho = \frac{\sum \ell_i}{V} \tag{3.2}$$

where ℓ_i is the length of the i-th dislocation line and V is the volume of the Al core.

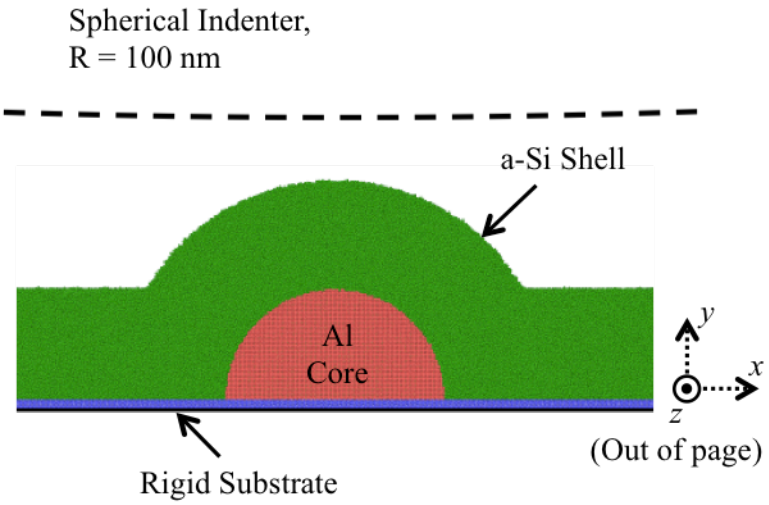

Fig. 3.5: Schematic of the MD simulation domain used during the nanoindentation simulations.

3.5 Nanotribological Property Characterization

The TriboIndenter is equipped with a two-axis transducer that can measure lateral forces in response to controlled lateral displacements. This functionality is useful for nanotribological characterization of surfaces, especially measuring friction forces and coefficients of friction (COFs). In addition, pull-off adhesion forces can be directly measured from shallow-depth displacement control indentations.

3.5.1 Nanoscratch Testing

Nanoscratch tests were performed with the two-axis nanoindentation transducer, which has a 500 nN lateral force resolution. A schematic of a typical nanoscratch load/displacement profile is shown in Fig. 3.6. Friction behavior was characterized by scratches 8 μm in length at a lateral displacement rate of 1 μm/s and a conical diamond tip with a 100 μm tip radius of curvature. During each scratch test, the normal and lateral forces and displacements are measured, which allows the COF to be calculated as the ratio of the lateral force to the normal force averaged over the scratch length.

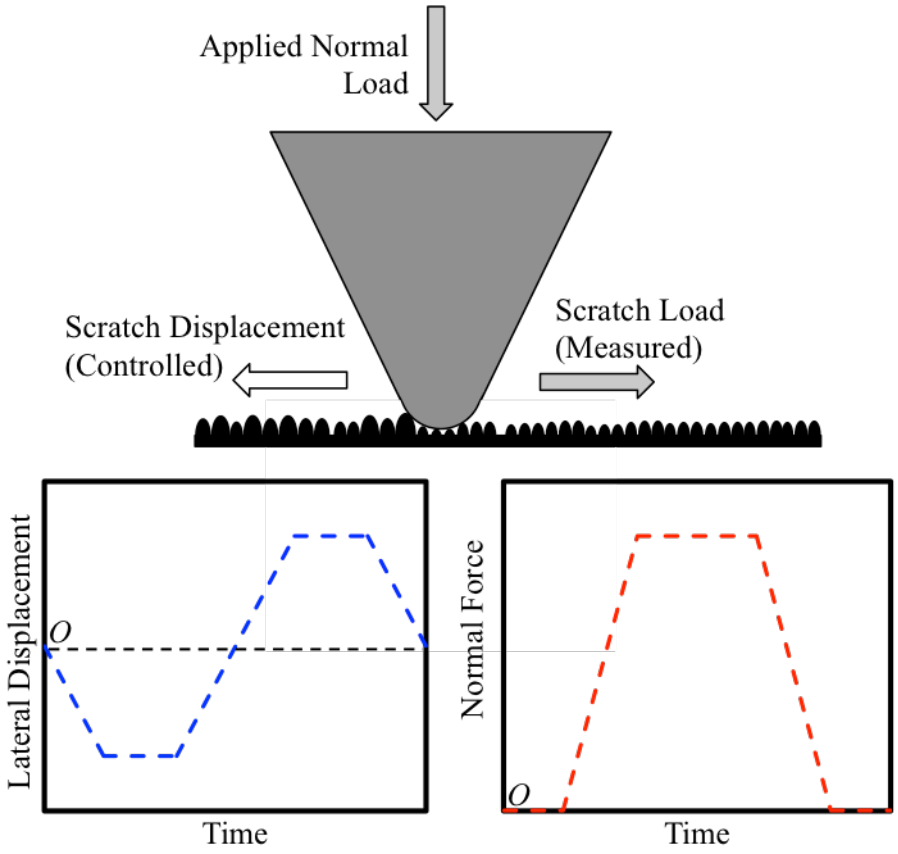

Fig. 3.6: Schematic of the transducer operation during a nanoscratch experiment.

3.5.2 Adhesion Measurements

Adhesion tests were also performed with the nanoindenter using displacement-controlled indents with a 100 μm tip. As the tip approaches the surface, an attractive tip-sample force results in a "snap-to-contact" event. Then, the tip indents a specified distance into the sample surface, and finally withdraws completely from the surface. During withdrawal, the measured normal force will become negative as the tip breaks the solid-solid adhesion between the diamond tip and the surface. The adhesion force is then the minimum force measured during withdrawal, which is illustrated in Fig. 3.7. To reduce the influence of feedback-induced noise on the adhesion measurements, the load-displacement data during unloading is first smoothed with a 7-point quadratic polynomial Savitsky-Golay filter [141] before analysis.

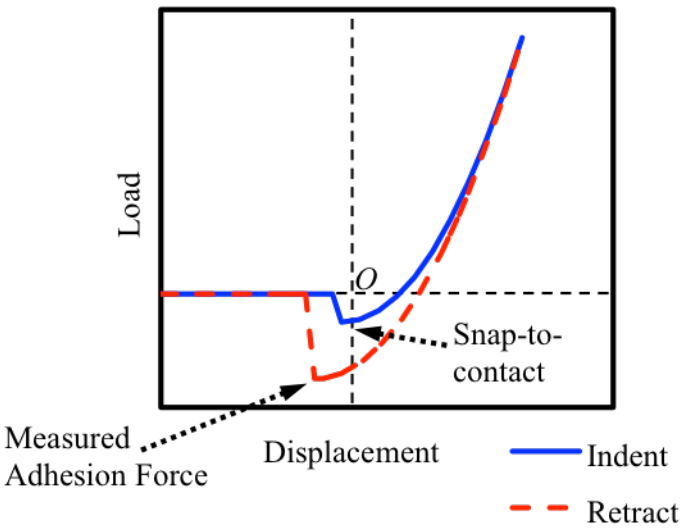

Fig. 3.7: Schematic of an adhesion measurement from the load-displacement data of a displacement-controlled indentation.

CHAPTER 4

THE ROLE OF CONFINED CORE VOLUME ON THE MECHANICAL BEHAVIOR OF AL/A-SI CORE-SHELL NANOSTRUCTURES

In this chapter, the mechanical behavior of novel Al/a-Si core-shell nanostructures (CSNs) is studied using instrumented nanoindentation to investigate the role that the size of the confined core volume plays on the mechanical response of these structures. The results show that CSNs with the smallest core diameter, and therefore the smallest confined core volume, have a unique load-displacement behavior characterized by discontinuous indentation signatures known as "load-drops" and "load-jumps" that occur during loading and unloading, respectively. In conjunction with these indentation signatures, nearly complete recovery of deformation beyond the elastic limit is observed, which is enabled by dislocation activities within the confined Al core. As the size of the confined core volume increases, the indentation signatures are suppressed and the deformation-resistant properties are reduced. Supporting molecular dynamics simulations show that a smaller core volume results in a larger back-stress developed in the core during indentation, which further correlates with improved dislocation removal from the core after unloading. The results presented in this chapter are based on a published study by Fleming and Zou [142].

4.1 CSN Surface Morphology Characterization

Using the EBL fabrication method, very uniform arrays of Al nanodots were fabricated to serve as the cores of the CSNs. SEM images of Al nanodots with 100, 200, and 300 nm base diameters are shown in Fig. 4.1. Geometrically, the nanodots are best described as truncated hemispheres, as all the structures are ~100 nm tall, regardless of base diameter, due to the lift-off

fabrication method. The individual nanodots are polycrystalline, with a mixture of (111) and (200) crystallites and a crystallite size of ~25 nm, based on X-ray diffraction measurements on a similarly prepared Al thin film.

After coating with PECVD a-Si, the Al nanodot arrays were transformed into arrays of regularly spaced CSNs that are firmly attached to the underlying Si substrate. This is shown schematically in Fig. 4.2, along with representative AFM images of CSNs with 100, 200, and 300 nm core diameters, all with 300 nm shell thicknesses. As a result of the shell skirting between structures, the final CNS height is still ~100 nm when measured by AFM, with some statistical variations from both the Al deposition and a-Si deposition processes.

4.2 Nanoindentation Experiments

The mechanical behavior of the CSNs was characterized by displacement-controlled nanoindentation. A spherical diamond tip of 1 μm radius of curvature was used to indent individual CSNs with a displacement rate of 3 nm/s while simultaneously measuring the applied force. The relatively large tip radius, as compared to the CSN size, was chosen to provide compression loading to the CSNs, rather than indenting the structures.

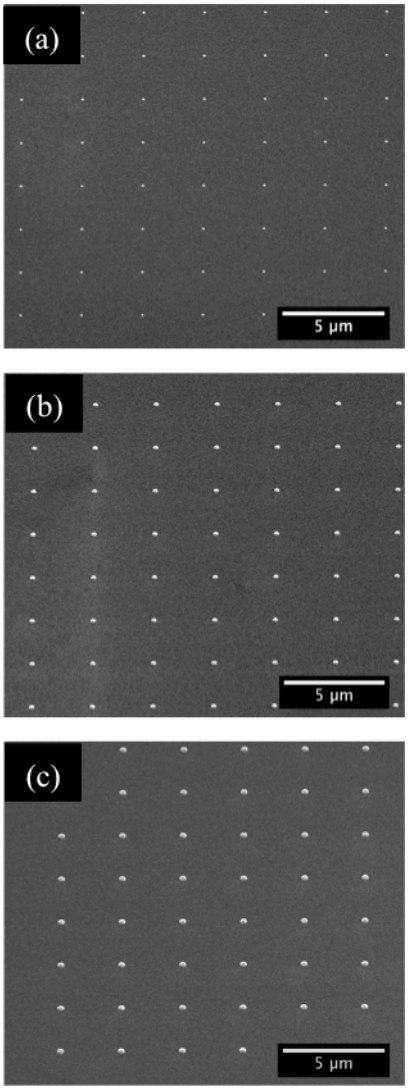

Fig. 4.1: SEM micrographs of Al nanodot arrays with 100 nm (a), 200 nm (b), and 300 nm (c) structure base diameters.

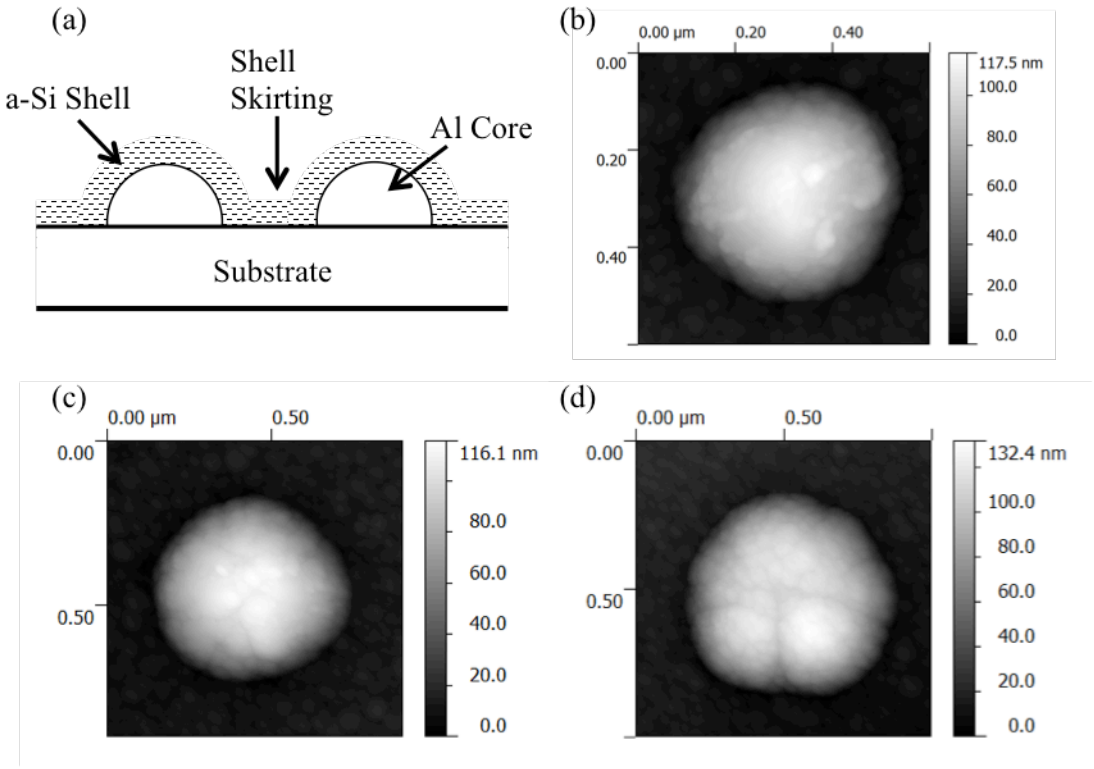

Fig. 4.2: Schematic of the CSN geometry (a), along with representative AFM images of CSNs with 100 nm (b), 200 nm (c), and 300 nm (d) core base diameters, all with 300 nm shell thickness.

4.2.1 Load-Displacement Behavior of CSNs with 100 nm Core Diameters

Representative load-displacement curves for 20, 40, 60, and 80 nm indentations on CSNs with 100 nm diameter cores and 300 nm shell thickness are shown in Fig. 4.3. The indenter displacement returns to zero (or nearly to zero) for all loading conditions, indicating that very little residual deformation remains after indentation. Several types of indentation response are observed as a function of maximum indenter displacement, which are summarized in Table 4.1. The indentation response is either elastic or a small hysteresis loop for 20 nm indents, which indicates that this loading is at or near the elastic limit of the structures. For the 40 nm indents, the load-displacement response is characterized by a smooth loading curve, along with an unloading curve with a slope inflection at a load of ~100 μN that serves to bring the residual displacement back to zero. At both 60 and 80 nm displacements, a large number of load-drops appear during loading. Then, during unloading, load-jumps occur in conjunction with a slope inflection. These indentation signatures represent microscopic events occurring beneath the indenter tip during loading and unloading.

Table 4.1: Indentation Response of CSNs

Indentation Depth	Maximum Indentation Load	Indentation Response
20 nm	108 μN	Elastic or Hysteresis Loop
40 nm	221 μN	Smooth Loading Curve Slope Inflection During Unloading
60 nm	336 μN	Load-Drops/Jumps Slope Inflection During Unloading
80 nm	359 μN	Load-Drops/Jumps Slope Inflection During Unloading

SPM images of a CSN before and after an 80 nm indent are shown in Fig. 4.4, along with the corresponding load-displacement curve. After indentation, the measured height of the CSN decreases by 3.4 nm, but the structure morphology remains hemispherical (up to the resolution of the SPM), with no residual impression left from the indenter tip. From the load-displacement data, a residual displacement of ~9.5 nm is observed after unloading. The discrepancy between the SPM measurements and the load-displacement data implies that additional recovery is occurring after the structure is fully unloaded. Regardless, this substantial deformation recovery beyond the elastic limit is especially remarkable considering the maximum indenter displacement is approximately 80% of the protruding structure height of ~100 nm.

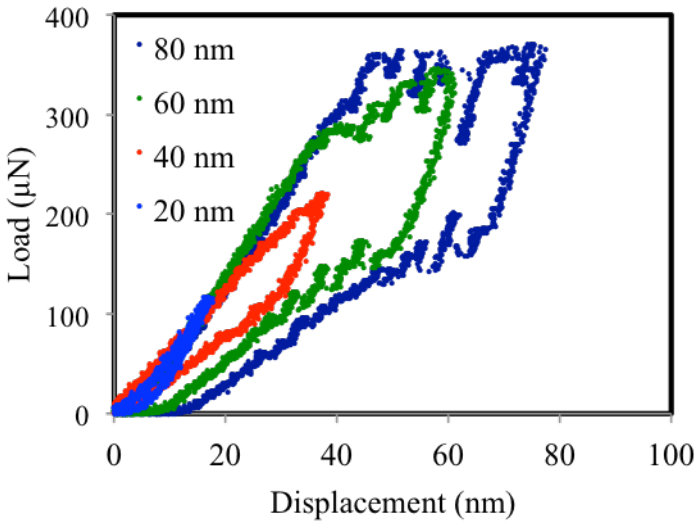

Fig. 4.3: Load-displacement curves for 20, 40, 60, and 80 nm indents on CSNs with 100 nm core diameters and 300 nm shell thickness.

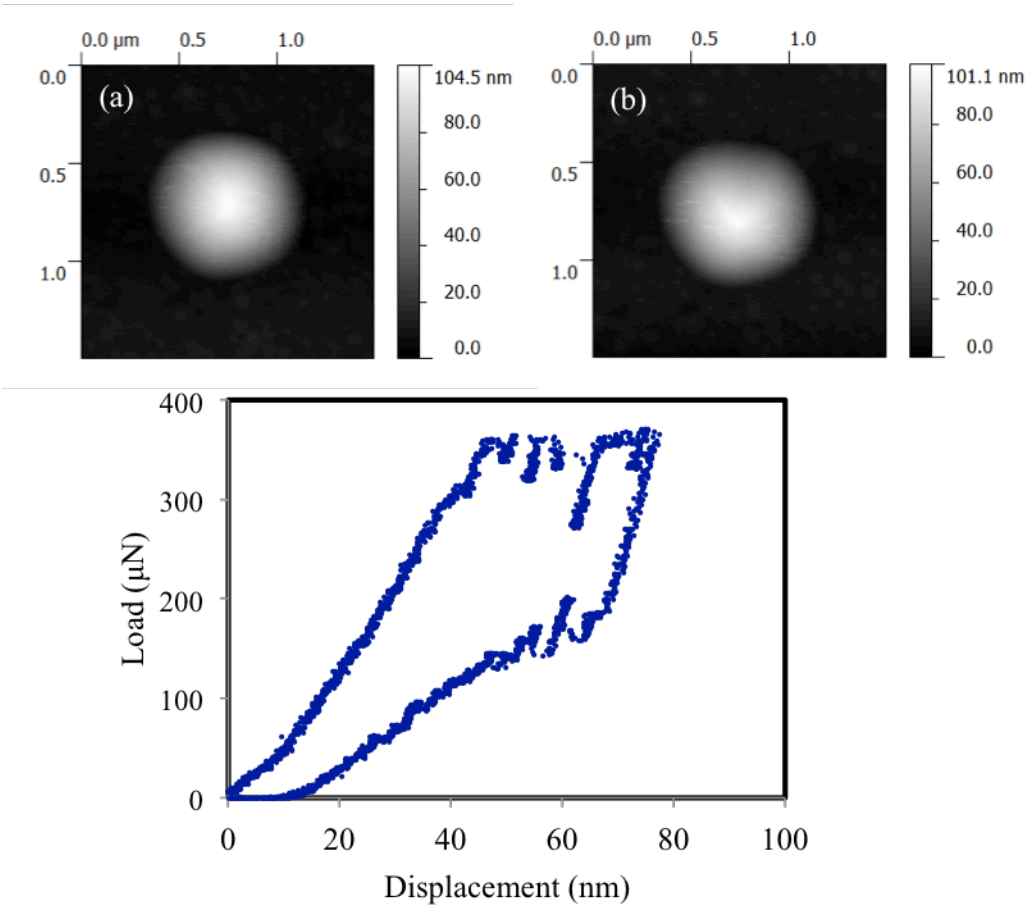

Fig. 4.4: SPM images of a CSN before (a) and after (b) an 80 nm indentation, along with the corresponding load-displacement curve (c).

4.2.2 Origin of the Indentation Signatures

The role the discontinuous indentation signatures play on the novel deformation-resistant properties of CSNs are not readily apparent. These signatures can be the result of dislocation nucleation events and their propagation in metals [124,143], phase transformations in semiconductors [144], fracture in brittle materials [145], and thin film delamination [146]; in general, the contribution from each source is potentially ambiguous and requires more detailed analysis. For Al/a-Si CSNs, the load-drops/jumps could potentially be attributed to dislocation activities in the Al core, pressure-induced phase transformations in a-Si, and shell fracture/delamination.

To gain further insight into the origin of the load-drops, multiple sequential indentations were performed on individual CSNs. Load-displacement curves for 4 sequential 80 nm indents on a single CSN are shown in Fig. 4.5, which show consistent hardening behavior after each indent. This hardening behavior suggests that neither shell delamination nor shell fracture can be the source of the observed load signatures, as elementary fracture mechanics predicts that these would both elicit a weakening effect in the CSNs. In addition, even if they occurred during loading, the formation of cracks or shell delamination could not be rationally correlated with the load-jumps observed during unloading on physical grounds.

The lack of cracks and shell delamination was further confirmed by high resolution SEM images of focused ion beam (FIB) milled cross-sections of an unindented CSN and a CSN that has been subjected to 4 sequential 1000 μN load-controlled indentations, shown in Fig. 4.6. In comparison to the unindented CSN, the apex of the indented nanostructure appears to be slightly flattened; however, it should be noted this CSN was indented to almost twice the maximum

contact load than the CSN characterized in Fig. 4.5. Even at this much larger contact load, no evidence of shell delamination or crack formation is observed.

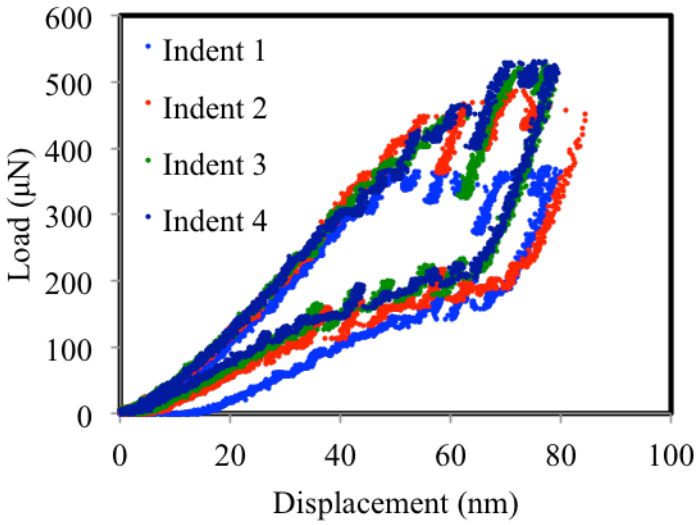

Fig. 4.5: Load-displacement curves for 4 repeated 80 nm indents on a CSN with 100 nm core diameter and 300 nm shell thickness. The maximum contact load increases after each subsequent indent, indicating hardening behavior.

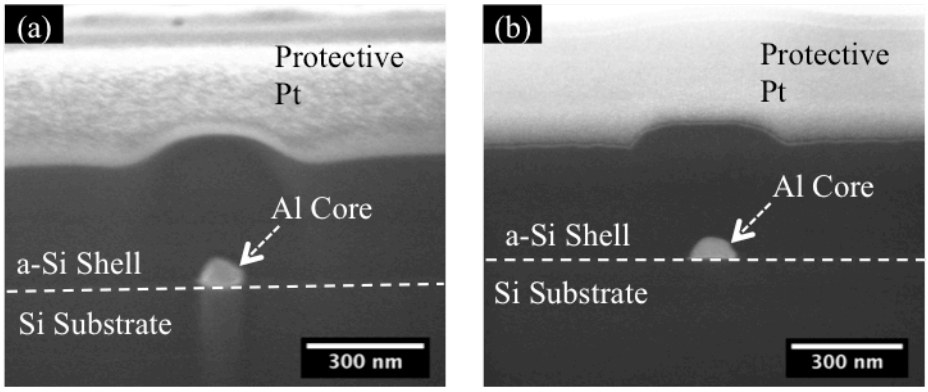

Fig. 4.6: High resolution SEM micrographs of FIB milled cross-sections of an unindented CSN (a) and a CSN after 4 sequential 1000 μN indentations (b), showing no evidence of shell delamination or crack formation.

In order to investigate the possibility of pressure-induced a-Si phase transformations as the source of the indentation signatures, load-controlled nanoindentation experiments were performed on a 300 nm smooth a-Si thin film fabricated with the same process conditions as the a-Si shells used to coat the CSNs. These phase transformations will typically appear as a pop-out or sharp slope inflection during the unloading portion of the load-displacement data [144,147], and are predicted to occur at contact pressures of 8.4 GPa, 16.25 GPa, and 19 GPa. As seen in Fig. 4.7, no evidence of a phase transformation is observed for contact pressures up to ~22 GPa. The elimination of shell delamination, shell fracture, and a-Si phase transformations as potential sources of the load-drops/jumps seen in the load-displacement curves strongly suggests that dislocation-based mechanisms in the Al core are instead responsible.

Further insight into the material deformation behavior can be found from analysis of the load vs. time and indenter displacement vs. time data. A plot of both contact load and indenter displacement vs. time for an 80 nm indent on an individual CSN is shown in Fig. 4.8. During loading, each drop in contact load corresponds to a forward indenter excursion as the contact stiffness suddenly and discontinuously decreases. More interesting, however, are the indenter signals observed during unloading, where each increase in the contact load correlates with an anomalous indenter retraction. Since this is a displacement-controlled indent, the only way the indenter can retract faster than the specified unloading rate is if something suddenly and unexpectedly pushes back against the indenter. This is a strong indication that the load-jumps during unloading are a result of rapid deformation recovery in the CSNs.

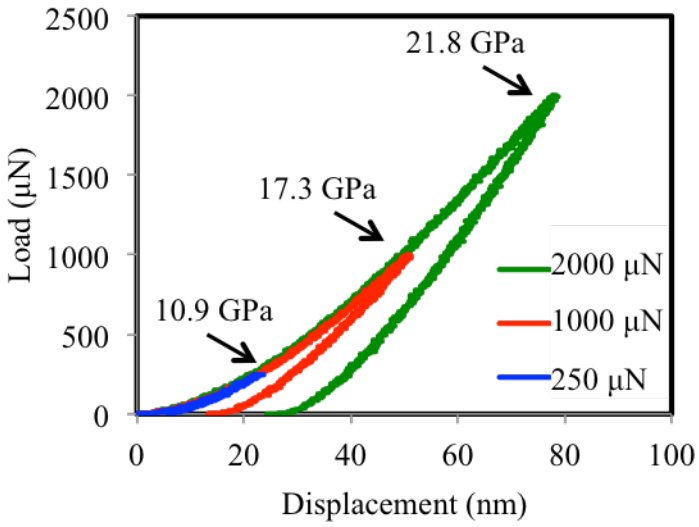

Fig. 4.7: Load-displacement curves for 250 μN, 1000 μN, and 2000 μN indents on a 300 nm a-Si thin film to investigate the existence of pressure-induced phase transformations. The estimated maximum contact pressures for each indent are indicated at the apex of each curve.

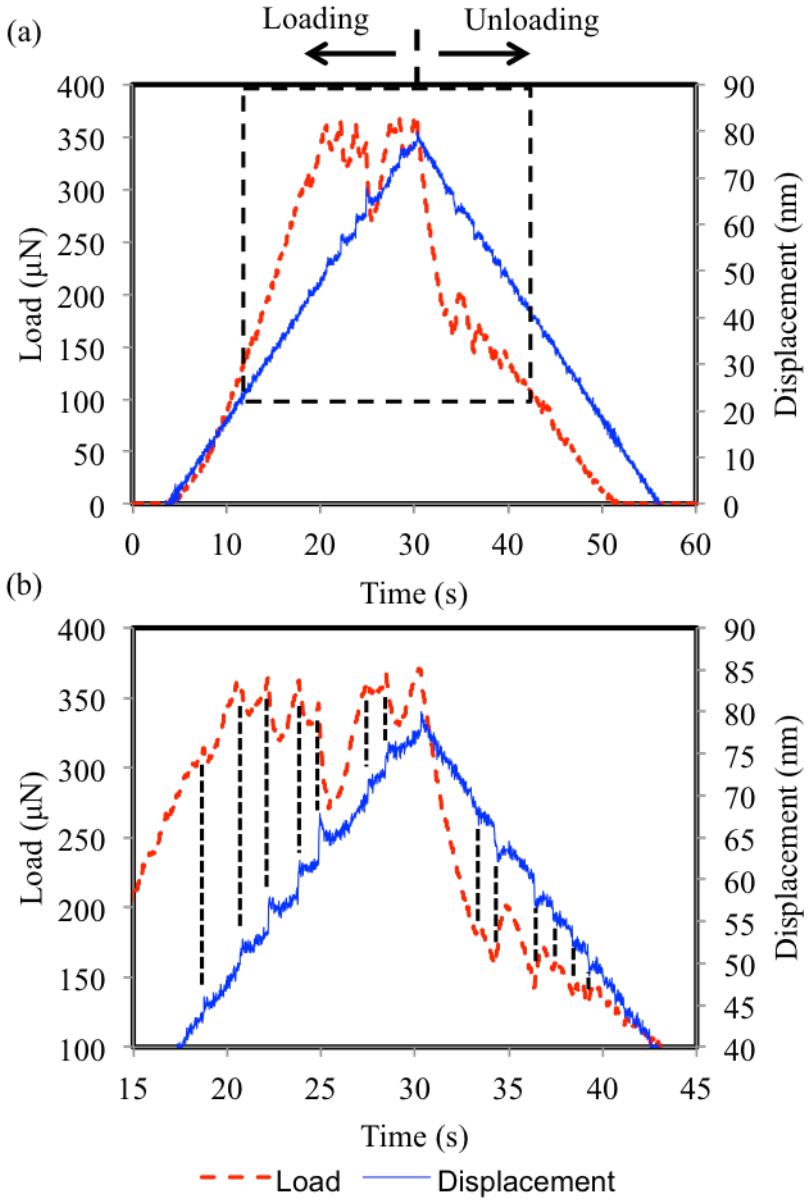

Fig. 4.8: Load and displacement vs. time curves for an 80 nm indent on a CSN with a 100 nm core diameter and 300 nm shell thickness (a); Zoom-in of the boxed area in (a) is shown in (b). During loading, load-drops are observed, in conjunction with a forward indenter excursion for each signature. During unloading, each anomalous increase in load correlates with a sudden indenter retraction.

Given the substantial amount of deformation recovery during unloading, it is not reasonable to expect that much of this deformation can be attributed to typically-brittle a-Si. This is especially true for large indentation depths, as there is no evidence to suggest such large recoverable deformations of a-Si should be possible. Since very little residual deformation is observed and the CSNs remain hemispherical after nanoindentation, it is very likely that the harder and stronger a-Si shell acts a vehicle to transmit stress to the Al core, and the primary deformation occurs due to compression of the softer Al core between the harder shell and Si substrate. At 20 nm indentation depth, where the CSNs behave elastically, the indenter is likely only interacting with the a-Si shell due to the relatively large thickness of the shell and the shallow indentation depth. As the indentation depth increases to 40 nm, the Al core is elastically compressed between the shell and the substrate, and during unloading, the elastic recovery correlates with the slope-inflection seen in the load-displacement curve. Further increases in indentation depth result in plastic deformation within the Al core, as indicated by the load-drops during loading that correspond to the nucleation and propagation of dislocations in the 60 and 80 nm indentations.

With the knowledge that dislocation activities in the Al core play a vital role in the mechanical behavior of these structures, new insights into the mechanisms that enable deformation resistance can be attained. In accordance with previous hypotheses [22,78,79], the existence of reverse plastic deformation depends on the generation of a sufficient back-stress to cause dislocations to retrace their paths or otherwise annihilate during unloading. For CSNs, this back-stress is generated as the confined core volume is compressed between the hard a-Si shell

and Si substrate. As the core diameter is increased, the confinement is reduced, which should have an effect on the mechanical behavior of these structures.

4.2.3 Effects of Confined Core Volume

To explore the role of the size of the confined core volume, nanoindentation experiments were conducted on CSNs with 100, 200, and 300 nm core diameters and 300 nm shell thickness. Load-displacement curves for 60 and 80 nm indents on these structures are shown in Fig. 4.9. For the 60 nm indents, load-drops/jumps are observed for the 100 nm core CSN, as expected. As the core diameter increases, the indentation signatures are at first partially suppressed, as seen for the CSN with the 200 nm core diameter, resulting in a load-displacement response similar to that seen in Fig. 4.3 for a 40 nm indent on a CSN with a 100 nm diameter core and 300 nm shell thickness. The occurrence of these load-drops/jumps indicates that a sufficient back-stress to trigger dislocation annihilation during unloading can be generated in this structure. With a further increase in core diameter, the displacement behavior completely changes, with full suppression of the load-drop/jump signatures. In addition, a residual displacement of 12.8 nm is seen in the load-displacement data. Similar results are obtained for the 80 nm indents.

It is worth noting that while core confinement is important for these structures, deformation resistance is not achieved for arbitrary shell thicknesses. Fig. 4.10 shows load-displacement curves for 80 nm indents on CSNs with 100 nm core diameters and 100 and 300 nm shell thicknesses, as well as SPM images of CSN height before and after indentation. While load-drops/jumps and reverse plastic deformation are present in both curves, more deformation recovery is observed with the 300 nm shell thickness compared to the 100 nm shell thickness.

According to the SPM images, the height of the CSN with the 100 nm shell thickness decreases by 10.9 nm, compared to only 3.6 nm for the CSN with the 300 nm shell thickness. As mentioned previously, it is not reasonable to expect that this deformation be localized to within the a-Si shell. Rather, much of the deformation occurs as the soft Al core is compressed between the hard a-Si shell and Si substrate. Since both of these CSNs are indented to a depth of 80 nm, the thinner shell results in higher stress being transmitted to the Al core due to the close proximity of the core to the location of indentation contact, and this higher stress results in more plastic deformation than can be recovered. Clearly, core size, shell thickness, and indentation load/displacement can affect the desirable deformation-resistant properties of Al/a-Si CSNs, which will allow for further optimization of the CSN properties.

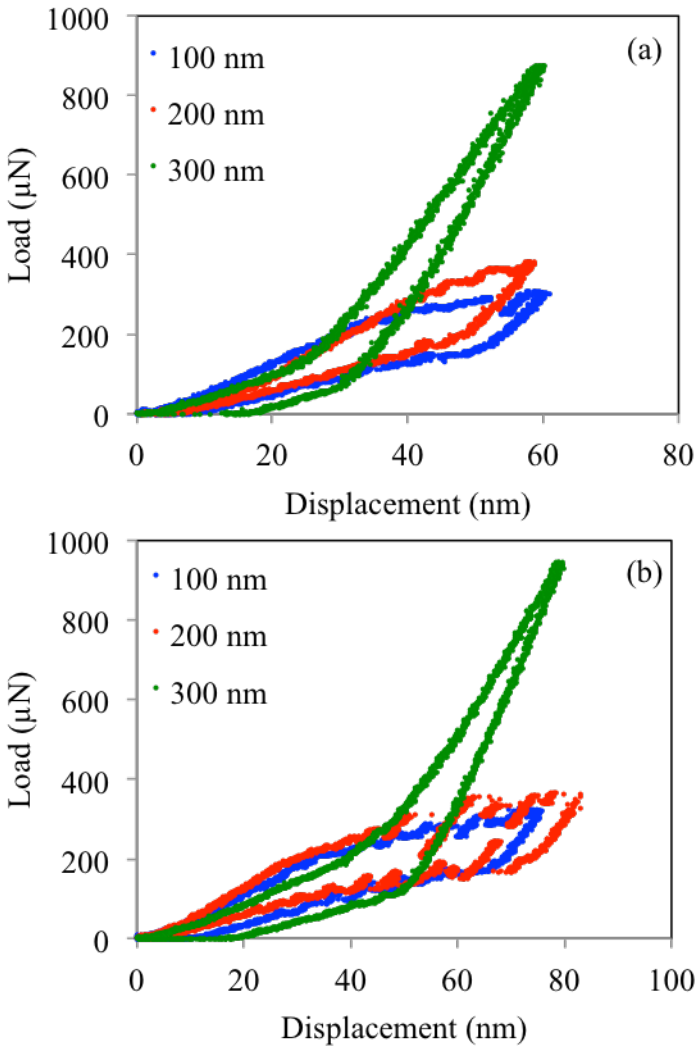

Fig. 4.9: Load-displacement plots for 60 nm indents (a) and 80 nm indents (b) on CSNs with 300 nm shell thickness and 100, 200, and 300 nm core base diameters.

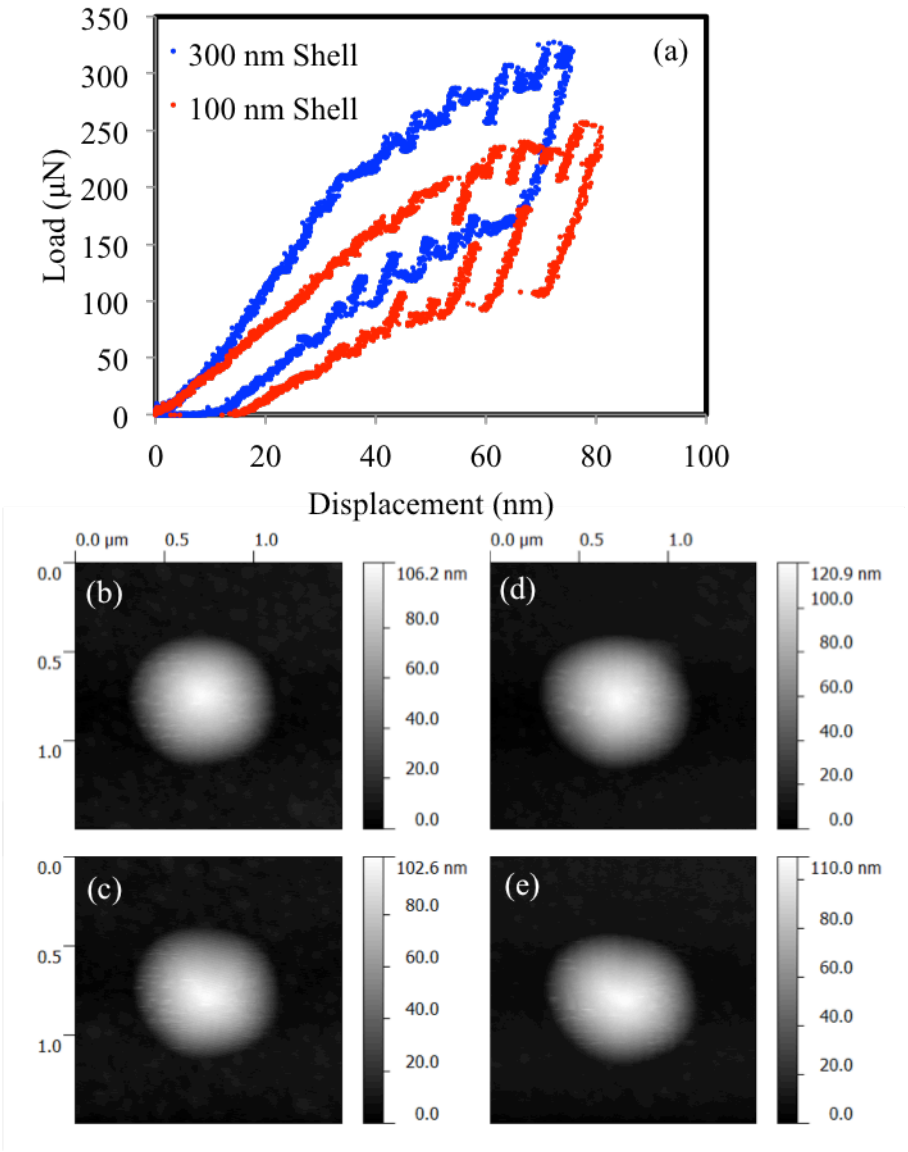

Fig. 4.10: Load-displacement plots for 80 nm indents on CSNs with 100 nm core base diameters and 100 and 300 nm shell thicknesses (a); SPM images of the 300 nm shell structure before (b) and after indentation (c); SPM images of the 100 nm shell structure before (d) and after indentation (e).

4.3 Molecular Dynamics Simulations

MD nanoindentation simulations were performed on CSNs and Al nanodots to study the underlying dislocation dynamics in these structures, with an emphasis on how the size of the confined core volume affects the dislocation behavior within the Al core. CSNs with core diameters of 20 and 30 nm, both with 10 nm shell thicknesses, were subjected to 9-11 nm indents. Prior to indentation, the potential energy of each system was minimized using a conjugate gradient method with a relative energy tolerance of 10^{-6}, followed by equilibration to 300 K with a Nosé-Hoover thermostat [113]. Dislocation activities within the Al core were visualized using the dislocation extraction algorithm (DXA) within the Open Visualization Tool (OVITO).

4.3.1 Dislocation Dynamics During Nanoindentation

Atomistic snapshots of dislocations generated during nanoindentation simulations in both the core of a CSN with a 20 nm diameter core and a 10 nm shell thickness, as well as a 20 nm diameter Al nanodot, are shown in Fig. 4.11. The dislocations are colored by Burgers' vector, with perfect FCC, Shockley partial, Hirth, stair-rod, and other dislocations colored blue, green, yellow, purple, and red, respectively. In this illustration, these structures have comparable maximum dislocation densities of $7.02 \cdot 10^{16}$ m^{-2} and $1.00 \cdot 10^{17}$ m^{-2} for the CSN and Al nanodot, respectively; additional dislocations may be obscured by the visualization perspective. For the CSN, dislocations are first nucleated at the Al/a-Si interface and propagate into the Al core during loading, eventually reaching a maximum dislocation density at the maximum indenter displacement. Upon unloading, the number of dislocations within the core decreases as dislocations are absorbed by the Al/a-Si interface or annihilate through reactions with other

dislocations. This process continues even after the indenter loses contact with the structure after unloading, eventually leading to the complete removal of all the dislocations in some circumstances. In comparison, the dislocation content within the Al nanodot is far more stable, with less dislocation annihilation occurring during unloading.

A more detailed look at the underlying dislocation dynamics yields some interesting observations about the behavior of dislocations in these structures. In the CSN, dislocations are first nucleated at the core-shell interface, and the resulting dislocation content at the maximum indenter displacement is primarily composed of glissile Shockley partials, as shown in Fig. 4.12. The high proportionality of mobile dislocations leads to significant egression of dislocations when the stress generated within the core is relieved during unloading, as indicated by the dislocation content within the core 22,000 time steps later. As these dislocations begin to be absorbed by the core-shell interface, the remaining sessile dislocation structures can become destabilized due to reactions with passing mobile dislocations, a phenomenon that has also been documented in MD simulations of amorphous/crystalline nanolaminates [148]. Note that further dislocation annihilation occurs after this time step, eventually leading to the dislocation-free state seen in Fig. 4.11.

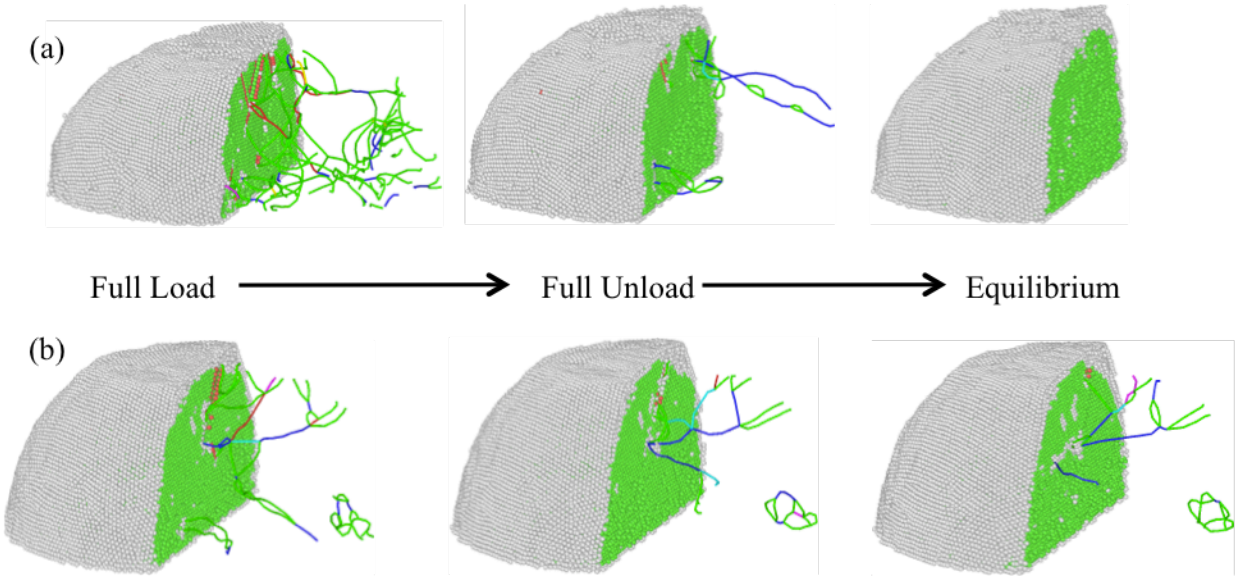

Fig. 4.11: Atomistic snapshots of dislocation content in the core of a CSN with a 20 nm core diameter and 10 nm shell thickness (a) and an Al nanodot with a 20 nm diameter (b) during nanoindentation simulations.

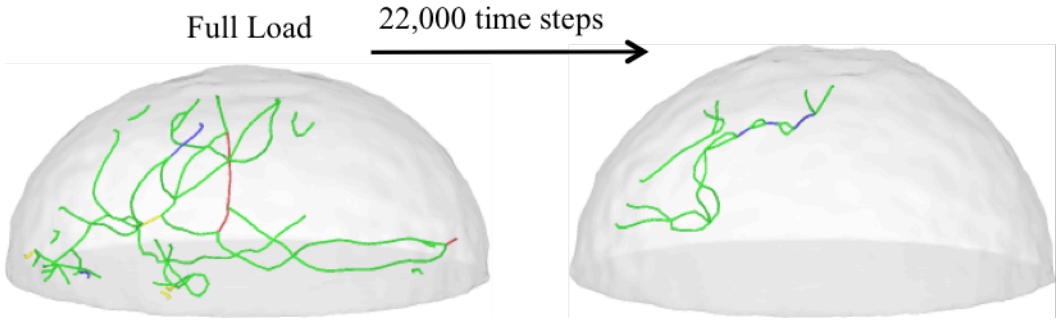

Fig. 4.12: Dislocation content in the core of a CSN with a 20 nm core diameter and 10 nm shell thickness, showing the egression of dislocations over time during unloading.

Dislocations in the Al nanodot are instead nucleated at or slightly below the nanodot surface, which is in good agreement with the location of maximum shear stress predicted from contact mechanics theory for sphere-on-sphere contact with radii of 10 nm (nanodot) and 100 nm (indenter) and a contact interference of 2 nm. In contrast to the CSN, more prominent sessile dislocations structures involving Hirth dislocations, Frank dislocations, and Lomer-Cottrell locks are formed within the Al nanodot, as shown in Fig. 4.13. This disparity in mobile vs. sessile dislocations formed within the two structures is perhaps the result of the difference in dislocation nucleation site, i.e., heterogeneous nucleation at the interface in the CSN and homogenous nucleation in the Al nanodot.

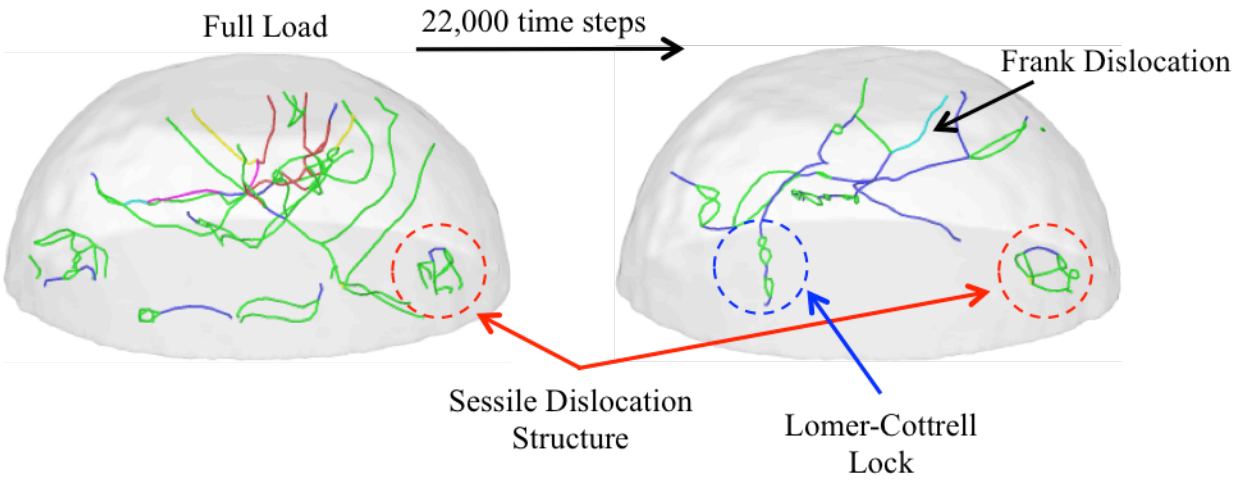

Fig. 4.13: Dislocation content in a 20 nm diameter Al nanodot. Significantly less dislocation annihilation occurs compared to the CSN due to the formation of sessile dislocation structures, Lomer-Cottrell locks, and Frank dislocations.

4.3.2 Effects of Core Size on Dislocation Density

To characterize the dislocation content within the Al core at various points during the indentation process, the dislocation densities at maximum indenter depth (full load), immediately after the indenter loses contact with the CSN during unloading (full unload), and at equilibrium after indenter removal were calculated. Fig. 4.14 shows the calculated dislocation densities at several different maximum indenter displacements for CSNs consisting of 20 and 30 nm diameter cores, both with 10 nm shell thicknesses, as well as a 30 nm diameter Al nanodot. Furthermore, these values are summarized in Table 4.2. For the CSN with the 20 nm core diameter, 82% of the nucleated dislocations are removed from the core during unloading of a 9 nm indent, eventually reaching 100% removal at equilibrium. As the indentation depth is increased to 10 nm, fewer dislocations (64%) are removed at full unloading, while still reaching full removal at equilibrium. Finally, for the 11 nm indent, the dislocation removal at full unloading again decreases to 57%; in addition, dislocations are still present in the core volume even at equilibrium, with a residual dislocation density of 11% remaining. As the core diameter increases to 30 nm, dislocations are less readily removed from the core volume during unloading. For this structure, the reduction of dislocation content at equilibrium is 100%, 81%, and 71% for the 9, 10, and 11 nm indents, respectively. Far less dislocation annihilation during unloading is observed in the Al nanodot. Although the nanodot is subjected to lower maximum indenter displacements due to the lack of a shell, the resulting dislocation densities at full load are comparable to those of the CSNs. For these simulations, the amount of dislocation recovery at equilibrium ranges from 53%-61%, depending on indentation depth. Clearly, confinement of the Al core by the a-Si shell correlates with improved dislocation removal during unloading. In addition, smaller confined core volume further correlates with improved dislocation removal,

which supports the hypothesis that core confinement is a critical component to the deformation-resistant properties of Al/a-Si CSNs.

Table 4.2: Calculated Dislocation Densities from MD Nanoindentation Simulations of CSNs and Al Nanodots

Nanostructure	Indentation Depth	Maximum Load	Fully Unloaded		Equilibrium	
		ρ ($1/m^2$)	ρ ($1/m^2$)	Dislocation Recovery	ρ ($1/m^2$)	Dislocation Recovery
CSN (20 nm Core)	9 nm	$7.02 \cdot 10^{16}$	$1.29 \cdot 10^{16}$	81.6%	0	100%
	10 nm	$1.82 \cdot 10^{17}$	$6.60 \cdot 10^{16}$	63.6%	0	100%
	11 nm	$2.33 \cdot 10^{17}$	$9.96 \cdot 10^{16}$	57.3%	$2.60 \cdot 10^{16}$	88.8%
CSN (30 nm Core)	9 nm	$1.29 \cdot 10^{16}$	$6.32 \cdot 10^{15}$	51.0%	0	100%
	10 nm	$8.32 \cdot 10^{16}$	$2.98 \cdot 10^{16}$	64.2%	$1.55 \cdot 10^{16}$	81.3%
	11 nm	$1.64 \cdot 10^{17}$	$8.58 \cdot 10^{16}$	47.7%	$4.80 \cdot 10^{16}$	70.7%
Al Nanodot (30 nm)	3 nm	$1.09 \cdot 10^{17}$	$6.97 \cdot 10^{16}$	35.8%	$5.07 \cdot 10^{16}$	53.3%
	4 nm	$1.61 \cdot 10^{17}$	$8.09 \cdot 10^{16}$	49.7%	$6.34 \cdot 10^{16}$	60.5%
	5 nm	$2.05 \cdot 10^{17}$	$1.11 \cdot 10^{17}$	45.7%	$8.39 \cdot 10^{16}$	59.0%

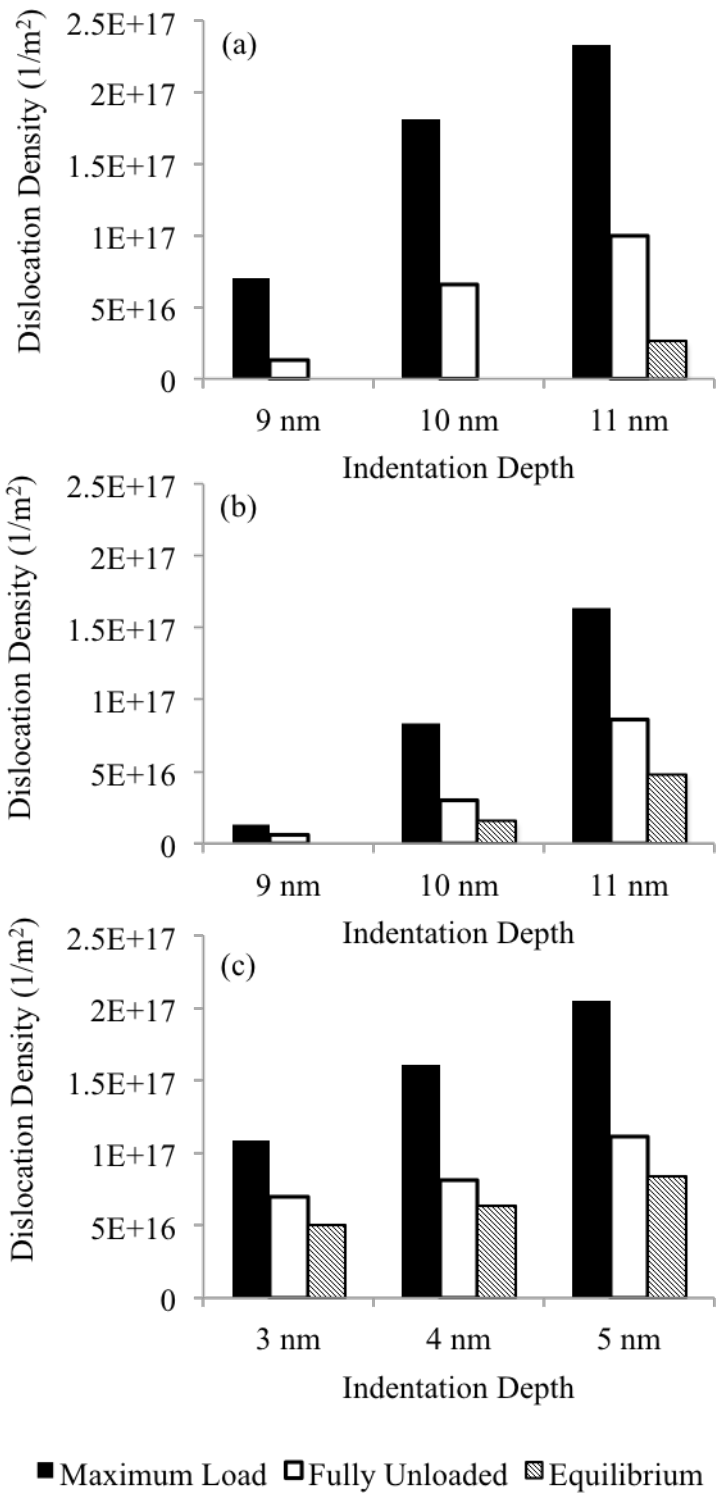

Fig. 4.14: Dislocation densities calculated from MD nanoindentation simulations for CSNs with 20 nm core diameter (a) and 30 nm core diameter (b) (both with 10 nm shell thickness) and a 30 nm diameter Al nanodot (c).

4.3.3 Back-stress Calculations

The stress state in the core of the CSNs during nanoindentation was also studied. Since the stress within the Al core is inhomogeneous due to the CSN shape and tip curvature, this was characterized by defining a volume-weighted state of stress for the entire core and tracking this value as a function of time during nanoindentation. In LAMMPS, atomic stress is calculated using an energy equation [149], meaning that the computed quantity actually has units of stress·volume. As a result, the actual per-atom stress would be obtained by dividing the computed quantity by the per-atom volume to calculate a true stress. However, the volume of an individual atom is ill-defined in a deformed solid. To resolve this limitation, a global state of stress within the core was calculated by first computing the per-atom stress tensor (which has units of stress·volume), summing the value of each component over all atoms in the core, and then dividing these summed components by the total core volume to produce a volume-weighted global stress tensor. Finally, the components of the global stress tensor were used to calculate the von Mises stress in the core. Of particular interest is the residual stress that the core relaxes to after unloading, which can be interpreted as the back-stress generated within the core. Plots of von Mises stress vs. time for 10 nm indents on CSNs with both 20 nm and 30 nm core diameters are shown in Fig. 4.15. A substantially larger back-stress is generated in the CSN with the 20 nm core (208 MPa) compared to the CSN with the 30 nm core (62 MPa). The concurrence of increased back-stress and improved dislocation annihilation in the CSN with the 20 nm core strongly indicates that the removal of dislocation from the core is mediated by the higher residual stress developed in these structures.

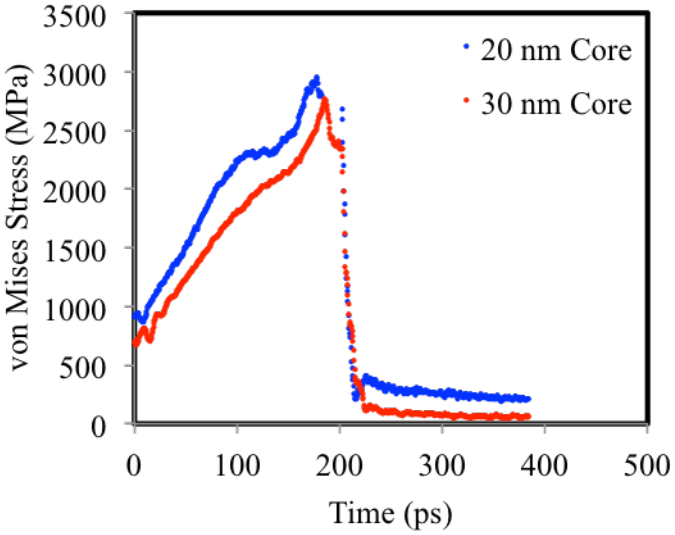

Fig. 4.15: Calculated von Mises stress in the core of CSNs with 20 and 30 nm core diameters during nanoindentation simulations. The residual stress after unloading is the back-stress generated in the core.

4.3.4 Insights from MD Simulations Applied to Experimental Results

The MD models demonstrate a significant egression of dislocations from single-crystal Al cores during unloading, with more dislocation annihilation occurring in CSNs with smaller cores. However, whereas the models use a single-crystal Al core, the as-fabricated Al cores are polycrystalline, with a grain size on the order of 25 nm. With this grain size, each 100 nm diameter Al core likely contains less than 25 grains, and the grain boundaries themselves can ostensibly act as sources for heterogeneous dislocation nucleation [150,151]. The annihilation mechanisms determined from the MD models likely very well describe the behavior of dislocations that are nucleated at the core-shell interface in grains on the surface of the Al core. For dislocations that are heterogeneously nucleated in the interior grains of the core far from the core-shell interface, the grain boundaries can act to obstruct dislocation motion and prevent the dislocations from annihilating at the core-shell interface. In this case, annihilation of dislocations may potentially be achieved by reverse dislocation motion enabled by the stress fields generated by dislocations piling up in front of grain boundaries, which has been observed in ultrafine grained Al during *in-situ* TEM experiments [68]. In the *in-situ* TEM experiments, the magnitude of reverse motion was large enough to result in dislocation annihilation at the original grain boundary source, due to the small grain size of the UFG Al (~500 nm, which is substantially larger than the grain size of the cores of the CSNs). It is plausible that such a mechanism could occur in the CSNs, with the dislocations that nucleate and propagate within interior grains moving back and annihilating at the nucleation source under the generated back-stress.

In consideration of MD length scales, there are significant computational challenges in modeling the polycrystalline structure of the CSN cores with 25 nm grains in order to capture similar deformation mechanisms to the experiments. The Hall-Petch strengthening mechanism predicts an increase in material strength with decreasing grain size due to dislocation pile-ups at grain boundaries. However, this behavior breaks down when the grain size is below a critical value (typically in the range of 10-50 nm [53]) and transitions to a so-called "inverse Hall-Petch" regime where material softening with decreasing grain size is observed. Below this critical grain size, dislocation nucleation events are largely suppressed [152], and the mechanical behavior is dominated by grain boundary sliding [54]. MD simulations of nanocrystalline Al show that the critical grain size is less than 18 nm [153], which is less than the 25 nm Al core grain size in the fabricated CSNs. This means that simulations of CSNs with polycrystalline cores having grain sizes smaller than 18 nm will be modeling a situation that is not consistent with the experiments. An MD simulation of a CSN with a realistic core grain size (~25 nm) and enough grains to form at least one interior grain will require a core diameter of at least 75 nm plus additional shell thickness.

Based on the experiments and simulations performed in this study, the material and geometrical properties that are sufficient to produce Al/a-Si CSNs with deformation-resistant properties are:

1. A core that supports dislocation-based plasticity,
2. A hard shell of suitable thickness to mitigate the transmission of stress into the core, and
3. A core volume small enough to allow the generation of a back-stress large enough to cause dislocation egression during unloading.

These guiding principles will potentially aid in the development of deformation-resistant CSNs from other material combinations, which will further enhance the understanding of the microscopic mechanisms that contribute to the mechanical behavior of these structures.

4.4 Conclusions

Nanoindentation experiments were performed to investigate the origin of the unique mechanical behavior observed in Al/a-Si CSNs. The results show that confinement of Al core, and particularly the size of confined core volume, are critically important for the deformation-resistant properties of these structures. Based on the indentation signatures exhibited by the CSNs with the smallest core diameter, the deformation behavior is mediated by dislocation activities within the confined core, with the deformation recovery resulting from dislocations retracing their paths or otherwise annihilating due to a back-stress generated during unloading. As the size of the confined core volume increases, the magnitude of this back-stress decreases, and deformation resistance is eventually completely suppressed as a result. Complimentary MD simulations show that smaller core diameters correlate with both a larger back-stress being developed and improved dislocation removal during unloading. These findings clarify the mechanisms that contribute to the desirable properties of Al/a-Si CSNs so that they can be designed to be effectively used in applications where the mechanical integrity of nanostructures is important.

CHAPTER 5

THE ROLE OF MATERIAL DIMENSIONALITY ON THE MECHANICAL BEHAVIOR OF AL/A-SI CORE-SHELL NANOSTRUCTURES

In chapter 4, the role of core confinement on the mechanical behavior of Al/a-Si CSNs was explored through experiments on CSNs with different core sizes. In this chapter, core confinement is instead studied in terms of the dimensionality of the confinement. Nanoindentation experiments were performed on hemispherical Al/a-Si CSNs, horizontally-aligned Al/a-Si core-shell nanorods (CSRs) with various core lengths, and an Al/a-Si layered thin film to study the effects of geometrical confinement of the Al core on the CSN deformation behavior. Whereas the CSNs have an unconventional load-displacement response characterized by no residual displacement after unloading when loaded beyond the elastic limit, a slight reduction in the geometrical confinement results in a loss of deformation resistance, as in the case of CSRs with the shortest rod length. Further decreases in core confinement result in conventional nanoindentation behavior, regardless of geometry. Supporting molecular dynamics simulations show that dislocations nucleated in the core of a CSN are more effectively removed during unloading compared to CSRs, which supports the hypothesis that the unique deformation resistance of Al/a-Si CSNs is enabled by 3-dimensional confinement of the Al core. The results presented in this chapter are based on a published study by Fleming *et al.* [154].

5.1 Nanostructure Morphology Characterization

Uniform arrays of Al nanodots and nanorods were deposited as the cores of the CSNs and CSRs, respectively, using the EBL and metal lift-off fabrication method. A schematic of the rod geometry is shown in Fig. 5.1; note that the specified rod length excludes the hemispherical end-

caps of each rod. A 100 nm thick Al thin film was also fabricated with thermal evaporation using the same deposition parameters as in the EBL procedure. SEM micrographs of 100 nm diameter Al nanodots and 100 nm, 500 nm, and 10 μm long Al nanorods (all with 100 nm rod diameters) are shown in Fig. 5.2. The Al nanostructures are polycrystalline, with a mixture of (111) and (200) crystallites, based on X-ray diffraction measurements of a similarly prepared Al thin film. Deposition of a-Si on these nanostructures results in a conformal shell on the nanostructures, as seen in SEM images in Fig. 5.3. Due to the conformal nature of the coating, the lateral dimensions of the visible portion of the individual nanostructures measured from the SEM images uniformly increases by 300 nm for both the CSNs and the CSRs, with only the top ~100 nm of the structure protruding from the surface. The diameter of the CSNs increases to 400 nm, while the width of the CSRs increases to 400 nm, regardless of core length, and the length of the CSRs increases by 300 nm compared to the lengths of Al nanorods. Some small-scale roughness is evident in the shell morphology, as seen in the AFM images in Fig. 5.4, but since it is substantially smaller than the tip radius used during nanoindentation, it is not expected to interfere with the mechanical characterization. All together, three different geometries of Al/a-Si nanostructures have been fabricated, each representing different levels of core confinement: hemispherical CSNs, in which the Al core is axisymmetrically confined by the a-Si shell and by the Si substrate; CSRs, which have reduced core confinement along the longitudinal axis of the rod; and an Al/a-Si layered thin film, where the Al layer is only confined between the Si substrate and the a-Si film, with no lateral confinement. These 3 geometries are shown schematically in Fig. 5.5.

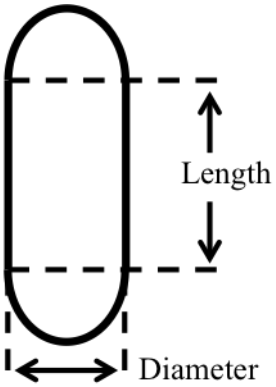

Fig. 5.1: Schematic of the nanorod geometry.

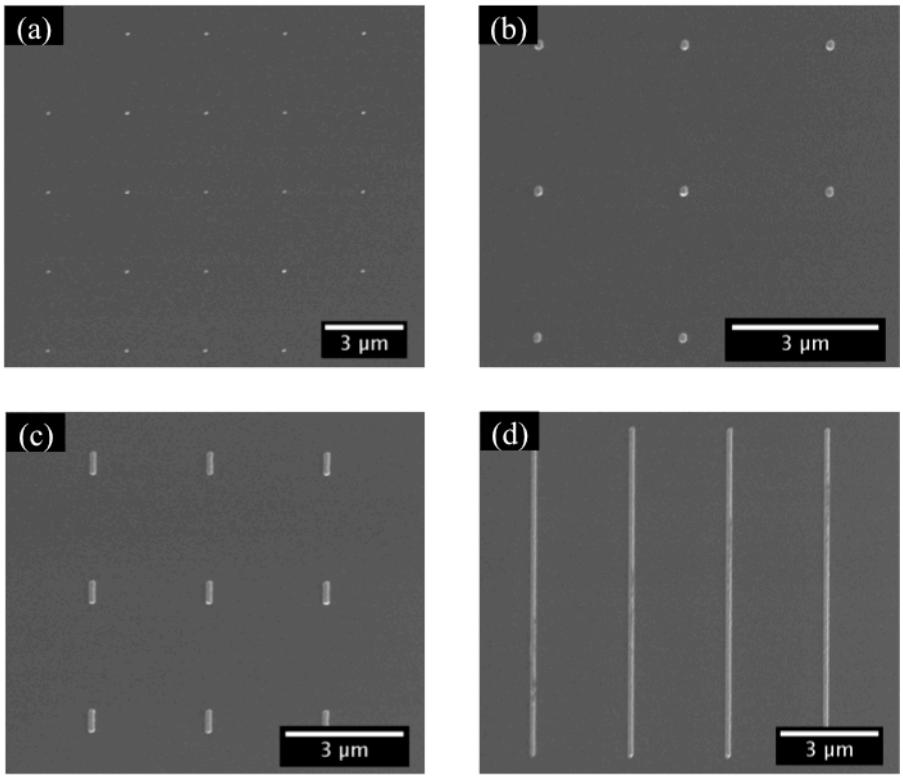

Fig. 5.2: SEM micrographs of 100 nm diameter Al nanodots (a) and horizontally-aligned Al nanorods with lengths of 100 nm (b), 500 nm (c), and 10 µm (d).

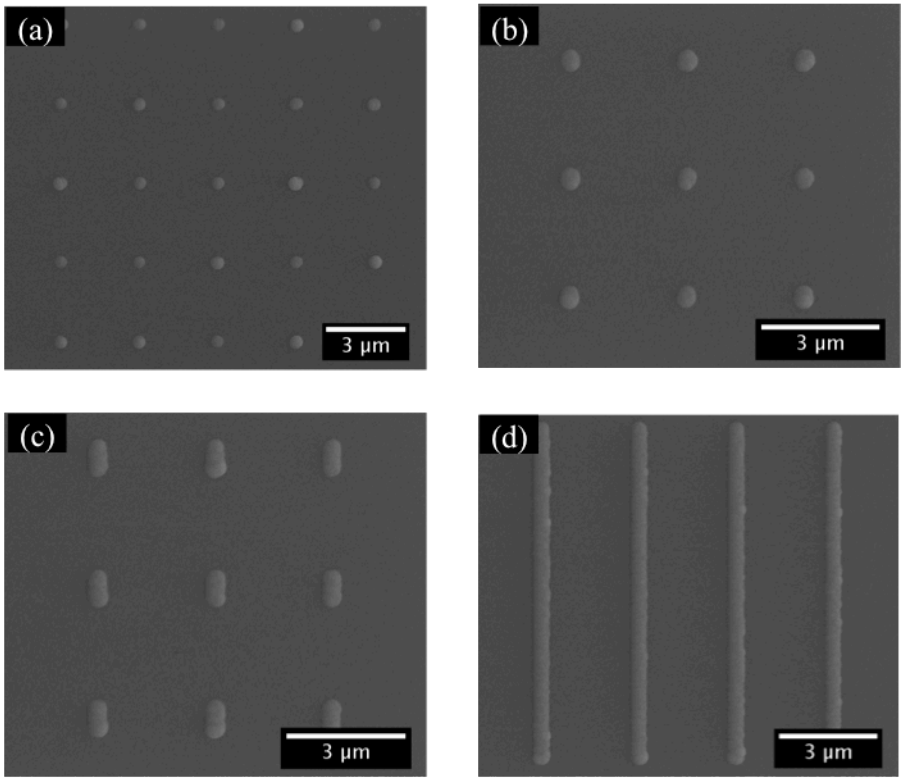

Fig. 5.3: SEM micrographs of CSNs (a) and CSRs with core lengths of 100 nm (b), 500 nm (c), and 10 µm (d).

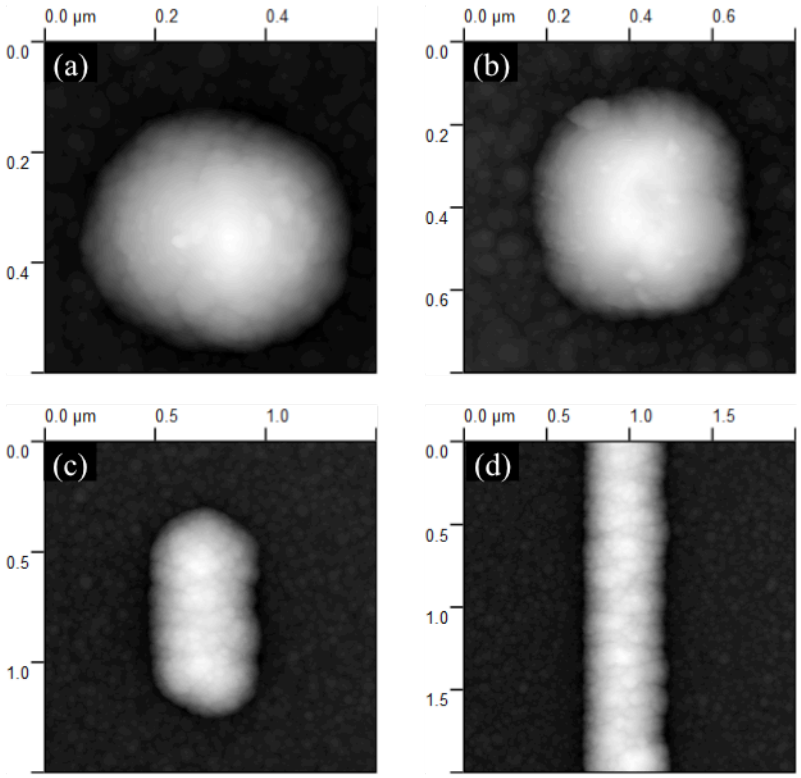

Fig. 5.4: AFM images of a CSN (a) and CSRs with core lengths of 100 nm (b), 500 nm (c), and 10 µm (d).

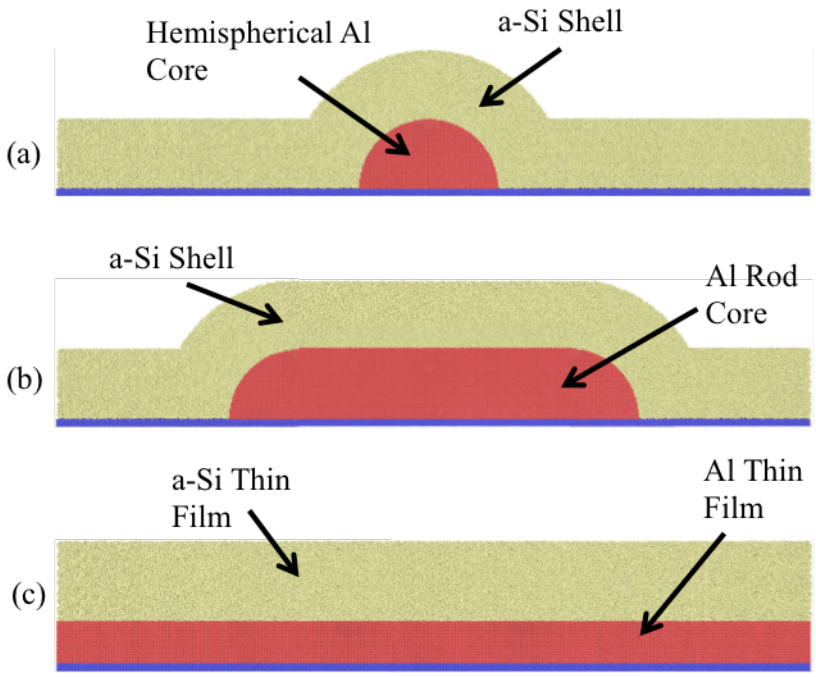

Fig. 5.5: Schematics of the three geometrical confinements: hemispherical core-shell (a), core-shell rod (b), and layered thin film (c).

5.2 Nanoindentation Experiments

The mechanical behavior of the CSNs, CSRs, and layered thin film was characterized using displacement-controlled nanoindentation with a spherical diamond tip of 1 μm radius of curvature and a displacement rate of 3 nm/s. The differences in mechanical behavior are qualitatively characterized in terms of load-displacement response, as well as quantitatively in terms of contact stiffness and residual displacement.

5.2.1 Deformation Resistance of CSNs

As detailed in Chapter 4, nanoindentation experiments were performed to characterize the mechanical response of hemispherical CSNs to compression loading. The CSNs exhibited nearly complete recovery of deformation beyond the elastic limit, as demonstrated in Fig. 5.6. This behavior was attributed to the generation of a back-stress in the Al core that induces dislocation annihilation during unloading. Development of this back-stress is dependent on confinement of the Al core by the hard a-Si shell, with higher stresses correlating with smaller confined core volumes. Ostensibly, the 3-dimensional axisymmetric core confinement of the CSNs plays a role in this behavior, and structures with reduced core confinement, namely horizontally aligned CSRs and layered thin films, should display different mechanical behavior as the core confinement is decreased.

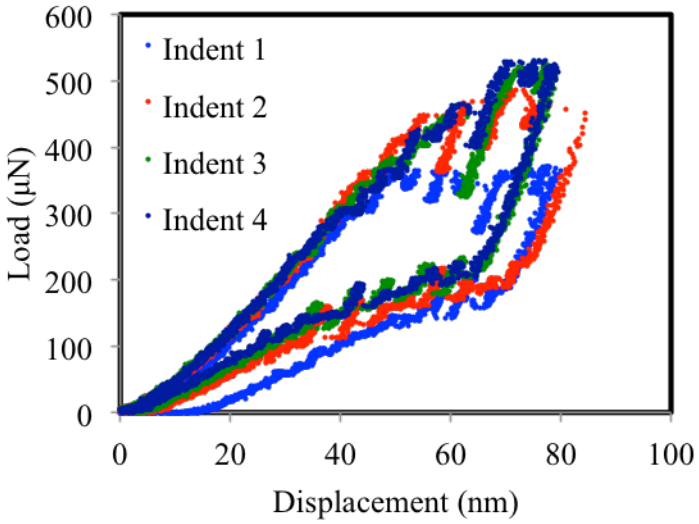

Fig. 5.6: Load-displacement curves for 4 repeated 80 nm indents on a CSN with 100 nm core diameter and 300 nm shell thickness.

5.2.2 Effects of Decreased Core Confinement

Nanoindentation experiments were conducted on CSRs with a core length of 100 nm to test this hypothesis. The elongated core of this structure breaks the axisymmetric core confinement of the CSNs, resulting in quasi-2-dimensional core confinement due to the additional core volume along the longitudinal axis of the rod. A load-displacement curve for an 80 nm indentation on a CSR is shown in Fig. 5.7, along with an AFM image of the structure morphology after indentation. The load signatures seen in the load-displacement data of the CSNs are still evident in the CSR, but the number and magnitude are significantly changed. For example, in the first indent in Fig. 5.6, approximately 9 load-drops and 8 load-jumps are observed, with average magnitudes of 13.7 μN and 10.7 μN, respectively. In comparison, approximately 4 load-drops and 5 load-jumps are seen in Fig. 5.7(a), with the indentation signatures dominated by a single, large magnitude signature, along with several much smaller secondary load signatures. During loading, a large load-drop with a magnitude of 63.2 μN occurs near the maximum indenter displacement, as well as 3 other load-drops with an average magnitude of 1.5 μN. Similarly, during unloading, a 30.2 μN load-jump occurs in addition to 4 other load-jumps with an average magnitude of 9.4 μN. In addition, the indenter displacement no longer returns to zero during unloading and residual deformation of the structure is clearly seen from the AFM image, meaning that the CSRs are not deformation-resistant.

Multiple repeated indents on a single CSR results in an increase in maximum indentation load after each indentation, as seen in the load-displacement curves for 4 sequential indents on a CSR in Fig. 5.8. Although this behavior was attributed to strain hardening in the CSNs, the residual deformation on the CSRs after indentation (Fig. 5.7(b)) results in an increase in contact

area for each subsequent indentation, which can also explain the increase in maximum indentation load for multiple indentations. Even so, the presence of load-drops and load-jumps suggests that dislocations activities within the confined Al core of the CSR still play a key role on the mechanical behavior, but the reduced confinement perhaps inhibits the ability of dislocations to annihilate during unloading. To further explore this, nanoindentation experiments were also performed on CSRs with core lengths of 500 nm and 10 μm, as well as an Al/a-Si thin film. Representative load-displacement curves for 80 nm displacement-controlled indents on all 5 geometries, including the hemispherical CSNs and the 100 nm CSRs, are shown in Fig. 5.9. As previously noted, the CSN has an unconventional mechanical response characterized by numerous discontinuous indentation signatures and deformation-resistant behavior as indicated by zero residual displacement after unloading. When the confinement of the Al core is slightly reduced, as in the 100 nm CSR, the number and magnitude of the observed indentation signatures are heavily reduced, along with the deformation resistance. As the core confinement is reduced further, however, there is a sharp transition in the mechanical behavior. The 500 nm and 10 μm CSRs, as well as the layered thin film, all have a more conventional load-displacement response, with no indentation signatures observed during loading and unloading and a substantial residual displacement evident in the load-displacement curve. This residual displacement accompanies the residual impressions left on the structures after indentation, as shown in SPM images in Fig. 5.10.

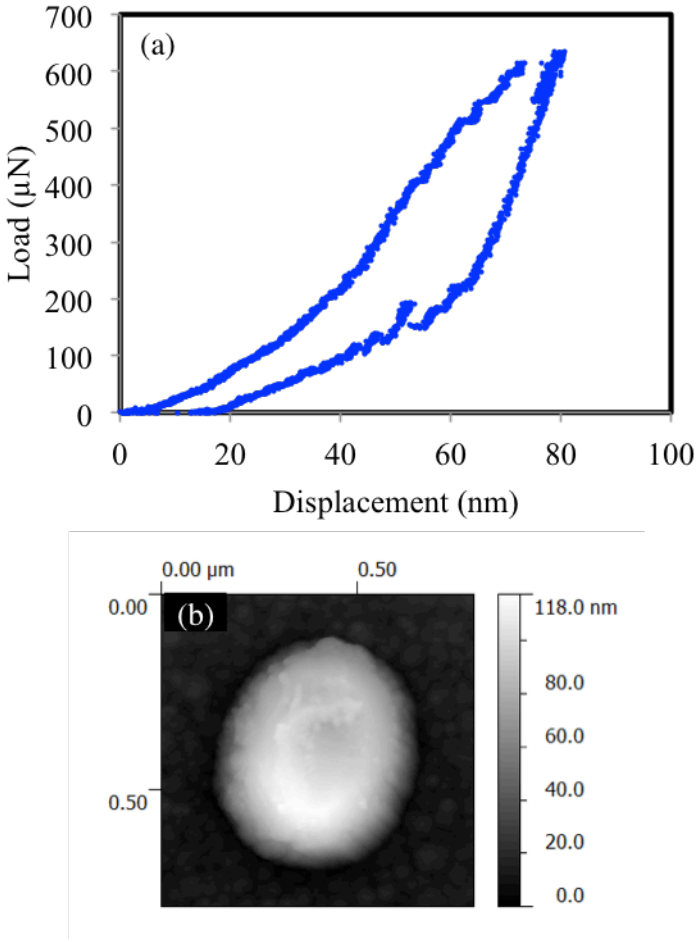

Fig. 5.7: Load-displacement curve for an 80 nm indent on a CSR with a 100 nm core length (a). The AFM image of the surface morphology of the CSR (b) clearly shows residual deformation after indentation.

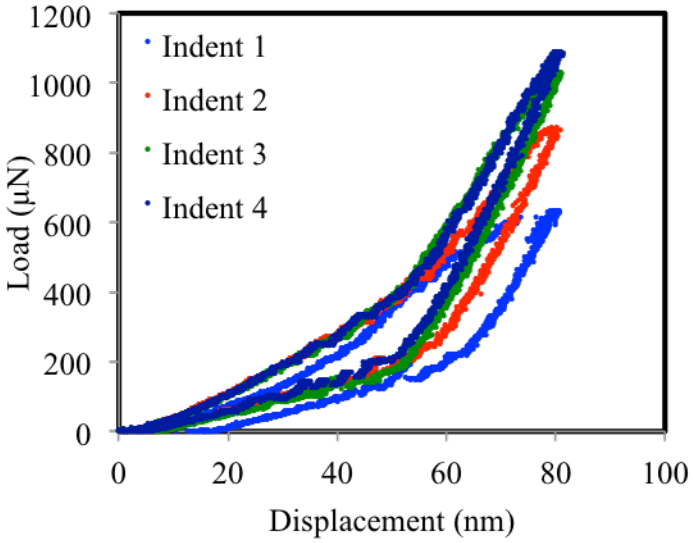

Fig. 5.8: Load-displacement curves for 4 repeated 80 nm indents on a CSR with a 100 nm core length. The indentation signatures are suppressed compared to the CSNs.

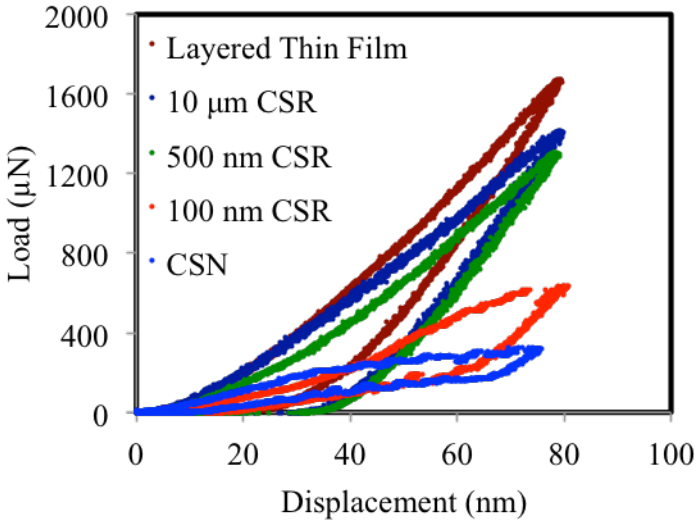

Fig. 5.9: Load-displacement curves for 80 nm indents on a CSN, CSRs with 100 nm, 500 nm, and 10 μm core lengths, and a layered thin film.

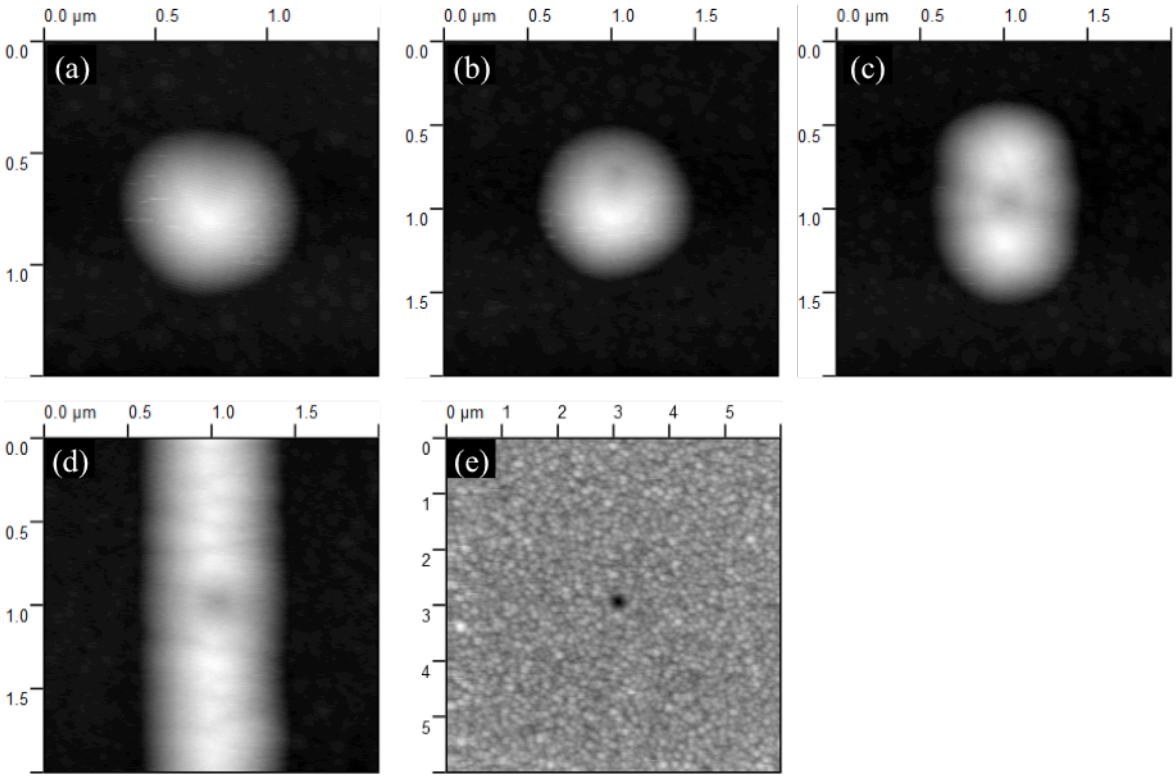

Fig. 5.10: SPM images of the surface morphology after 80 nm indents on a CSN (a), CSRs with 100 nm (b), 500 nm (c), and 10 µm (d) core lengths, and a layered thin film (e).

Analysis of the contact stiffness provides further insights into the mechanical behavior of these structures. A plot of contact stiffness vs. maximum indentation depth for all 5 geometries is shown in Fig. 5.11. For the CSNs, the contact stiffness increases with indentation depth up to 60 nm, at which point it becomes practically constant. Similar contact stiffness behavior is also observed in the 100 nm CSRs, which also show some evidence of dislocation activities during indentation, as noted in Fig. 5.7 and 5.8. The contact stiffnesses of the 500 nm CSRs, 10 μm CSRs, and layered thin film, however, all increase linearly with indentation depth, with values that generally overlap. In effect, the longer CSRs have a mechanical response that is largely indistinguishable from that of the layered thin film geometry. Moreover, the transition from the deformation-resistant behavior in the CSNs to the conventional indentation behavior of the layered thin films occurs abruptly, i.e., when the 3-dimensional core confinement of the CSN is reduced slightly, as in the 100 nm CSR, the deformation resistance and the accompanying indentation signatures are heavily reduced. More drastic reductions in core confinement result in a conventional indentation response, regardless of the dimensionality of the core confinement. As a result, it is very clear that 3-dimensional core confinement plays a critical role in the novel deformation-resistant behavior of Al/a-Si CSNs.

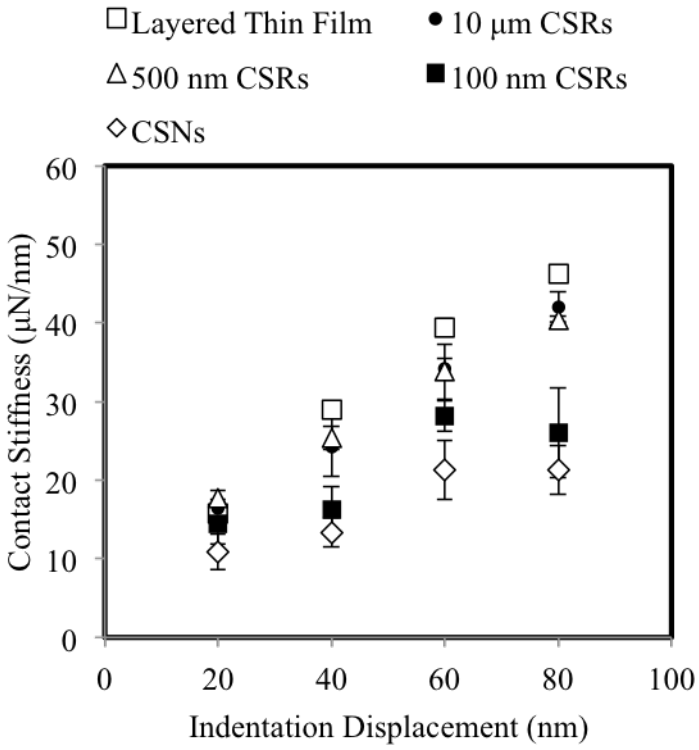

Fig. 5.11: Plot of contact stiffness vs. indentation displacement for a CSN, CSRs with 100 nm, 500 nm, and 10 μm core lengths, and a layered thin film.

5.3 Molecular Dynamics Simulations

Nanoindentation simulations were performed on several different geometries of Al/a-Si nanostructures: a CSN with a 15 nm core radius and CSRs with a rod radius of 15 nm and core lengths of 15, 25, and 35 nm, all with a 5 nm shell thickness. For these simulations, the indenter is controlled to move 6 nm into the nanostructure at a constant rate of 0.5 Å/ps while maintaining a system temperature of 300 K. After reaching the specified indenter displacement, the indenter is completely retracted at the same displacement rate.

5.3.1 Effects of Core Confinement on Dislocation Density

A snapshot of the atomic distortion resulting from dislocations nucleated in the core of a CSN at maximum indenter displacement is shown in Fig. 5.12(a). The core has been sliced down the middle to visualize an interior plain of atoms, which are colored by lattice structure. The green atoms are in a FCC arrangement and the red atoms are HCP atoms representing a stacking fault formed by the nucleation of Shockley partial dislocations. A more detailed view of the dislocation content is provided in Fig. 5.12(b), showing only the HCP atoms that primarily comprise the stacking faults, with the leading and trailing Shockley partials represented as green lines. As indicated, one pair of Shockley partials has cross-slipped into an adjacent slip plane. This cross-slipped dislocation structure is far less mobile than in-plane Shockley partial dislocations, which will potentially affect the dynamics of these dislocations after the removal of the applied indentation load. To visualize this, the time evolution of the dislocation content within the core is shown in Fig. 5.12(c), with all atoms removed to show only the dislocations within the interior of the core. The individual dislocation lines are colored by Burgers vector, with perfect FCC dislocations, Shockley partials, Hirth dislocations, and other dislocations

colored blue, green, black and red, respectively. As the nanostructure is indented, dislocations consisting primarily of glissile Shockley partials are nucleated at the core/shell interface and further propagate. This continues until a maximum dislocation density is reached at the maximum indenter displacement. During unloading, a notable egression of dislocations occurs as the mobile dislocations are reabsorbed by the core/shell interface. This continues even after the indenter loses contact with the CSN, eventually reaching an equilibrium dislocation density. A non-zero equilibrium dislocation density is typically due to the formation of sessile dislocation structures, either due to cross-slip (as demonstrated here) or other dislocation reactions. In this case, ~93% of the dislocations nucleated during loading have been reabsorbed by the core/shell interface or otherwise annihilated. Again, it should be noted that this phenomenon is specific to the core-shell structure, as similar simulations performed on Al nanodots result in stable dislocation densities that do not substantially decrease during unloading.

To characterize how the dimensionality of core confinement affects the behavior of dislocations in CSNs and CSRs, the dislocations densities at key points during the nanoindentation simulations were calculated. Fig. 5.13 shows the calculated dislocations densities at maximum indenter displacement, immediately after the indenter loses contact with the nanostructure during unloading, and at equilibrium (at least 85,000 time steps after the indenter has lost contact with the nanostructure); these values are summarized in Table 5.1. For the CSN, which is the structure with the most highly confined core, approximately 65.1% of the dislocations nucleated during indentation are removed when the structure is fully unloaded and further increases to 92.6% at equilibrium. When this confinement is reduced, as in the CSRs, the dislocation density relaxes to a nearly constant value when fully unloaded, regardless of core length, with minimal additional recovery occurring at equilibrium. For these structures, the

proportion of dislocations removed at equilibrium from the core of the CSRs decreases from 89.1% to 84.8% and then to 83.0% as the core length increases from 15 nm to 25 nm and 35 nm, respectively. The reduced lateral confinement exhibited in the CSRs allows more opportunity for dislocations to cross-slip or otherwise form sessile dislocations, such as Hirth or stair-rod dislocations, resulting in less dislocation recovery compared to the CSN.

Table 5.1: Calculated Dislocation Densities from MD Nanoindentation Simulations of a CSN and CSRs of Various Lengths

Nanostructure	Maximum Load	Fully Unloaded		Equilibrium	
	ρ ($1/m^2$)	ρ ($1/m^2$)	Dislocation Recovery	ρ ($1/m^2$)	Dislocation Recovery
CSN	$1.90 \cdot 10^{16}$	$6.62 \cdot 10^{15}$	65.1%	$1.40 \cdot 10^{15}$	92.6%
15 nm CSR	$3.63 \cdot 10^{16}$	$4.35 \cdot 10^{15}$	88.0%	$3.96 \cdot 10^{15}$	89.1%
25 nm CSR	$2.40 \cdot 10^{16}$	$3.59 \cdot 10^{15}$	85.0%	$3.65 \cdot 10^{15}$	84.8%
35 nm CSR	$2.37 \cdot 10^{16}$	$5.13 \cdot 10^{15}$	78.3%	$4.01 \cdot 10^{15}$	83.0%

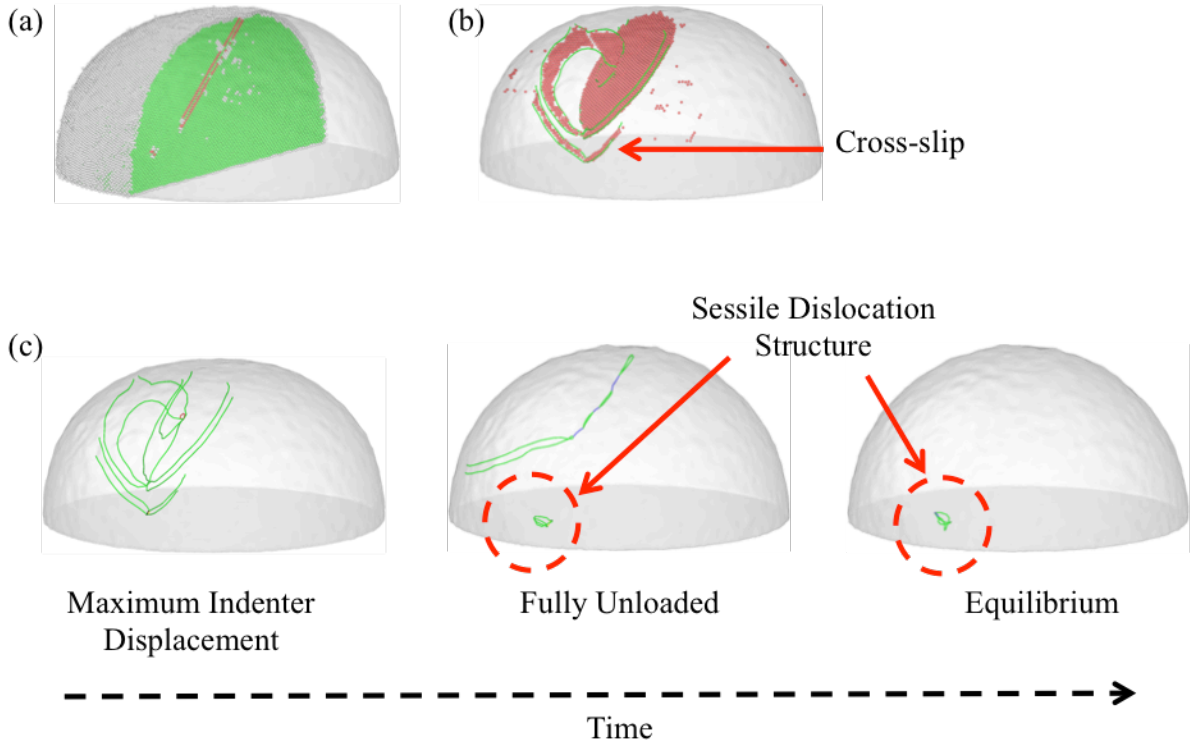

Fig. 5.12: A snapshot of atomic distortion resulting from dislocations nucleated in the core of a CSN (a); a snapshot of the dislocation content within the core, showing cross-slipped dislocations (b); and the time evolution of dislocation egression and sessile dislocation structure formation during unloading (c).

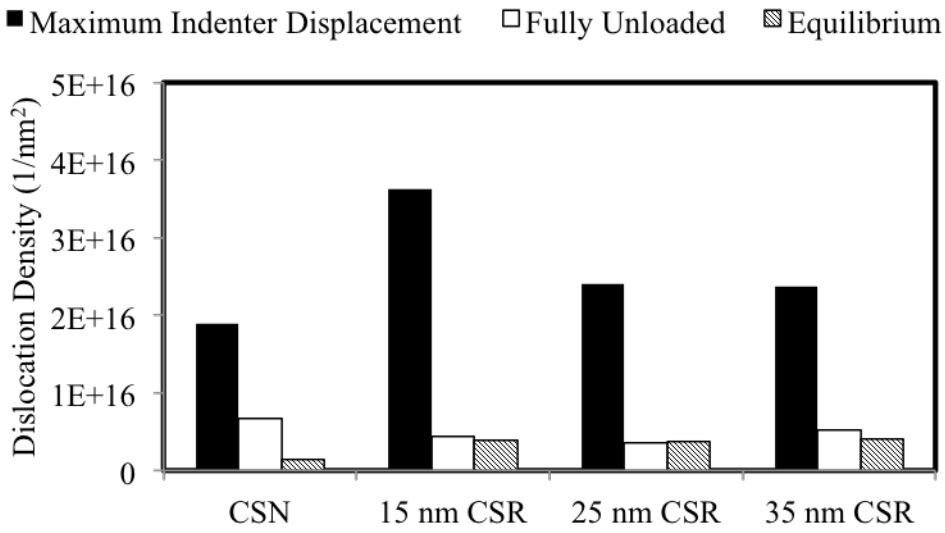

Fig. 5.13: Dislocation densities calculated from MD nanoindentation simulations for a CSN with a 15 nm core diameter and CSRs with various core lengths.

5.4 Conclusions

Nanoindentation experiments were performed on several different geometries of Al/a-Si nanostructures, including hemispherical CSNs, horizontally-aligned CSRs, and a layered thin film, to investigate the effects of geometrical confinement of the Al core on the CSN deformation behavior. The CSNs have deformation-resistant properties, as indicated by complete recovery of deformation beyond the elastic limit. When the core confinement is slightly reduced, the deformation resistance that is observed in the CSNs is substantially reduced. A further reduction in core confinement results in more conventional indentation behavior regardless of geometry. Supporting molecular dynamics simulations show that dislocations nucleated in the core of CSNs are more readily removed during unloading compared to CSRs, which indicates that the 3-dimensional core confinement of the CSNs plays an important role in the deformation-resistant properties of CSNs. This study elucidates the effects that core confinement plays on the novel nanoindentation behavior of hemispherical Al/a-Si CSNs, which will allow for the rational design and effective implementation of these structures in nanomechanical applications.

CHAPTER 6

TRIBOLOGICAL PROPERTIES OF NANOSTRUCTURE-TEXTURED SURFACES

Nanotextured surfaces can effectively reduce friction and adhesion, especially in applications with micro- and nanoscale contact interactions. However, for these surfaces, a common weakness is a lack of structural integrity of the individual nanotextures when subjected to contact loading, resulting in permanent deformation at even the moderate contact forces encountered in microscale systems. In this chapter, nanostructure-textured surfaces (NSTSs), comprised of arrays of novel Al/a-Si core-shell nanostructures (CSNs), have been developed with a desirable combination of low friction and high deformation resistance. Compared to Al nanodot-textured surfaces (ANDTSs), the NSTSs exhibit superior tribological properties. Specifically, when subjected to nanoscratch testing, the NSTSs have extremely low COFs (~0.015 at 8000 μN normal load), as well as no detectable nanostructure deformation at contact loads up to 8000 μN (estimated contact pressure greater than 1 GPa); the ANDTSs, in comparison, have higher COFs and are significantly deformed after scratch testing. In addition, the NSTSs have low adhesion (pull-off) forces on the order of less than 1 μN. The unique properties of NSTSs provide avenues for designing low friction, deformation-resistant surfaces that could potentially benefit a variety of fields, such as MEMS/NEMS, microelectronics, and magnetic recording. The results presented in this chapter are based on a published study by Fleming and Zou [155] .

6.1 Surface Morphology Characterization of ANDTSs and NSTSs

Using the EBL fabrication procedure, ANDTSs comprised of very uniform, densely packed arrays of polycrystalline Al nanodots were fabricated. SEM micrographs and

representative AFM topography profiles of ANDTSs with nanodot base diameters of 100, 200, and 300 nm and 1 μm structure pitch are shown in Fig. 6.1. As in Chapters 4 and 5, the ANDTSs were fabricated using a lift-off method, meaning that all the structures are approximately 100 nm tall, regardless of base diameter. The individual nanodots are polycrystalline, with a grain size of ~25 nm. As a result of this graininess, the height of each nanodot can potentially vary by up to ~25 nm, resulting in the subtle height variations seen in the AFM topography profiles. The areal surface roughness parameter S_a, calculated from 10x10 μm^2 AFM topography scans, is 5.9, 9.8, and 12.7 nm for nanodot diameters of 100, 200, and 300 nm, respectively.

To produce the NSTSs, these nanodot arrays were coated with a-Si, resulting in uniform arrays of CSNs that are rigidly attached to the substrate. The a-Si coating results in a uniform nanotextured surface, as can be seen from the SEM images and AFM topography profiles in Fig. 6.2. Due to the conformal nature of the coating, the diameter of the visible portion of the individual nanostructures measured from the SEM images increases by ~300 nm, with only the top ~100 nm of the structure protruding from the surface. The addition of the a-Si coating results in an increase in surface roughness of the NSTSs compared to the ANDTSs. For the NSTSs, the S_a values are 27.4, 37.5, and 40.3 nm for core diameters of 100, 200, and 300 nm, respectively.

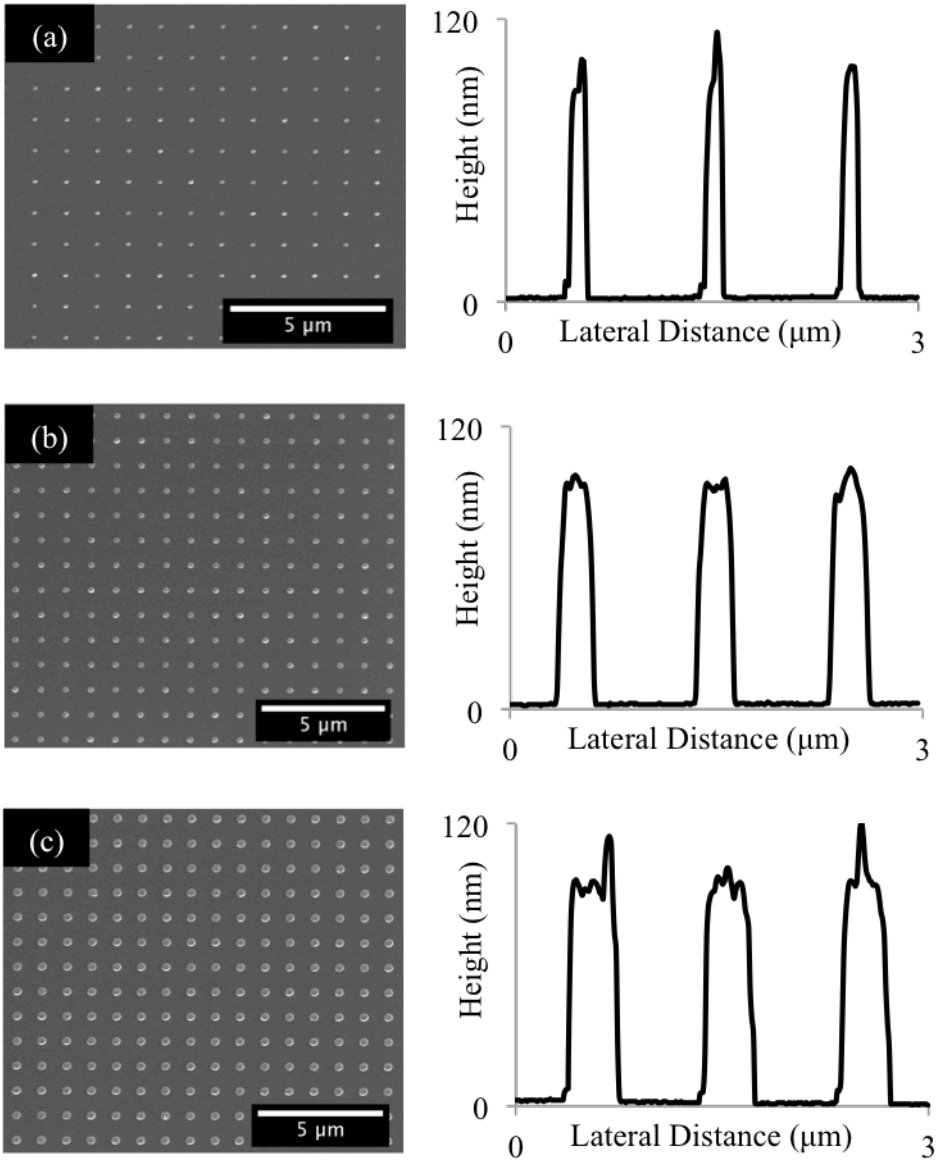

Fig. 6.1: SEM micrographs and AFM topography profiles of ANDTSs with base diameters of (a) 100, (b) 200, and (c) 300 nm.

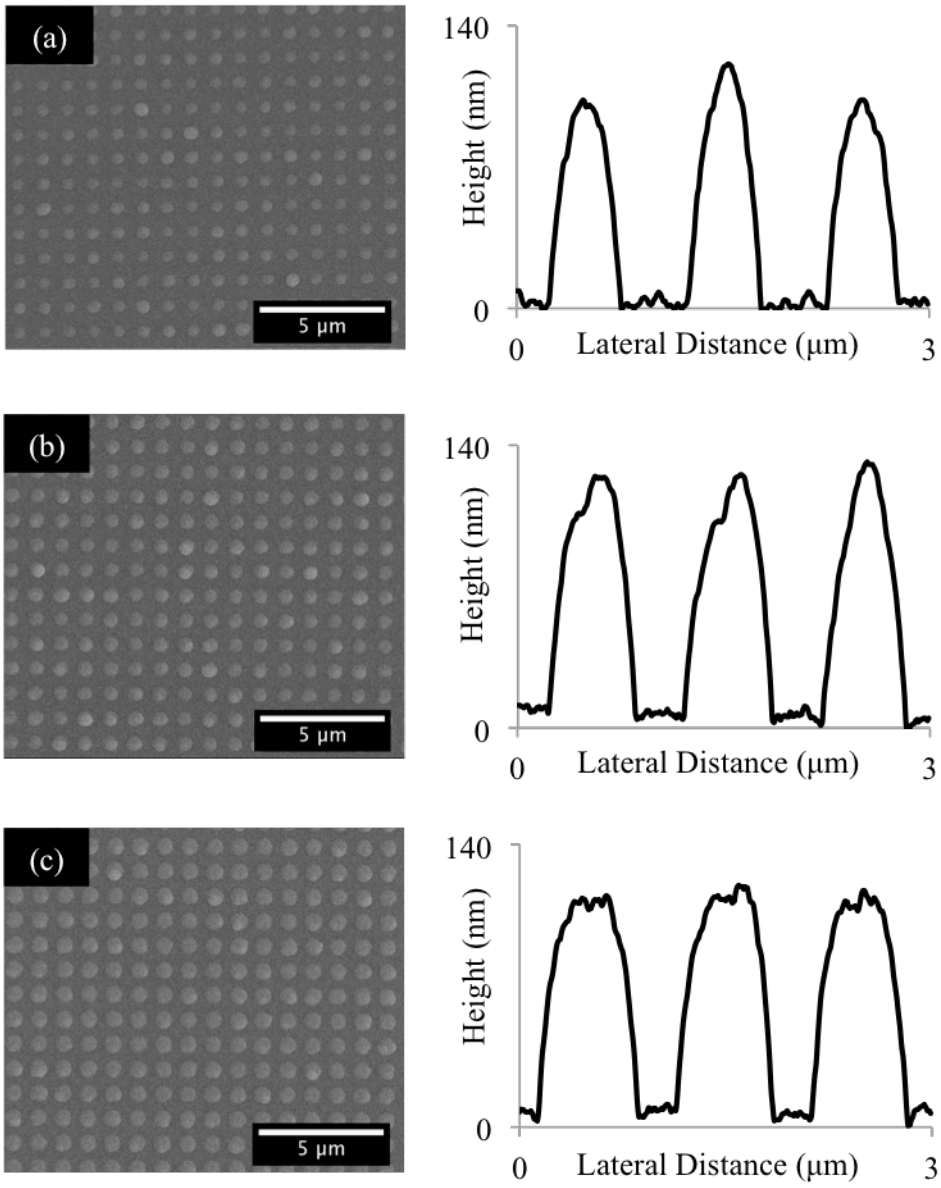

Fig. 6.2: SEM micrographs and AFM topography profiles of NSTSs composed of CSNs with core diameters of (a) 100, (b) 200, and (c) 300 nm.

6.2 Friction Measurements

The average COFs as a function of applied normal load are shown in Fig. 6.3 for an ANDTS composed of 100 nm diameter Al nanodots, a NSTS fabricated from CSNs with 100 nm diameter Al cores, and a polished (100) Si wafer, based on five scratches for each normal load. For all three surfaces, the COF varies significantly with applied normal load at low loads and then becomes relatively independent of load for higher applied normal loads. Both the ANDTS and the NSTS have reduced COFs compared to smooth Si across the entire load range. In the high normal load range, the COF of the ANDTS is notably reduced compared to smooth Si. For example, at 8000 μN normal load, the COFs of these two surfaces are 0.044 and 0.062, respectively. The NSTS performs even better, with a very low minimum COF of 0.015. This represents a 66% reduction in COF compared to the ANDTS and a 76% reduction compared to smooth Si at 8000 μN normal load.

At low loads, the heavy dependence of the COF on applied normal load indicates that adhesive effects are significantly contributing to the frictional behavior. More insight can be attained from the relationship between the measured friction force and the applied normal load, as shown in Fig. 6.4. The friction coefficient is usually defined from Amontons' law, which establishes a direct proportionality between friction force and applied normal load. This implies that, in the absence of adhesive effects, a plot of friction vs. normal load would have a constant slope equal to the friction coefficient and a y-intercept that is precisely zero. However, for all three surfaces measured, the friction vs. load relationship at normal loads up to 2000 μN is roughly linear, with a linear fit that does not pass through the origin. In this case, the magnitude of the y-intercept of these fits is a qualitative measure of the adhesive contribution to friction,

with a lower y-intercept value corresponding to lower adhesion. Based on the relative magnitudes of the y-intercepts of these trend lines, it can be concluded that adhesion plays a larger role in the frictional behavior of the (100) Si and the ANDTS compared to the NSTS. At higher loads (4000 μN and above), the data is best fit using a linear trend line with a different slope. Notably, however, these trend lines still have a non-zero y-intercept, which means that adhesion still plays a demonstrable role on the measured friction values.

The dependence of friction on the size of the individual nanotextures is also of interest. The measured friction for ANDTSs with 100, 200, and 300 nm base diameters are shown in Fig. 6.5(a). For loads up to 2000 μN, the measured friction values largely overlap, regardless of nanodot diameter. At higher loads, the friction measurements begin to diverge, with higher friction forces occurring for larger nanodot diameters. In this case, increased nanodot size correlates with increased nanodot volume fraction within the contact area with the tip during nanoscratch tests, which effectively increases the contact area and leads to higher friction. Similar measurements on NSTSs composed of CSNs with various core diameters are plotted in Fig. 6.5(b). For these surfaces, the measured friction forces are effectively identical, regardless of core diameter. Due to the larger CSN diameters caused by the a-Si shell, the relative size difference between each of the CSN sizes (400, 500, and 600 nm diameters) is not as pronounced as compared to the Al nanodots (100, 200, and 300 nm diameters). As a result, the contact area for the NSTSs does not change very much as the CSN diameter increases, resulting in similar friction for all the NSTSs, regardless of CSN core diameter.

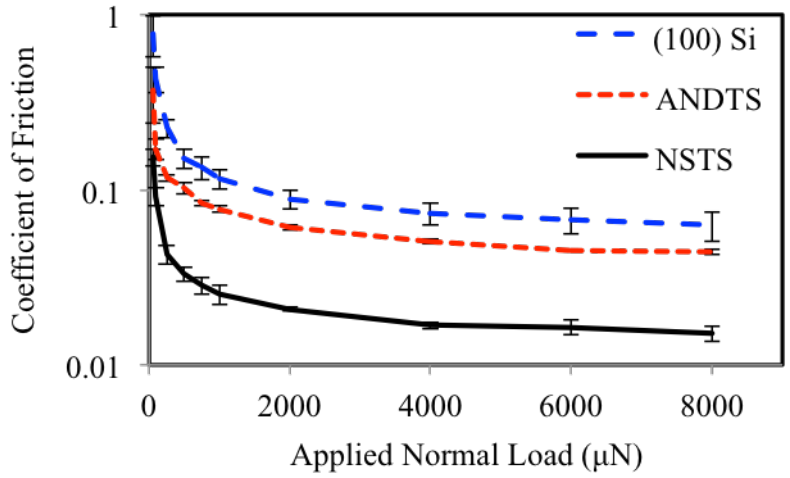

Fig. 6.3: COF measurements for a 100 nm diameter ANDTS, a NSTS fabricated from CSNs with 100 nm diameter Al cores, and a polished (100) Si wafer.

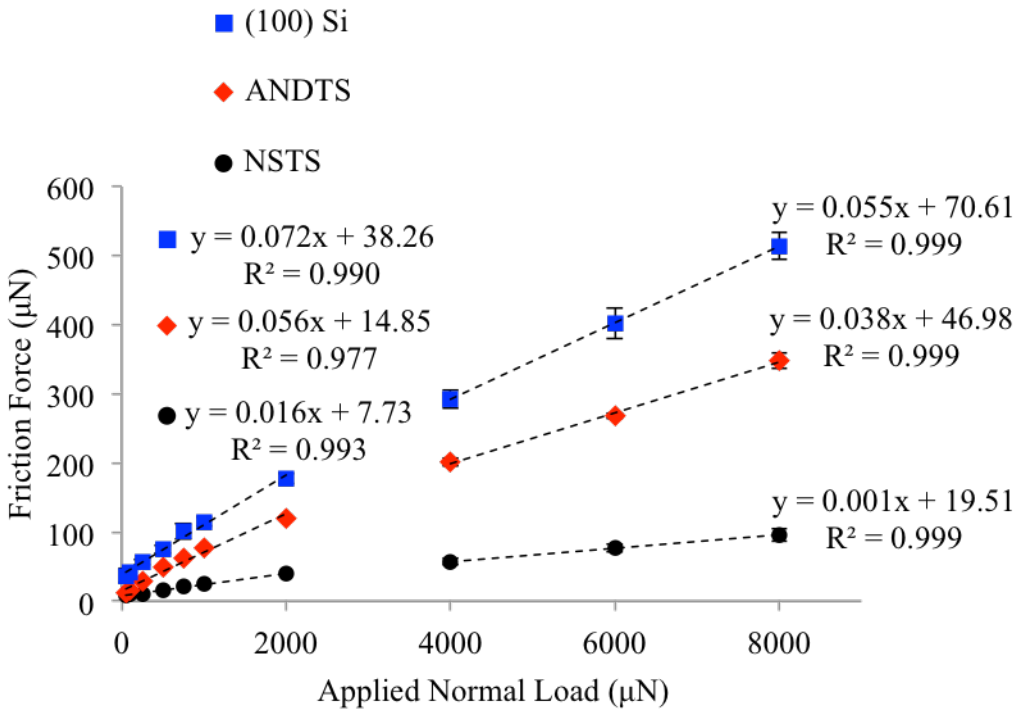

Fig. 6.4: Friction force measurements for a 100 nm diameter ANDTS, a NSTS fabricated from CSNs with 100 nm diameter Al cores, and a polished (100) Si wafer.

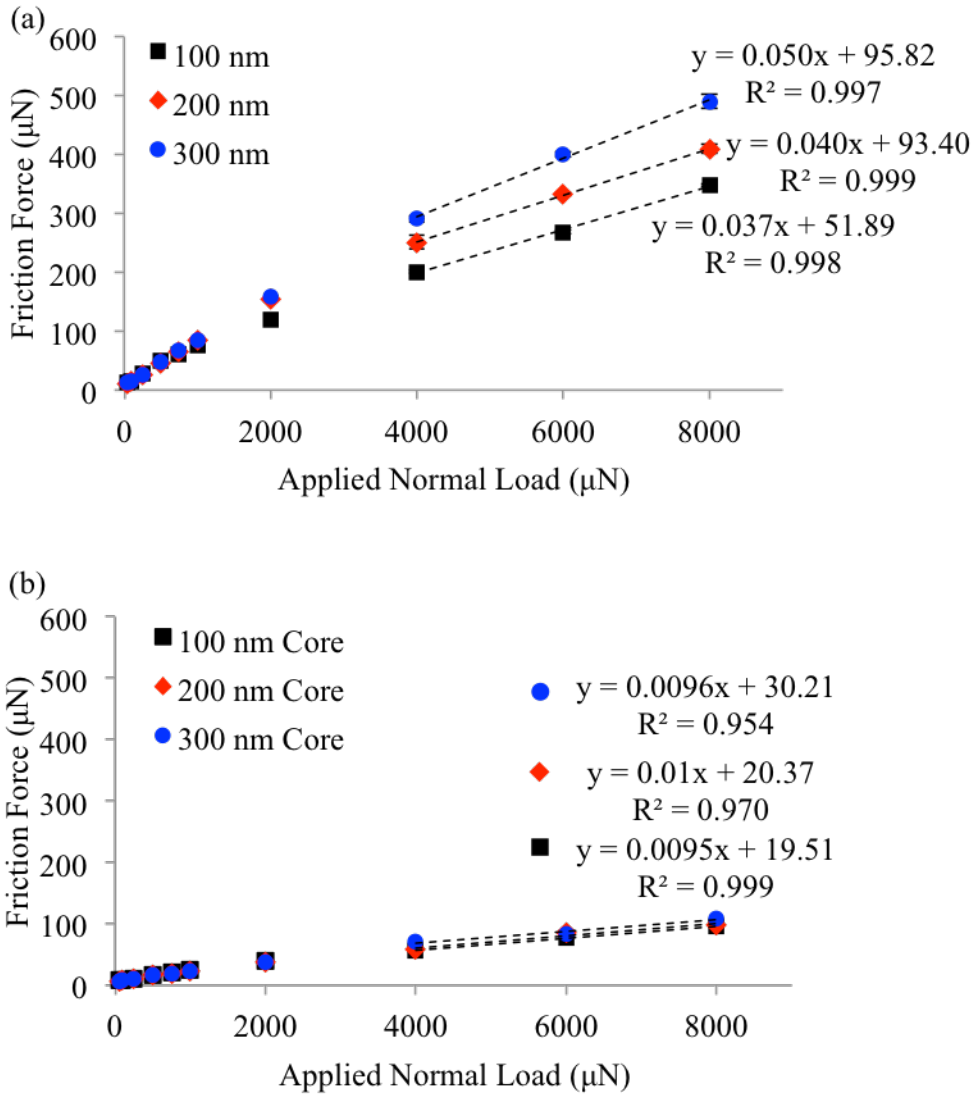

Fig. 6.5: Friction force measurements for ANDTSs with different nanodot diameters (a) and NSTSs fabricated from CSNs with different core diameters (b).

6.2.1 Friction Mechanisms

From the plot of COF vs. applied normal load in Fig. 6.3, it is apparent that COF varies heavily with applied load at low normal loads and is relatively independent of load at high loads. This strong dependence of COF on normal load, as well as the non-zero y-intercept obtained from the friction vs. normal load data in Fig. 6.4, further indicates that adhesive interactions play a significant role in the frictional behavior of these surfaces at low normal loads. Hertzian contact theory predicts that when the contact deformations are purely elastic, as might be the case at low normal loads, the contact area depends on applied normal load as [156]:

$$A \propto P^{2/3} \tag{6.1}$$

where A is the real area of contact and P is the applied normal load. Furthermore, the frictional force F is proportional to the contact area when adhesion is the dominant mechanism of friction, which has been verified to be valid even for nanotextured surfaces [20]. Therefore, when adhesion effects are significant, the COF should be proportional to the normal load raised to the -1/3 power, as shown in Eq. 6.2 below.

$$COF = \frac{F}{P} \propto \frac{A}{P} \propto P^{-1/3} \tag{6.2}$$

A plot of COF vs. applied normal load raised to the -1/3 power is shown in Fig. 6.6 for a 100 nm diameter ANDTS, a NSTS fabricated from CSNs with 100 nm diameter Al cores, and smooth Si. For all three surfaces, there are three friction regimes with different dependencies on normal load raised to the -1/3 power. For loads at or below 250 μN (denoted as 0.16 $\mu N^{-1/3}$), a strong proportionality between COF and applied load raised to the -1/3 power is observed, which suggests that significant adhesive friction occurs in this regime. At the highest loads, namely 4000 μN (0.063 $\mu N^{-1/3}$) and above, the COF depends much more weakly on applied load raised

to the -1/3 power, as indicated by the smaller slopes of the linear trend lines. For example, for the smooth Si surface, the slope decreases from 4.91 at low load to 0.82 at high load, which represents an 83% decrease. Similarly, the slopes for these two load ranges decrease by 76% and 87% for the ANDTS and the NSTS, respectively. This substantially reduced dependence on applied normal load suggests that deformation mechanisms play a larger, perhaps even dominant, role in friction at these loads. However, as previously noted in Fig. 6.4, adhesive interactions clearly still influence the frictional behavior of all 3 surfaces at high loads. At intermediate loads (500-2000 μN), the data is best fit by linear trend lines with different slopes than those obtained from both the high- and low-load ranges. This suggests that both adhesive and deformational components of friction are important in this region, with neither truly dominating.

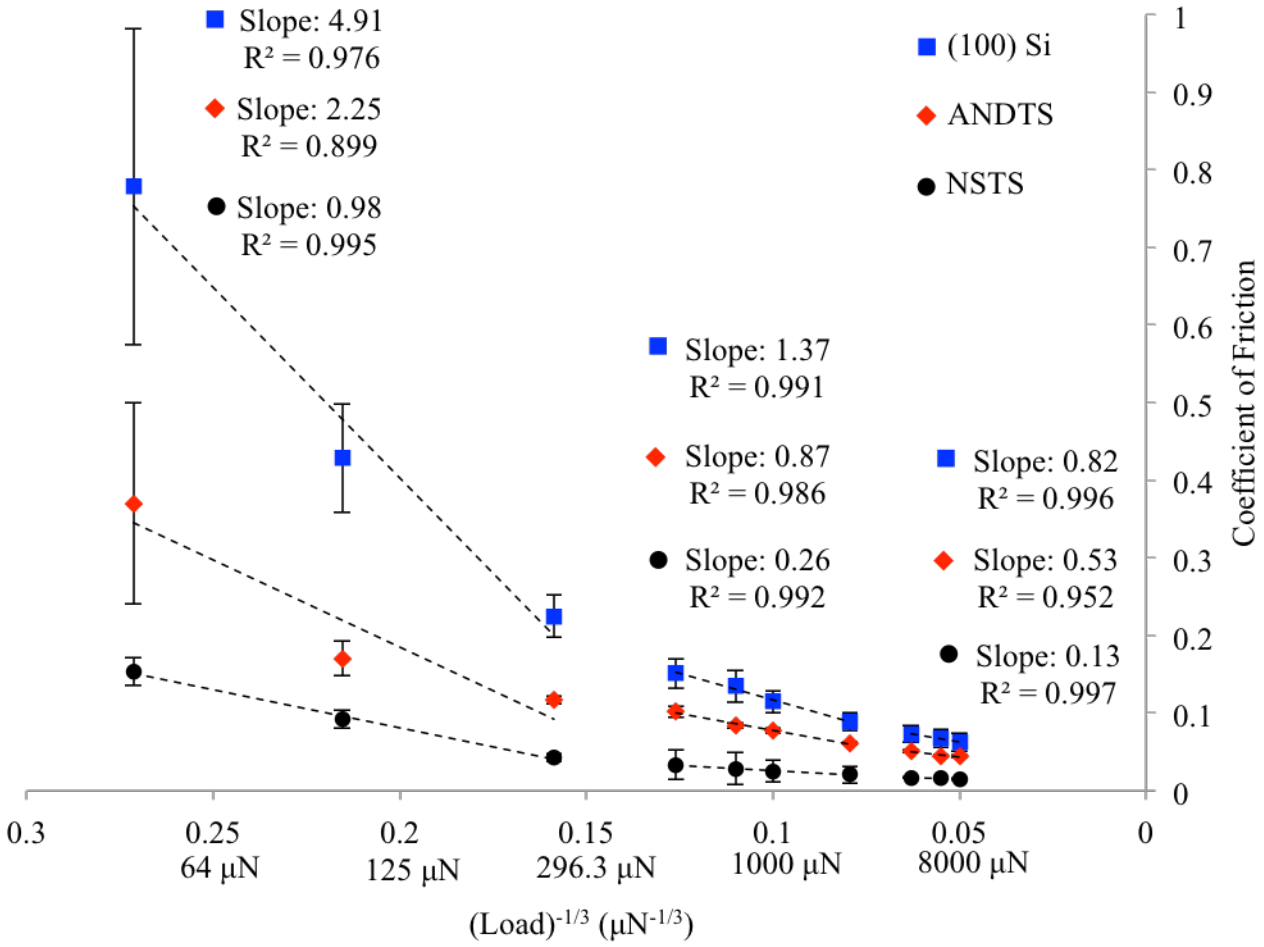

Fig. 6.6: COF vs. normal load raised to -1/3 power for a 100 nm diameter ANDTS, a NSTS fabricated from CSNs with 100 nm diameter Al cores, and a polished (100) Si wafer.

6.3 Adhesion Measurements

Pull-off adhesion forces were characterized for the ANDTSs and NSTSs. Since the adhesion force is the negative-valued force measured by the nanoindenter transducer as the diamond tip breaks contact with the sample surface, these measurements must be performed using feedback control to govern the displacement of the transducer. As a result, it is customary to plot adhesion as a function of maximum indenter displacement. The average adhesion forces measured by the diamond tip on the 100 nm diameter ANDTS and the NSTS fabricated from CSNs with 100 nm diameter Al cores are shown in Fig. 6.7(a) for indentation depths ranging from 2 to 40 nm. For indentation depths up to 20 nm, the measured adhesion forces on the ANDTSs range from 0.32 to 0.44 μN. Higher adhesion is observed for the NSTS, in some cases increasing by 100% compared to the ANDTS at the same indentation depth; however, these values are still below 1 μN. At 40 nm indentation depth, the adhesion on the ANDTS increases to 1.1 μN, which is 59% higher than the measured adhesion of 0.71 μN on the NSTS. For this larger indentation depth, more significant deformation of the soft Al nanodots occurs, leading to a substantial increase in contact area and adhesion.

Compared to reported adhesion values of 9-15 μN on smooth (100) Si across the same indentation depth range and using the same 100 μm tip [87], the measured adhesion on both the ANDTSs and the NSTSs represents a greater than 95% decrease in adhesion. Although the friction data suggests that the NSTS should be less adhesive compared to the ANDTS, lower measured adhesion forces are found for the ANDTS at small indentation depth. However, it is important to point out that the size of the individual nanostructures is different for the two surfaces. The larger size of the CSNs on the NSTSs means that the real area of contact on this

surface will be larger compared to the ANDTS for a given indentation depth. Therefore, higher adhesion is expected for the NSTS when the two surfaces are subjected to the same normal displacements. Furthermore, when the adhesion force is plotted against the average indentation load corresponding to each displacement used during adhesion testing, as shown in Fig. 6.7(b), it is clear that for loads above 10 μN, the NSTS has less adhesion than the ANDTS. Notably, the measured adhesion increases drastically with increasing contact load for the ANDTS, while the adhesion on the NSTS remains relatively constant at ~0.6-0.7 μN over a much wider load range. This is in agreement with the measured COF and friction force data (Figs. 6.3 and 6.4), which indicates that the NSTS has lower adhesive friction compared to the ANDTS.

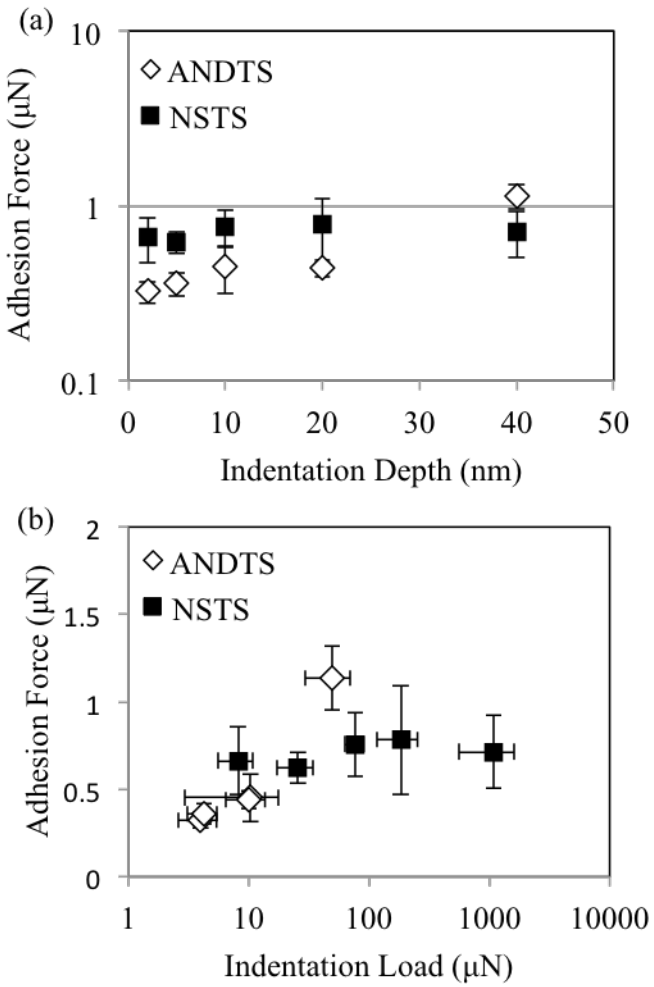

Fig. 6.7: Adhesion measurements for a 100 nm diameter ANDTS and a NSTS composed of CSNs with 100 nm diameter Al cores as a function of indentation depth (a) and as a function of indentation load (b).

6.4 Surface Deformation Characterization

After scratch testing, the surface deformation of both the ANDTSs and the NSTSs were characterized by SEM and AFM. For the ANDTSs, surface deformation was first detected for scratches at 250 μN normal load, with the severity of the scratch deformation increasing with increasing normal load. Fig. 6.8 shows SEM micrographs of surface deformations from 250 μN, 1000 μN, and 8000 μN normal load scratches, as well as representative AFM topography profiles across the middle of each scratch region. At 250 μN, while the individual nanodots appear to be only slightly deformed from the SEM image, the AFM topography profile shows that the nanodots in the center of the scratch region have been deformed to a height of ~55 nm, which is roughly half the height of an undeformed nanodot. From the COF analysis in Fig. 6.6, the data indicates that primarily adhesive friction occurs for applied normal loads up to 250 μN, which correlates with the normal load at which plastic deformation is first observed from the SEM images. However, from the AFM analysis, it is clear that the nanodots are significantly deformed at 250 μN, so although adhesive effects are clearly present, it cannot be said that this is truly the transition point from an adhesion dominated friction regime to a regime where deformation-mediated friction begins to contribute.

As the applied normal load is increased to 1000 μN, significantly more plastic deformation is observed in the contact area. At the largest scratch load of 8000 μN, the nanodots are substantially flattened, but not completely removed. The topography profile for these scratches reveals that the most severely deformed nanodots have a residual height of ~10 nm. Because the individual nanodots are neither removed nor flattened all the way to the substrate

during scratching, the COF for the ANDTS never reaches that of smooth Si because the tip never comes in contact with substrate.

For the NSTSs, no observable deformation was detected at any applied normal load. SEM micrographs of 8000 μN normal load scratches are shown in Fig. 6.9 for NSTSs composed of CSNs with 100, 200, and 300 nm diameter cores, along with representative AFM topography profiles across the middle of each scratch region. The CSNs have unique deformation-resistant properties that result in very high deformation resistance under frictional loading. This deformation resistance, combined with the superior COF of the NSTS, is potentially useful in applications with microscale contact interactions. Notably, there is no tradeoff between deformation resistance and COF with the NSTSs.

6.4.1 Estimation of Contact Pressure from Scratch Deformation Measurements

Characterization of the extent of the plastic deformation from scratches on the ANTDS allows for the contact pressure during scratch testing to be estimated. This is achieved by using the width of each scratch, as measured from SEM, to estimate the contact area as a function of applied normal load. Since the tip is spherically symmetric, the scratch width defines the contact diameter during each test. To calculate the estimated contact area, image processing software (ImageJ, NIH) was used to calculate the surface area of only the deformed Al nanodots contained within a circle (with a diameter equal to the scratch width; dashed circles in Fig. 6.8) located at the center of each scratch. As this contact area is really an estimated contact area, it does not account for any elastic deformations. However, it is perhaps still useful for comparative purposes, especially when large plastic deformations occur.

For the 100 nm diameter ANDTS, the estimated contact pressure ranges from approximately 530 MPa for 50 μN normal load scratches to slightly over 1 GPa for 8000 μN scratches, without considering frictional effects. Since no deformation was detected for scratches on the NSTSs, the same analysis cannot be applied to these surfaces. However, the normal displacement during scratch testing is substantially smaller than that of the ANDTS when subjected to the same normal load. This is illustrated in Fig. 6.10, which plots the indentation depth as a function of maximum indentation load for several displacement-controlled indents on both surfaces. It can be seen that for a given indentation load, the corresponding indentation depth is much smaller for the NSTS compared to the ANDTS. For example, when the indentation load is ~75 μN, the indentation depth for the ANDTS is 40 nm, while the indentation depth for the NSTS is much smaller at only 5 nm. As a result, the contact area should be more than proportionally smaller for the NSTSs, meaning they are subjected to even higher contact pressures than the ANDTSs during nanoscratch testing.

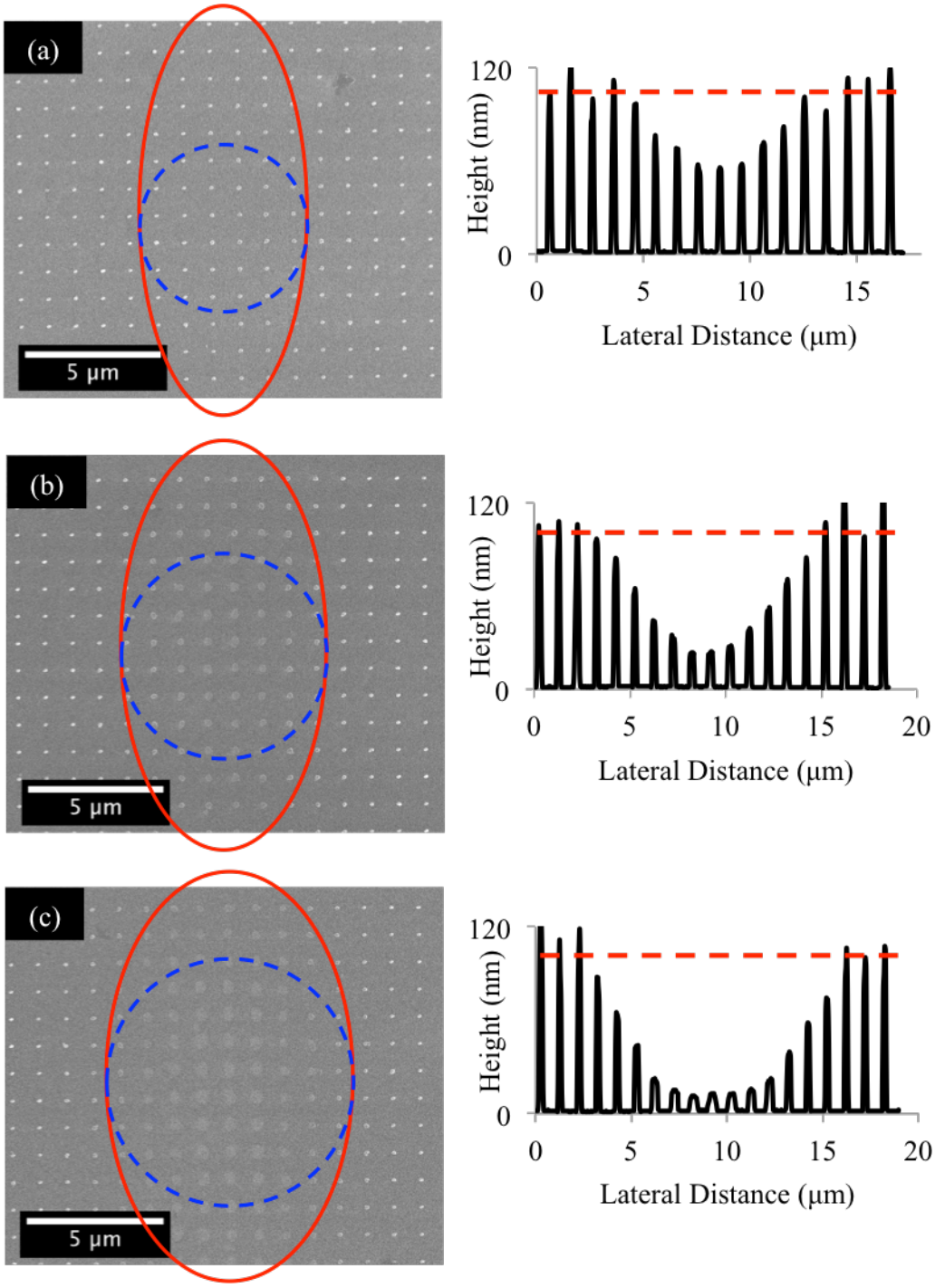

Fig. 6.8: SEM micrographs of scratches at (a) 250, (b) 1000, and (c) 8000 µN normal loads on a 100 nm diameter ANDTS. The scratch areas are indicated by the solid ovals, while the dashed circles represents the regions used to estimate contact pressure. To the right of each micrograph is an AFM topography profile of the scratch area; the nominal height of the nanodots (100 nm) is indicated by the dashed red line.

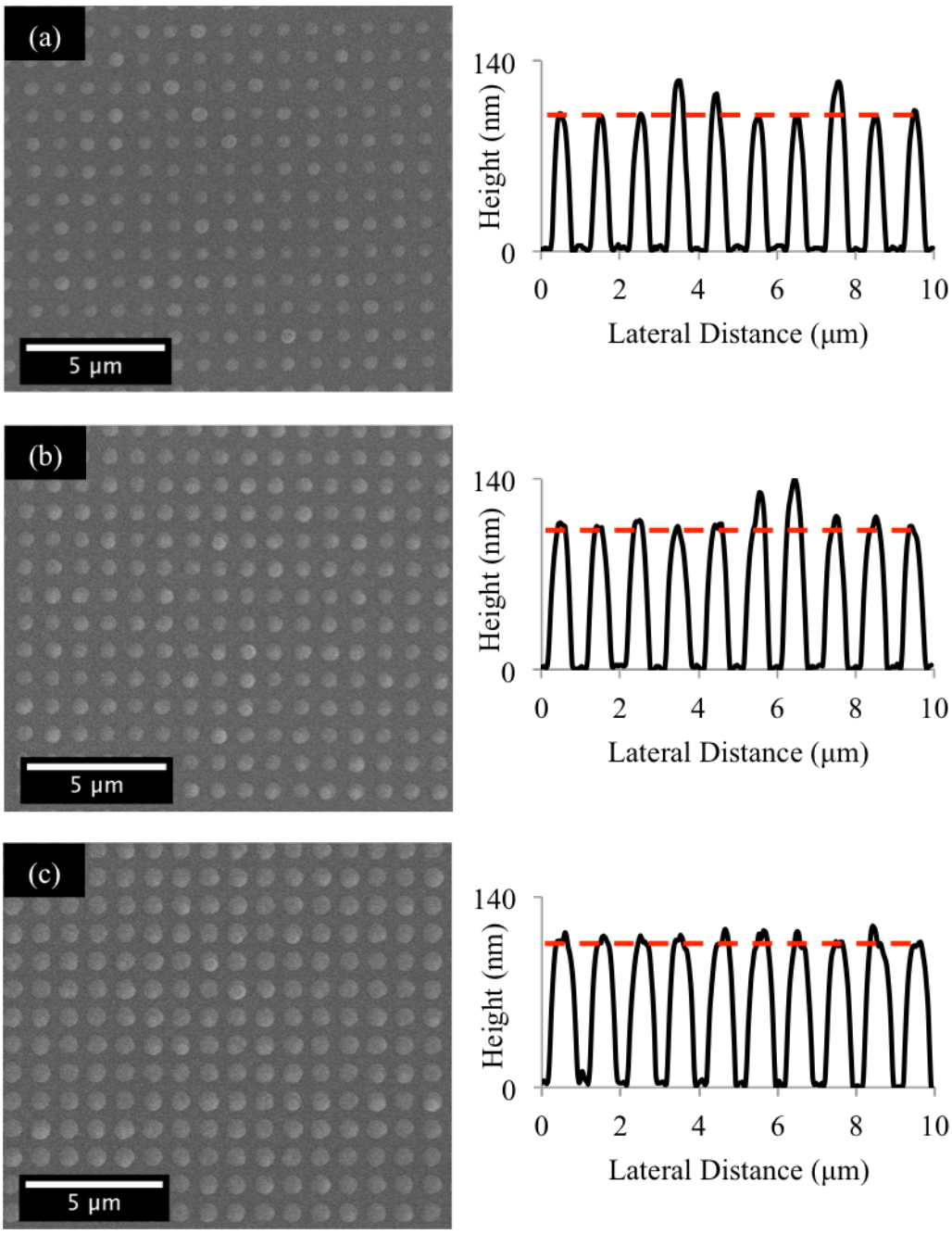

Fig. 6.9: SEM micrographs of scratches at 8000 µN normal load on NSTSs composed of CSNs with core diameters of (a) 100, (b) 200, and (c) 300 nm. To the right of each micrograph is an AFM topography profile of the scratch area; the nominal height of the CSNs (100 nm) is indicated by the dashed red line.

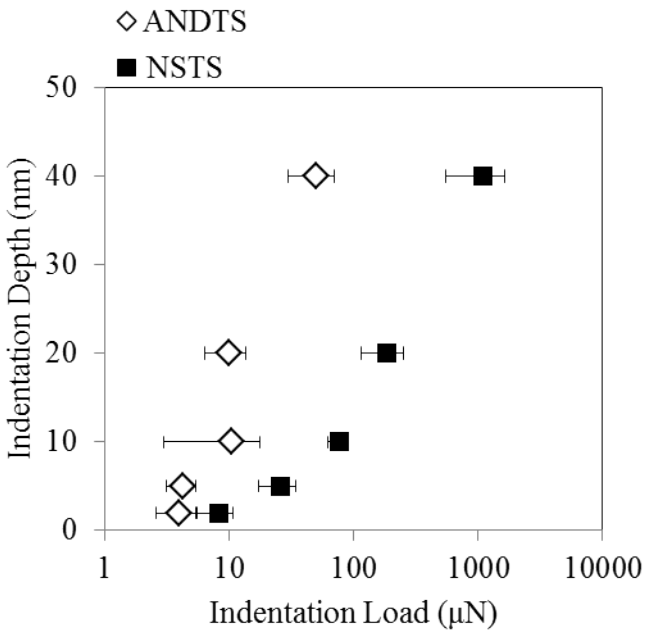

Fig. 6.10: Indentation depth as a function of maximum indentation load for a 100 nm diameter ANDTS and a NSTS composed of CSNs with 100 nm diameter Al cores.

6.5 Conclusions

Nanotextured surfaces composed of Al nanodots and NSTSs composed of Al/a-Si CSNs have been characterized to assess the frictional, adhesion, and deformation behavior of these surfaces. Compared to smooth Si, the ANDTSs and the NSTSs have reduced COFs, as low as 0.044 and 0.015, respectively. In addition, both surfaces exhibit low adhesion with pull-off forces on the order of less than 1 μN. The NSTSs are highly deformation-resistant, with no surface deformation apparent after nanoscratch testing, even at contact forces up to 8000 μN (estimated contact pressure greater than 1 GPa). In comparison, the Al nanodots are plastically deformed at contact loads as low as 250 μN. An analysis of the COF dependence on applied normal load shows that the substantial adhesive friction occurs for normal loads below 250 μN, while deformation mechanisms contribute more significantly at higher loads. Together, this combination of low COF, low adhesion, and high deformation resistance of NSTSs show promise for their use in micro- and nanotribological applications where low friction and deformation resistance are desired.

CHAPTER 7

CONCLUSIONS AND FUTURE WORK

A comprehensive investigation of the mechanical behavior of novel Al/a-Si CSNs has been performed to determine the foundational mechanisms that govern the deformation-resistant properties of Al/a-Si CSNs. Herein, the results of the investigation are summarized, conclusions are drawn from these results, and recommendations for future research efforts are proposed.

7.1 Summary of Results

In Chapter 4, the origin of the unique mechanical properties of Al/a-Si CSNs was explored through nanoindentation experiments and MD modeling. The results show that dislocation mechanisms in the Al core play a substantial role in the mechanical behavior of the CSNs, which is enabled by geometrical confinement of the soft Al core by the hard a-Si shell. In particular, the deformation behavior of these structures is critically dependent on the size of the confined core volume. As the core diameter increases, the mechanical response is significantly altered and the deformation resistance is reduced. Based on the indentation signatures exhibited by the CSNs with the smallest core diameter, the deformation behavior is mediated by dislocation activities within the confined core, with the deformation recovery resulting from dislocations retracing their paths or otherwise annihilating due to a back-stress generated during unloading. As the size of the confined core volume increases, the magnitude of this back-stress decreases, and deformation resistance is eventually completely suppressed as a result. Complimentary MD simulations show that smaller core diameters correlate with both a larger back-stress being developed and improved dislocation removal during unloading.

In Chapter 5, the role of geometric dimensionality on the mechanical behavior of Al/a-Si CSNs was assessed through experiments on hemispherical CSNs, horizontally-aligned CSRs of various lengths, and a layered thin film. Whereas the hemispherical CSNs are deformation-resistant, with nearly complete deformation recovery after indentation (even when loaded much beyond the elastic limit), the slight asymmetry in the core confinement of short CSRs results in a substantial decrease in the deformation resistance. More conventional indentation behavior is observed in the long CSRs and layered thin film. Supporting molecular dynamics simulations show that dislocations nucleated in the core of CSNs are more readily removed during unloading compared to CSRs, which indicates that the 3-dimensional core confinement of the CSNs plays an important role in the deformation-resistant properties of CSNs.

Finally, in Chapter 6, the friction, adhesion, and deformation of NSTSs composed of Al/a-Si CSNs were characterized. The results show that the NSTSs have extremely low COFs (~0.015 at 8000 μN normal load), as well as no detectable nanostructure deformation at contact loads up to 8000 μN (estimated contact pressure greater than 1 GPa). Analysis of the COF dependence on applied normal load shows that adhesive interactions contribute significantly to friction for normal loads below 250 μN, while deformation mechanisms contribute more significantly at higher loads. NSTSs not only provide low adhesion and friction at low normal loads due to reduced contact area, but also provide low COF at high normal loads due to high deformation resistance. Together, this combination of low adhesion, low COF, and high deformation resistance of NSTSs shows promise for their use in micro- and nanotribological applications where low adhesion, low friction and deformation resistance are desired.

7.2 Conclusions

The specific objectives of this investigation, as outlined in section 1.2, have been addressed through the experiments and simulations performed as a part of this study. The conclusions drawn based on these results are summarized below:

1. Confinement of the Al core, and particularly the size of the confined core volume, is critically important for the deformation-resistant properties of Al/a-Si CSNs. For CSNs with a core diameter of 100 nm, discontinuous indentation signatures are observed during nanoindentation in conjunction with nearly complete recovery of deformation beyond the elastic limit. These signatures are attributed to dislocation activities within the confined core, with the deformation recovery mediated by dislocations retracing their paths or otherwise annihilating during unloading. As the size of the confined core volume increases, the dislocation signatures are suppressed, with an attendant loss of deformation resistance.
2. The "dimensionality" of core confinement substantially influences the deformation behavior of Al/a-Si CSNs. Whereas the hemispherical CSNs have deformation-resistant properties, when the axisymmetric core confinement is broken, as in the case of CSRs with short core lengths, the deformation resistance that is observed in the CSNs is substantially reduced. In the limit of very long CSRs and layered thin films, conventional indentation behavior is observed, regardless of geometry.
3. During MD simulations of hemispherical CSNs, a high proportionality of glissile Shockley partial dislocations are nucleated in the Al core during compression, which then leads to significant egression of dislocations when the stress generated within the core is relieved during unloading. Furthermore, smaller core diameters correlate with both a

larger back-stress being developed and improved dislocation removal during unloading. MD simulations on CSRs show that dislocations nucleated in the core of CSRs are not as effectively removed during unloading compared to CSNs, which indicates that the 3-dimensional core confinement of the CSNs plays an important role in the deformation-resistant properties of CSNs.

4. NSTSs composed of hemispherical CSNs exhibit improved tribological properties compared to ANDTSs and single crystal Si. NSTSs have a COF as low as 0.015, exhibit low adhesion with adhesion forces on the order of less than 1 μN, and are highly deformation-resistant, with no surface deformation apparent after nanoscratch testing, even at contact forces up to 8000 μN (estimated contact pressure greater than 1 GPa).

These findings clarify the mechanisms that contribute to the desirable properties of Al/a-Si CSNs so that they can be designed to be effectively used in applications where the mechanical integrity of nanostructures is important.

7.3 Recommendations for Future Work

The results of this investigation provide significant insights into the origins of the novel mechanical behavior of Al/a-Si CSNs. Based on these results, further research paths into both the fundamental material physics of CSNs and the practical applications of CSNs are opened.

7.3.1 CSNs Fabricated from Other Core and Shell Materials

Whereas the mechanical behavior of Al/a-Si CSNs is attributed to dislocation dynamics within the Al core as it is compressed between the hard a-Si shell and hard Si substrate, further investigation is needed to determine if this behavior is specific to the combination of Al and a-Si,

or is rather a more general core/shell phenomenon. This can be addressed through experiments and simulations of CSNs with other core and shell materials, which can evaluate the effects of a wide variety of material properties and CSN characteristics, such as stacking fault energy, crystal structure, core/shell interface, etc., in a fundamental way. Since dislocations, particularly Shockley partials, play such a key role in Al/a-Si CSNs, the behavior of CSNs with other metallic cores is of interest. For example, using a Au core, which has a lower stacking fault energy compared to Al, or a Ni core, which will support different types of dislocations than FCC Al, may give rise to different material behaviors. Also of interest are polymer cores. Although polymers do not support dislocations in general, it may be interesting to assess whether deformation recovery can exist in CSNs with polymer cores through some other mechanism, such as viscoelasticity or shear banding.

7.3.2 *In situ* TEM Nanoindentation Experiments

In situ TEM nanoindentation is one of the most advanced techniques for assessing mechanical behavior of nanomaterials in response to applied stress and strain. Such experiments could, in principle, directly observe the dislocation activities within the cores of CSNs during compression. Presently, however, the CSN fabrication method utilized in this investigation cannot produce CSNs that are suitable for *in situ* TEM nanoindentation. Specifically, the CSN dimensions are somewhat too large to be electron transparent, and the planar processing techniques used to fabricate the CSNs are not compatible with the Si microwedge substrates that are widely utilized in *in situ* TEM nanocompression experiments. This limitation can be overcome through the development of a solution-synthesis CSN fabrication method [157,158]. Such a method will allow for the synthesis of isolated core-shell nanoparticles with extensive

control of the core and shell dimensions, with an aim to produce CSNs that are small enough for *in situ* TEM experiments and can be reliably deposited on Si microwedge substrates. Although these isolated nanostructures will potentially display different mechanical behavior compared to the CSNs detailed in this study since they are not rigidly attached to a substrate, these experiments will still provide a unique opportunity to directly observe the dynamics of confined dislocations.

7.3.3 Large-scale MD and Multiscale Simulations

The MD simulations performed in this investigation provide a substantial improvement in the understanding of the mechanisms that contribute to the novel mechanical behavior of Al/a-Si CSNs. However, several aspects of the real-world CSNs were not considered in the models. Notably, the models used a single crystal Al core, while the as-fabricated CSNs have a polycrystalline core structure. In addition, the as-fabricated Al cores are not expected to be pristine and should have a non-zero initial dislocation density, potentially including misfit dislocations at the core/substrate interface due to the lattice mismatch between Al and Si. There is also an interest in how the amorphous/crystalline interphase region at the core/shell interface affects the underlying dislocation dynamics in the CSNs. More sophisticated and larger scale MD simulations investigating the effects of realistic polycrystalline Al cores on Si substrates, non-zero initial dislocation densities, and the core/shell interphase structure can provide further insight into the properties of CSNs. Furthermore, due to the inherent size and timescale limitations of MD, the mechanical behavior of CSNs can also be studied using multiscale methods such as the coupled atomistics and discrete dislocation (CADD) method [159,160], which will allow access to more experimentally relevant length and time scales.

7.3.4 Long-term Durability

In terms of utilizing NSTSs in practical applications, the long-term durability of these surfaces still needs to be assessed. This is especially important for MEMS/NEMS applications, in which reliability is characterized by the ability to withstand millions of actuation cycles. In this investigation, individual CSNs were subjected to a maximum of 4 loading/unloading cycles, while the friction and deformation of NSTSs were assessed after only a single nanoscratch. Obviously, this is not enough to make definitive claims about the resilience of the CSNs and NSTSs over time. The durability of CSNs can be evaluated using nanoscale dynamic mechanical analysis (DMA) [161], a nanoindentation technique in which a sinusoidal load oscillation is applied to a CSN with a specified loading frequency. Using a loading frequency of 60 Hz, for example, DMA can apply over 100,000 loading/unloading cycles to a single CSN over a span of 30 minutes. Likewise, traditional micro- and nanotribometry experiments can be used to measure the friction and durability of NSTSs in response to reciprocating abrasion with precise load control. These experiments, however, require relatively large-scale patterned areas, typically on the order of at least square centimeters. The serial throughput of EBL makes fabricating such large areas of CSNs potentially untenable, so further research into more efficient NSTS fabrication methods is also needed.

REFERENCES

[1] K.E. Aifantis, A.A. Konstantinidis, Hall-Petch revisited at the nanoscale, Mater. Sci. Eng. B. 163 (2009) 139-144. doi:10.1016/j.mseb.2009.05.010.

[2] R.W. Armstrong, 60 years of Hall-Petch: Past to present nano-scale connections, Mater. Trans. 55 (2014) 2-12. doi:10.2320/matertrans.MA201302.

[3] A. Misra, R.G. Hoagland, Plastic flow stability of metallic nanolaminate composites, J. Mater. Sci. 42 (2007) 1765-1771. doi:10.1007/s10853-006-0895-9.

[4] N. Chawla, D.R.P. Singh, Y.-. Shen, G. Tang, K.K. Chawla, Indentation mechanics and fracture behavior of metal/ceramic nanolaminate composites, J. Mater. Sci. 43 (2008) 4383-4390. doi:10.1007/s10853-008-2450-3.

[5] I.N. Mastorakos, A. Bellou, D.F. Bahr, H.M. Zbib, Size-dependent strength in nanolaminate metallic systems, J. Mater. Res. 26 (2011) 1179-1187. doi:10.1557/jmr.2011.120.

[6] E.T. Lilleodden, J.A. Zimmerman, S.M. Foiles, W.D. Nix, An experimental and computational study of the elastic-plastic transition in thin films, MRS Proc. 673 (2001) 1-3.

[7] S.M. Han, T. Bozorg-Grayeli, J.R. Groves, W.D. Nix, Size effects on strength and plasticity of vanadium nanopillars, Scr. Mater. 63 (2010) 1153-1156. doi:10.1016/j.scriptamat.2010.08.011.

[8] H. Hirakata, O. Nishijima, N. Fukuhara, T. Kondo, A. Yonezu, K. Minoshima, Size effect on fracture toughness of freestanding copper nano-films, Mater. Sci. Eng. A. 528 (2011) 8120-8127. doi:10.1016/j.msea.2011.07.071.

[9] A. Rinaldi, P. Peralta, K. Sieradzki, E. Traversa, S. Liccoccia, Role of dislocation density on the sample-size effect in nanoscale plastic yielding, J. Nanomech. Micromech. 2 (2012) S1-S6. doi:10.1061/(ASCE)NM.2153-5477.0000047.

[10] W. Wang, Y. Zhong, K. Lu, L. Lu, D.L. McDowell, T. Zhu, Size effects and strength fluctuation in nanoscale plasticity, Acta Mater. 60 (2012) 3302-3309. doi:10.1016/j.actamat.2012.03.016.

[11] O.V. Kuzmin, Y.T. Pei, J.T.M. De Hosson, Size effects and ductility of Al-based metallic glass, Scr. Mater. 67 (2012) 344-347. doi:10.1016/j.scriptamat.2012.05.019.

[12] S. Chang, A.K. Nair, M.J. Buehler, Nanoindentation study of size effects in nickel-graphene nanocomposites, Philos. Mag. Lett. 93 (2013) 196-203. doi:10.1080/09500839.2012.759293.

[13] F. Hammami, Y. Kulkarni, Size effects in twinned nanopillars, J. Appl. Phys. 116 (2014). doi:10.1063/1.4890541.

[14] W.D. Nix, J.R. Greer, G. Feng, E.T. Lilleodden, Deformation at the nanometer and micrometer length scales: Effects of strain gradients and dislocation starvation, Thin Solid Films. 515 (2007) 3152-3157. doi:10.1016/j.tsf.2006.01.030.

[15] Z.W. Shan, R.K. Mishra, S.A. Syed Asif, O.L. Warren, A.M. Minor, Mechanical annealing and source-limited deformation in submicrometre-diameter Ni Crystals, Nat. Mater. 7 (2008) 115-119. doi:10.1038/nmat2085.

[16] E.-. Yoon, R.A. Singh, H. Kong, B. Kim, D.-. Kim, H.E. Jeong, K.Y. Suh, Tribological properties of bio-mimetic nano-patterned polymeric surfaces on silicon wafer, Tribol. Lett. 21 (2006) 31-37. doi:10.1007/s11249-005-9005-4.

[17] N.S. Tambe, B. Bhushan, Micro/nanotribological characterization of PDMS and PMMA used for BioMEMS/NEMS applications, Ultramicroscopy. 105 (2005) 238-247. doi:10.1016/j.ultramic.2005.06.050.

[18] B.D. Morton, H. Wang, R.A. Fleming, M. Zou, Nanoscale Surface Engineering with Deformation-resistant Core-shell Nanostructures, Tribol. Lett. 42 (2011) 51-8. doi:10.1007/s11249-011-9747-0.

[19] M. Zou, H. Wang, P.R. Larson, K.L. Hobbs, M.B. Johnson, O.K. Awitor, Ni nanodot-patterned surfaces for adhesion and friction reduction, Tribol. Lett. 24 (2006) 137-142.

[20] H. Wang, R.P. Nair, M. Zou, P.R. Larson, A.L. Pollack, K. Hobbs, M.B. Johnson, O. Awitor, Friction study of a Ni nanodot-patterned surface, Tribol. Lett. 28 (2007) 183-189.

[21] J.M. Lackner, W. Waldhauser, L. Major, C. Teichert, P. Hartmann, Tribology of bio-inspired nanowrinkled films on ultrasoft substrates, Comput. Struct. Biotechnol. J. 6 (2013) 1-12.

[22] W. Tidwell, D. Scott, H. Wang, R. Fleming, M. Zou, Nanoindentation study of deformation-resistant Al/a-Si core-shell nanostructures, Acta Mater. 59 (2011) 6110-16. doi:10.1016/j.actamat.2011.06.023.

[23] L. Qian, W. Shen, B. Shen, G.W. Qin, B. Das, Nanoporous gold-alumina core-shell films with tunable optical properties, Nanotechnology. 21 (2010). doi:10.1088/0957-4484/21/30/305705.

[24] L. Zhang, D.A. Blom, H. Wang, Au-Cu_2O core-shell nanoparticles: A hybrid metal-semiconductor heteronanostructure with geometrically tunable optical properties, Chem. Mater. 23 (2011) 4587-4598. doi:10.1021/cm202078t.

[25] G. Armelles, A. Cebollada, A. Garcia-Martin, J. Montero-Moreno, M. Waleczek, K. Nielsch, Magneto-optical properties of core-shell magneto-plasmonic Au-$Co_xFe_{3-x}O_4$ nanowires, Langmuir. 28 (2012) 9127-9130. doi:10.1021/la300431a.

[26] S. Mathew, B.S. Bhardwaj, A.D. Saran, P. Radhakrishnan, V.P.N. Nampoori, C.P.G. Vallabhan, J.R. Bellare, Effect of ZnS shell on optical properties of CdSe-ZnS core-shell quantum dots, Opt. Mater. 39 (2015) 46-51. doi:10.1016/j.optmat.2014.10.061.

[27] Y. Lei, W. Chim, Highly ordered arrays of metal/semiconductor core-shell nanoparticles with tunable nanostructures and photoluminescence, J. Am. Chem. Soc. 127 (2005) 1487-1492. doi:10.1021/ja043969m.

[28] M. Tadic, M. Panjan, D. Markovic, NiO/SiO_2 nanostructure and the magnetic moment of NiO nanoparticles, Mater. Lett. 64 (2010) 2129-2131. doi:10.1016/j.matlet.2010.07.006.

[29] V. Singh, M.S. Seehra, S. Bali, E.M. Eyring, N. Shah, F.E. Huggins, G.P. Huffman, Magnetic properties of (Fe, FeB)/-Fe_2O_3 core shell nanostructure, J. Phys. Chem. Solids. 72 (2011) 1373-1376. doi:10.1016/j.jpcs.2011.08.009.

[30] Y. Zhao, J. Miao, X.H. Wu, L.J. Qiao, X.G. Xu, Y. Jiang, Enhanced magnetic and dielectric properties of $BiFeO_3$/$BaTiO_3$ core-shell nanostructure, Micro. Nano. Lett. 7 (2012) 910-913. doi:10.1049/mnl.2012.0409.

[31] Y. Lu, S. Proch, M. Schrinner, M. Drechsler, R. Kempe, M. Ballauff, Thermosensitive core-shell microgel as a "nanoreactor" for catalytic active metal nanoparticles, J. Mater. Chem. 19 (2009) 3955-3961. doi:10.1039/b822673n.

[32] D.M. Fouad, M.B. Mohamed, Studies on the photo-catalytic activity of semiconductor nanostructures and their gold core-shell on the photodegradation of malathion, Nanotechnology. 22 (2011). doi:10.1088/0957-4484/22/45/455705.

[33] K.K. Haldar, S. Kundu, A. Patra, Core-size-dependent catalytic properties of bimetallic Au/Ag core-shell nanoparticles, ACS Appl. Mater. Interfaces. 6 (2014) 21946-21953. doi:10.1021/am507391d.

[34] A.P. Alivisatos, Semiconductor clusters, nanocrystals, and quantum dots, Science. 271 (1996) 933-937.

[35] A.V. Jovanovic, J.A. Flint, M. Varshney, T.E. Morey, D.M. Dennis, R.S. Duran, Surface modification of silica core-shell nanocapsules: Biomedical implications, Biomacromolecules. 7 (2006) 945-949. doi:10.1021/bm050820+.

[36] Y. Qiang, J. Antony, M.G. Marino, S. Pendyala, Synthesis of core-shell nanoclusters with high magnetic moment for biomedical applications, IEEE Trans. Magn. 40 (2004) 3538-3540. doi:10.1109/TMAG.2004.828962.

[37] N.Z. Knezevic, E. Ruiz-Hernandez, W.E. Hennink, M. Vallet-Regi, Magnetic mesoporous silica-based core/shell nanoparticles for biomedical applications, RSC Adv. 3 (2013) 9584-9593. doi:10.1039/c3ra23127e.

[38] B. Mandal, H. Bhattacharjee, N. Mittal, H. Sah, P. Balabathula, L.A. Thoma, G.C. Wood, Core-shell-type lipid-polymer hybrid nanoparticles as a drug delivery platform, Nanomedicine. 9 (2013) 474-491. doi:10.1016/j.nano.2012.11.010.

[39] G. Zamora, F. Wang, C. Sun, A. Trinidad, Y.J. Kwon, S.K. Cho, K. Berg, S.J. Madsen, H. Hirschberg, Photochemical internalization-mediated nonviral gene transfection: Polyamine core-shell nanoparticles as gene carrier, J. Biomed. Opt. 19 (2014). doi:10.1117/1.JBO.19.10.105009.

[40] C.S. Bell, S.S. Yu, T.D. Giorgio, The multistrata nanoparticle: An FeO_x/Au core/shell enveloped in a silica-Au shell, Small. 7 (2011) 1158-1162. doi:10.1002/smll.201002100.

[41] J. Park, C. Dvoracek, K.H. Lee, J.F. Galloway, H.C. Bhang, M.G. Pomper, P.C. Searson, CuInSe/ZnS core/shell NIR quantum dots for biomedical imaging, Small. 7 (2011) 3148-3152. doi:10.1002/smll.201101558.

[42] L.L. Mishnaevsky Jr., D. Gross, Deformation and failure in thin films/substrate systems: Methods of theoretical analysis, Appl. Mech. Rev. 58 (2005) 338-353. doi:10.1115/1.1995717.

[43] A. Rinaldi, P. Peralta, C. Friesen, D. Nahar, S. Licoccia, E. Traversa, K. Sieradzki, Superhard nanobuttons: Constraining crystal plasticity and dealing with extrinsic effects at the nanoscale, Small. 6 (2010) 528-536. doi:10.1002/smll.200902138.

[44] A.T. Jennings, J.R. Greer, Heterogeneous dislocation nucleation from surfaces and interfaces as governing plasticity mechanism in nanoscale metals, J. Mater. Res. 26 (2011) 2803-2814. doi:10.1557/jmr.2011.338.

[45] J.V. Barth, G. Costantini, K. Kern, Engineering atomic and molecular nanostructures at surfaces, Nature. 437 (2005) 671-9.

[46] B. Bhushan, H. Liu, Micro/nanoscale tribological and mechanical characterization for MEMS/NEMS, SPIE Proc. 5343 (2004) 194-206. doi:10.1117/12.531849.

[47] J. Keller, D. Vogel, B. Michel, Nanoscale deformation measurements for reliability assessment of MEMS and NEMS, Proc. NSTI Nanotech. Conf. 4 (2007) 57-60.

[48] A.J. Lockwood, M.S. Bobji, R.J.T. Bunyan, T.J. Inkson, Cyclic deformation and nano-contact adhesion of MEMS nano-bridges by in-situ TEM nanomechanical testing, J. Phys. Conf. Ser. 241 (2010). doi:10.1088/1742-6596/241/1/012056.

[49] H.F. Dadgour, M.M. Hussain, A. Cassell, N. Singh, K. Banerjee, Impact of scaling on the performance and reliability degradation of metal-contacts in NEMS devices, Proc. IEEE IRPS. (2011) 3D.3.1-3D.3.10. doi:10.1109/IRPS.2011.5784489.

[50] C.M. Mate, J. Wu, Nanotribology of polymer surfaces for disk drive applications, ACS Sympos. Ser. 39 (1998) 1141-1142.

[51] N. Tagawa, M. Takada, A. Mori, H. Sawada, K. Kawahara, Development of contact sliders with nanotextures by femtosecond laser processing, Tribol. Lett. 24 (2006) 143-149. doi:10.1007/s11249-006-9142-4.

[52] H. Wang, J. Kim, M. Zou, S. Tung, J. Kim, Adhesion study of Escherichia coli cells on nano-/microtextured surfaces in a microfluidic system, IEEE Trans. Nano. 7 (2008) 573-579.

[53] H. Conrad, J. Narayan, On the grain size softening in nanocrystalline materials, Scr. Mater. 42 (2000) 1025-1030.

[54] H. Van Swygenhoven, P. Derlet, A. Hasnaoui, Atomic mechanism for dislocation emission from nanosized grain boundaries, Phys. Rev. B. 66 (2002) 024101.

[55] Z.S. Ma, Y.C. Zhou, S.G. Long, C. Lu, Residual stress effect on hardness and yield strength of Ni thin film, Surf. Coat. Technol. 207 (2012) 305-309. doi:10.1016/j.surfcoat.2012.07.002.

[56] E. Arzt, Size effects in materials due to microstructural and dimensional constraints: A comparative review, Acta Materialia. 46 (1998) 5611-5626. doi:10.1016/S1359-6454(98)00231-6.

[57] S. Shao, S.N. Medyanik, Interaction of dislocations with interfaces in nanoscale multilayered metallic composites, Proc. ASME IMECE. 13 (2009) 1217-1222. doi:10.1115/IMECE2008-67523.

[58] C. Brandl, T.C. Germann, A. Misra, Structure and shear deformation of metallic crystalline-amorphous interfaces, Acta Mater. 61 (2013) 3600-3611. doi:10.1016/j.actamat.2013.02.047.

[59] G. Richter, K. Hillerich, D.S. Gianola, R. Monig, O. Kraft, C.A. Volkert, Ultrahigh strength single crystalline nanowhiskers grown by physical vapor deposition, Nano Lett. 9 (2009) 3048-3052. doi:10.1021/nl9015107.

[60] A.T. Jennings, M.J. Burek, J.R. Greer, Microstructure versus Size: Mechanical properties of electroplated single crystalline Cu nanopillars, Phys. Rev. Lett. 104 (2010). doi:10.1103/PhysRevLett.104.135503.

[61] D. Mordehai, M. Kazakevich, D.J. Srolovitz, E. Rabkin, Nanoindentation size effect in single-crystal nanoparticles and thin films: A comparative experimental and simulation study, Acta Mater. 59 (2011) 2309-2321. doi:10.1016/j.actamat.2010.12.027.

[62] O.L. Warren, Z. Shan, S.A.S. Asif, E.A. Stach, J.W. Morris Jr., A.M. Minor, In situ nanoindentation in the TEM, Mater. Today. 10 (2007) 59-60. doi:10.1016/S1369-7021(07)70051-2.

[63] A.M. Minor, S.A. Syed Asif, Z. Shan, E.A. Stach, E. Cyrankowski, T.J. Wyrobek, O.L. Warren, A new view of the onset of plasticity during the nanoindentation of aluminium, Nat. Mater. 5 (2006) 697-702. doi:10.1038/nmat1714.

[64] J. Deneen, W.M. Mook, A. Minor, W.W. Gerberich, C.B. Carter, In situ deformation of silicon nanospheres, J. Mater. Sci. 41 (2006) 4477-4483. doi:10.1007/s10853-006-0085-9.

[65] J. Deneen Nowak, W.M. Mook, A.M. Minor, W.W. Gerberich, C.B. Carter, Fracturing a nanoparticle, Philos. Mag. 87 (2007) 29-37. doi:10.1080/14786430600876585.

[66] Z.W. Shan, G. Adesso, A. Cabot, M.P. Sherburne, S.A. Syed Asif, O.L. Warren, D.C. Chrzan, A.M. Minor, A.P. Alivisatos, Ultrahigh stress and strain in hierarchically structured hollow nanoparticles, Nat. Mater. 7 (2008) 947-952. doi:10.1038/nmat2295.

[67] C.E. Carlton, P.J. Ferreira, In situ TEM nanoindentation of nanoparticles, Micron. 43 (2012) 1134-1139. doi:10.1016/j.micron.2012.03.002.

[68] F. Mompiou, D. Caillard, M. Legros, H. Mughrabi, In situ TEM observations of reverse dislocation motion upon unloading in tensile-deformed UFG aluminium, Acta Mater. 60 (2012) 3402-3414.

[69] R. Ghosh Chaudhuri, S. Paria, Core/shell nanoparticles: Classes, properties, synthesis mechanisms, characterization, and applications, Chem. Rev. 112 (2012) 2373-2433. doi:10.1021/cr100449n.

[70] L. Li, I. Etsion, A. Ovcharenko, F.E. Talke, The onset of plastic yielding in a spherical shell compressed by a rigid flat, J. Appl. Mech.-Trans. ASME. 78 (2011) 0110161-0110167. doi:10.1115/1.4001994.

[71] R. Goltsberg, I. Etsion, G. Davidi, The onset of plastic yielding in a coated sphere compressed by a rigid flat, Wear. 271 (2011) 2968-2977. doi:10.1016/j.wear.2011.06.025.

[72] X. Huang, H. Kasem, H.F. Shang, T.M. Shao, I. Etsion, Experimental study of a potential weakening effect in spheres with thin hard coatings, Wear. 296 (2012) 590-597. doi:10.1016/j.wear.2012.08.018.

[73] B. Zheng, Y.N. Wang, M. Qi, E.H. Williams, Phase boundary effects on the mechanical deformation of core/shell Cu/Ag nanoparticles, J. Mater. Res. 24 (2009) 2210-2214. doi:10.1557/jmr.2009.0263.

[74] J.E. Sader, G.V. Hartland, P. Mulvaney, Theory of acoustic breathing modes of core-shell nanoparticles, J. Phys. Chem. B. 106 (2002) 1399-1402. doi:10.1021/jp014068s.

[75] T. Still, R. Sainidou, M. Retsch, U. Jonas, P. Spahn, G.P. Hellmann, G. Fytas, The "Music" of core-shell spheres and hollow capsules: influence of the architecture on the mechanical properties at the nanoscale, Nano Lett. 8 (2008) 3194-3199. doi:10.1021/nl801500n.

[76] A. Rinaldi, M. Correa-Duarte, V. Salgueirino-Maceira, S. Licoccia, E. Traversa, A. Davila-Ibanez, P. Peralta, K. Sieradzki, Elastic properties of hard cobalt boride composite nanoparticles, Acta Mater. 58 (2010) 6474-6486. doi:10.1016/j.actamat.2010.08.009.

[77] A. Rinaldi, S. Licoccia, E. Traversa, K. Sieradzki, P. Peralta, A. Davila-Ibanez, M. Correa-Duarte, V. Salgueirino, Radial inner morphology effects on the mechanical properties of amorphous composite cobalt boride nanoparticles, J. Phys. Chem. C. 114 (2010) 13451-13458. doi:10.1021/jp102560c.

[78] W.W. Gerberich, W.M. Mook, C.R. Perrey, C.B. Carter, M.I. Baskes, R. Mukherjee, A. Gidwani, J. Heberlein, P.H. McMurry, S.L. Girshick, Superhard silicon nanospheres, J. Mech. Phys. Solids. 51 (2003) 979-992. doi:10.1016/S0022-5096(03)00018-8.

[79] W.W. Gerberich, W.M. Mook, M.J. Cordill, C.B. Carter, C.R. Perrey, J.V. Heberlein, S.L. Girshick, Reverse plasticity in single crystal silicon nanospheres, Int. J. Plast. 21 (2005) 2391-2405. doi:10.1016/j.ijplas.2005.03.001.

[80] M. Zou, D. Yang, Nanoindentation of silica nanoparticles attached to a silicon substrate, Tribol. Lett. 22 (2006) 189-196. doi:10.1007/s11249-006-9079-7.

[81] S. Vlassov, B. Polyakov, L.M. Dorogin, M. Vahtrus, M. Mets, M. Antsov, R. Saar, A.E. Romanov, A. Lhmus, R. Lhmus, Shape restoration effect in Ag-SiO_2 core-shell nanowires, Nano Lett. 14 (2014) 5201-5205. doi:10.1021/nl5019063.

[82] A. Corwin, M. De Boer, Effect of adhesion on dynamic and static friction in surface micromachining, Appl. Phys. Lett. 84 (2004) 2451-2453.

[83] K. Komvopoulos, Adhesion and friction forces in microelectromechanical systems: mechanisms, measurement, surface modification techniques, and adhesion theory, J. Adhes. Sci. Technol. 17 (2003) 477-517.

[84] Z. Burton, B. Bhushan, Hydrophobicity, adhesion, and friction properties of nanopatterned polymers and scale dependence for micro- and nanoelectromechanical systems, Nano Lett. 5 (2005) 1607-1613. doi:10.1021/nl050861b.

[85] H. Wang, M. Zou, P.R. Larson, E.S. Sanchez, K.L. Hobbs, M.E. Curtis, M.B. Johnson, O.K. Awitor, Nanomechanical properties of a Ni nanodot-patterned surface, Nanotechnology. 19 (2008). doi:10.1088/0957-4484/19/29/295708.

[86] M. Zou, L. Cai, H. Wang, D. Yang, T. Wyrobek, Adhesion and friction studies of a selectively micro/nano-textured surface produced by UV assisted crystallization of amorphous silicon, Tribol. Lett. 20 (2005) 43-52.

[87] M. Zou, L. Cai, H. Wang, Adhesion and friction studies of a nano-textured surface produced by spin coating of colloidal silica nanoparticle solution, Tribol. Lett. 21 (2006) 25-30.

[88] S.J. Park, K. Lee, D. Ko, Tribological behavior of nano-undulated surface of diamond-like carbon films, Diamond Relat. Mater. 14 (2005) 1291-1296.

[89] J.W. Yi, S.J. Park, M. Moon, K. Lee, S. Kim, Humidity effect on friction behaviors of nano-undulated diamond-like carbon films, Diamond Relat. Mater. 17 (2008) 967-971.

[90] R.A. Singh, K. Na, J.W. Yi, K. Lee, E. Yoon, DLC nano-dot surfaces for tribological applications in MEMS devices, Appl. Surf. Sci. 257 (2011) 3153-3157.

[91] M.J. Madou, Fundamentals of Microfabrication : The Science of Miniaturization, CRC Press, Boca Raton, 2002.

[92] L. Martinu, O. Zabeida, J.E. Klemberg-Sapieha, Chapter 9 - Plasma-Enhanced Chemical Vapor Deposition of Functional Coatings, in: P.M. Martin (Ed.), Handbook of Deposition Technologies for Films and Coatings (Third Edition), William Andrew Publishing, Boston, 2010, pp. 392-465.

[93] A. Fischer-Cripps, Nanoindentation, Springer-Verlag New York Inc., New York, NY, 2011.

[94] W.C. Oliver, G.M. Pharr, An Improved Technique for Determining Hardness and Elastic-Modulus using Load and Displacement Sensing Indentation Experiments, J. Mater. Res. 7 (1992) 1564-1583. doi:10.1557/JMR.1992.1564.

[95] W.C. Oliver, G.M. Pharr, Measurement of hardness and elastic modulus by instrumented indentation: Advances in understanding and refinements to methodology, J. Mater. Res. 19 (2004) 3-20.

[96] A. Fischer-Cripps, Measurement of hardness of very hard materials, Solid Mechanics and its Applications. 203 (2014) 53-62. doi:10.1007/978-94-007-6919-9-3.

[97] M. Zhao, Y. Xiang, J. Xu, N. Ogasawara, N. Chiba, X. Chen, Determining mechanical properties of thin films from the loading curve of nanoindentation testing, Thin Solid Films. 516 (2008) 7571-7580. doi:10.1016/j.tsf.2008.03.018.

[98] T.Y. Tsui, C.A. Ross, G.M. Pharr, Effects of adhesion on the measurement of thin film mechanical properties by nanoindentation, United States Dept. of Energy, Office of Energy Research. 473 (1997) 51-56.

[99] A. Strojny, X. Xia, A. Tsou, W.W. Gerberich, Techniques and considerations for nanoindentation measurements of polymer thin film constitutive properties, J. Adhes. Sci. Technol. 12 (1998) 1299-1321. doi:10.1163/156856198X00452.

[100] P. Schwaller, F. Haug, J. Michler, J. Patscheider, Nanocomposite hard coatings: Deposition issues and validation of their mechanical properties, Adv. Eng. Mater. 7 (2005) 318-322. doi:10.1002/adem.200500045.

[101] L. Shen, L. Wang, T. Liu, C. He, Nanoindentation and morphological studies of epoxy nanocomposites, Macromol. Mater. 291 (2006) 1358-1366. doi:10.1002/mame.200600184.

[102] R. Khanna, K.S. Katti, D.R. Katti, Nanomechanics of surface modified nanohydroxyapatite particulates used in biomaterials, J. Eng. Mech. 135 (2009) 468-478. doi:10.1061/(ASCE)EM.1943-7889.0000002.

[103] W.H. Roos, G.J.L. Wuite, Nanoindentation studies reveal material properties of viruses, Adv. Mater. 21 (2009) 1187-1192. doi:10.1002/adma.200801709.

[104] R.F. Gibson, A review of recent research on nanoindentation of polymer composites and their constituents, Compos. Sci. Technol. 105 (2014) 51-65. doi:10.1016/j.compscitech.2014.09.016.

[105] R.F. Cook, M.L. Oyen, Nanoindentation behavior and mechanical properties measurement of polymeric materials, Int. J. Mater. Res. 98 (2007) 370-378.

[106] O.L. Warren, S.A. Downs, T.J. Wyrobek, Challenges and interesting observations associated with feedback-controlled nanoindentation, Zeitschrift für Metallkunde. 95 (2004) 287-296.

[107] J. Chang, W. Cai, V.V. Bulatov, S. Yip, Molecular dynamics simulations of motion of edge and screw dislocations in a metal, Comput. Mater. Sci. 23 (2002) 111-115. doi:10.1016/S0927-0256(01)00221-X.

[108] G.P. Purja Pun, Y. Mishin, A molecular dynamics study of self-diffusion in the cores of screw and edge dislocations in aluminum, Acta Mater. 57 (2009) 5531-5542. doi:10.1016/j.actamat.2009.07.048.

[109] A. Simar, H.L. Voigt, B.D. Wirth, Molecular dynamics simulations of dislocation interaction with voids in nickel, Comput. Mater. Sci. 50 (2011) 1811-1817. doi:10.1016/j.commatsci.2011.01.020.

[110] M. Liao, B. Li, M.F. Horstemeyer, Unstable dissociation of a prismatic dislocation in magnesium, Scr. Mater. 69 (2013) 246-249. doi:10.1016/j.scriptamat.2013.04.008.

[111] D.E. Spearot, M.A. Tschopp, D.L. McDowell, Orientation and rate dependence of dislocation nucleation stress computed using molecular dynamics, Scr. Mater. 60 (2009) 675-678. doi:10.1016/j.scriptamat.2008.12.037.

[112] L. Capolungo, D.E. Spearot, M. Cherkaoui, D.L. McDowell, J. Qu, K.I. Jacob, Dislocation nucleation from bicrystal interfaces and grain boundary ledges: Relationship to nanocrystalline deformation, J. Mech. Phys. Solids. 55 (2007) 2300-2327. doi:10.1016/j.jmps.2007.04.001.

[113] W.G. Hoover, Canonical dynamics: Equilibrium phase-space distributions, Phys. Rev. A. 31 (1985) 1695-1697.

[114] S. Melchionna, G. Ciccotti, B. Lee Holian, Hoover NPT dynamics for systems varying in shape and size, Mol. Phys. 78 (1993) 533-544.

[115] D. Chandler, Introduction to Modern Statistical Mechanics, Oxford University Press, 1987.

[116] M.E. Tuckerman, Y. Liu, G. Ciccotti, G.J. Martyna, Non-Hamiltonian molecular dynamics: Generalizing Hamiltonian phase space principles to non-Hamiltonian systems, J. Chem. Phys. 115 (2001).

[117] S.B. Sinnott, Advances in the atomistic modeling of nanomaterials, Proc. SAMPE. (2007) 39-62.

[118] E.J. Terrell, E. Landry, A. McGaughey, C.F. Higgs III, Molecular dynamics simulation of nanoindentation, Proc. IJTC. (2009) 111-113.

[119] W. Chang, T. Fang, S. Lin, J. Huang, Nanoindentation response of nickel surface using molecular dynamics simulation, Molec. Simul. 36 (2010) 815-822. doi:10.1080/08927021003677761.

[120] J. Yang, K. Komvopoulos, A molecular dynamics analysis of surface interference and tip shape and size effects on atomic-scale friction, J. Tribol.-T. ASME. 127 (2005) 513-21. doi:10.1115/1.1843829.

[121] C.W. Yong, W. Smith, K. Kendall, Molecular dynamics simulations of (001) MgO surface contacts: effects of tip structures and surface matching, Nanotechnology. 14 (2003) 829-39. doi:10.1088/0957-4484/14/8/301.

[122] M.T. Knippenberg, P.T. Mikulski, J.A. Harrison, Effects of tip geometry on interfacial contact forces, Model. Simul. Mater. Sci. Eng. 18 (2010) 034002 (20 pp.). doi:10.1088/0965-0393/18/3/034002.

[123] U. Landman, W.D. Luedtke, Nanomechanics and dynamics of tip-substrate interactions, J. Vac. Sci. Technol. B. 9 (1991) 414-23. doi:10.1116/1.585583.

[124] T. Zhu, J. Li, K.J. Van Vliet, S. Ogata, S. Yip, S. Suresh, Predictive modeling of nanoindentation-induced homogeneous dislocation nucleation in copper, J. Mech. Phys. Solids. 52 (2004) 691-724. doi:10.1016/j.jmps.2003.07.006.

[125] D. Saraev, R.E. Miller, Atomistic simulation of nanoindentation into copper multilayers, Model. Simul. Mater. Sci. Eng. 13 (2005) 1089-1099. doi:10.1088/0965-0393/13/7/006.

[126] E.T. Lilleodden, J.A. Zimmerman, S.M. Foiles, W.D. Nix, Atomistic simulations of elastic deformation and dislocation nucleation during nanoindentation, J. Mech. Phys. Solids. 51 (2003) 901-20. doi:10.1016/S0022-5096(02)00119-9.

[127] P. Peng, G. Liao, T. Shi, Z. Tang, Y. Gao, Molecular dynamic simulations of nanoindentation in aluminum thin film on silicon substrate, Appl. Surf. Sci. 256 (2010) 6284-90. doi:10.1016/j.apsusc.2010.04.005.

[128] J.A. Zimmerman, C.L. Kelchner, P.A. Klein, J.C. Hamilton, S.M. Foiles, Surface step effects on nanoindentation, Phys. Rev. Lett. 87 (2001) 165507-1. doi:10.1103/PhysRevLett.87.165507.

[129] J.A. Zimmerman, P.A. Klein, S.M. Foiles, Effect of surface steps on dislocation structure during nanoindentation, MRS Proc. (2001) 8-8.

[130] M.S. Daw, M.I. Baskes, Embedded-atom method: Derivation and application to impurities, surfaces, and other defects in metals, Phys. Rev. B. 29 (1984) 6443.

[131] M.I. Baskes, Modified embedded-atom potentials for cubic materials and impurities, Phys. Rev. B. 46 (1992) 2727-2742.

[132] B. Jelinek, S. Groh, M.F. Horstemeyer, J. Houze, S.G. Kim, G.J. Wagner, A. Moitra, M.I. Baskes, Modified embedded atom method potential for Al, Si, Mg, Cu, and Fe alloys, Phys. Rev. B. 85 (2012) 1-18. doi:10.1103/PhysRevB.85.245102.

[133] D. Faken, H. Jónsson, Systematic analysis of local atomic structure combined with 3D computer graphics, Computational Materials Science. 2 (1994) 279-286. doi:10.1016/0927-0256(94)90109-0.

[134] C.L. Kelchner, S.J. Plimpton, J.C. Hamilton, Dislocation nucleation and defect structure during surface indentation, Phys. Rev. B. 58 (1998) 11085-8. doi:10.1103/PhysRevB.58.11085.

[135] A. Stukowski, Structure identification methods for atomistic simulations of crystalline materials, Model. Simul. Mater. Sci. Eng. 20 (2012). doi:10.1088/0965-0393/20/4/045021.

[136] A. Stukowski, V.V. Bulatov, A. Arsenlis, Automated identification and indexing of dislocations in crystal interfaces, Model. Simul. Mater. Sci. Eng. 20 (2012). doi:10.1088/0965-0393/20/8/085007.

[137] S. Plimpton, Fast Parallel Algorithms for Short-Range Molecular Dynamics, J. Comput. Phys. 517 (1995) 1-19.

[138] S.J. Cook, P. Clancy, Comparison of semi-empirical potential functions for silicon and germanium, Phys. Rev. B. 47 (1993) 7686-7699.

[139] J. Custer, M.O. Thompson, D. Jacobson, J. Poate, S. Roorda, W. Sinke, F. Spaepen, Density of amorphous Si, Appl. Phys. Lett. 64 (1994) 437-439.

[140] A. Stukowski, Visualization and analysis of atomistic simulation data with OVITO-the Open Visualization Tool, Model. Simul. Mater. Sci. Eng. 18 (2010). doi:10.1088/0965-0393/18/1/015012.

[141] A. Savitzky, M.J. Golay, Smoothing and differentiation of data by simplified least squares procedures. Anal. Chem. 36 (1964) 1627-1639.

[142] R.A. Fleming, M. Zou, The effects of confined core volume on the mechanical behavior of Al/a-Si core-shell nanostructures, Acta Mater. 128 (2017) 149-159. doi:10.1016/j.actamat.2017.02.009.

[143] J. Li, K.J. Van Vliet, T. Zhu, S. Yip, S. Suresh, Atomistic mechanisms governing elastic limit and incipient plasticity in crystals, Nature. 418 (2002) 307-310. doi:10.1038/nature00865.

[144] V. Domnich, Y. Gogotsi, S. Dub, Effect of phase transformations on the shape of the unloading curve in the nanoindentation of silicon, Appl. Phys. Lett. 76 (2000) 2214-2214. doi:10.1063/1.126300.

[145] J.S. Field, M.V. Swain, R.D. Dukino, Determination of fracture toughness from the extra penetration produced by indentation-induced pop-in, J. Mater. Res. 18 (2003) 1412-1419.

[146] C. Han, C. Huang, B. Wu, J. Lin, The nanoindentation applied to predict the interface delamination for the C/amorphous Si composite film, J. Appl. Phys. 106 (2009) 083517. doi:10.1063/1.3246618.

[147] M. Durandurdu, D. Drabold, Ab initio simulation of first-order amorphous-to-amorphous phase transition of silicon, Phys. Rev. B. 64 (2001) 014101.

[148] Y. Wang, J. Li, A.V. Hamza, T.W. Barbee Jr, Ductile crystalline-amorphous nanolaminates, Proc. Natl. Acad. Sci. U. S. A. 104 (2007) 11155-11160. doi:10.1073/pnas.0702344104.

[149] A.P. Thompson, S.J. Plimpton, W. Mattson, General formulation of pressure and stress tensor for arbitrary many-body interaction potentials under periodic boundary conditions, J. Chem. Phys. 131 (2009) 154107.

[150] H. Van Swygenhoven, M. Spaczer, A. Caro, Microscopic description of plasticity in computer generated metallic nanophase samples: a comparison between Cu and Ni, Acta Mater. 47 (1999) 3117-3126.

[151] M. Tschopp, D. McDowell, Grain boundary dislocation sources in nanocrystalline copper, Scr. Mater. 58 (2008) 299-302.

[152] V. Yamakov, D. Wolf, S. Phillpot, A. Mukherjee, H. Gleiter, Deformation-mechanism map for nanocrystalline metals by molecular-dynamics simulation, Nat. Mater. 3 (2004) 43-47.

[153] V. Yamakov, D. Wolf, S. Phillpot, A. Mukherjee, H. Gleiter, Deformation mechanism crossover and mechanical behaviour in nanocrystalline materials, Philos. Mag. Lett. 83 (2003) 385-393.

[154] R.A. Fleming, J.A. Goss, M. Zou, Material dimensionality effects on the nanoindentation behavior of Al/a-Si core-shell nanostructures, Appl. Surf. Sci. 412 (2017) 96-104. doi:10.1016/j.apsusc.2017.03.221.

[155] R.A. Fleming, M. Zou, Nanostructure-Textured Surfaces with Low Friction and High Deformation Resistance, Tribol. Trans. (2016) 1-8. doi:10.1080/10402004.2016.1274066.

[156] V. Popov, Contact Mechanics and Friction: Physical Principles and Applications, Springer Science & Business Media, 2010.

[157] C. Li, Y. Yamauchi, Facile solution synthesis of Ag@Pt core–shell nanoparticles with dendritic Pt shells, Phys. Chem. Chem. Phys. 15 (2013) 3490-3496.

[158] C.C. Crane, F. Wang, J. Li, J. Tao, Y. Zhu, J. Chen, Synthesis of Copper-Silica Core-Shell Nanostructures with Sharp and Stable Localized Surface Plasmon Resonance, J. Phys. Chem. C. 121 (2017) 5684-5692. doi:10.1021/acs.jpcc.6b11891.

[159] R.E. Miller, L.E. Shilkrot, W.A. Curtin, A coupled atomistics and discrete dislocation plasticity simulation of nanoindentation into single crystal thin films, Acta Mater. 52 (2004) 271-284. doi:10.1016/j.actamat.2003.09.011.

[160] B. Shiari, R.E. Miller, W.A. Curtin, Coupled atomistic/discrete dislocation simulations of nanoindentation at finite temperature, J. Eng. Mater. Tech. 127 (2005) 358-368.

[161] X. Li, B. Bhushan, A review of nanoindentation continuous stiffness measurement technique and its applications, Mater. Charact. 48 (2002) 11-36.

APPENDIX I: EXAMPLE LAMMPS INPUT SCRIPTS

The following LAMMPS script files were used to perform molecular dynamics nanoindentation simulations on CSNs, CSRs, and Al nanodots in this study. The various input parameters can be adjusted to simulate different structure geometries (e.g., core diameter, nanorod length, etc.), system temperatures, and indentation rates and depths. The MEAM potential files 'meam.meamf' and 'meam.alsimgcufe' were obtained from the NIST Interatomic Potential Repository (https://www.ctcms.nist.gov/potentials/). The simulations performed in this study were run primarily on the stable LAMMPS release dated June 28, 2014.

CSN Script:

```
########################################
log      CSN.log
# 3d Al/a-Si Hemispherical Core-Shell Structure

units           metal
boundary        p m p
atom_style      atomic
processors      * 1 *

# Define Variables for Geometry and Simulation Parameters
variable        Base equal 10.0                                 # Base Height in Angstroms
variable        Radius equal 100                                # Metal Core Radius in Angstroms
variable        Thick equal 100                                 # Shell Thickness in Angstroms
variable        Lat equal 4.05          # Lattice parameter of the Base Material in Angstroms
variable        Sim equal floor((3*(${Radius}+${Thick}))/${Lat})*${Lat}          # Size of
Simulation Cell in Angstroms
variable        IndentR equal 1000                  # Radius of Spherical Indenter in Angstroms
variable        IRate equal 0.5                     # Indent Rate in Angstroms/1000 timesteps
variable        t equal 300                         # Desired Simulation Temperature

# Create Simulation Box with FCC Al Lattice
lattice         fcc ${Lat}
region          box block 0 ${Sim} 0 ${Sim} 0 ${Sim} units box
create_box      3 box

# Al-Si MEAM Parameters from Jelinek et al.
pair_style      meam
pair_coeff      * * meam.meamf AlS SiS MgS CuS FeS meam.alsimgcufe AlS AlS SiS
```

```
# Define Regions for Al Core and Rigid Substrate
region          base block INF INF INF ${Base} INF INF units box
region          above-base block INF INF INF ${Base} INF INF side out units box
region          core-sphere sphere $(v_Sim/2) ${Base} $(v_Sim/2) ${Radius} units box
region          core intersect 2 core-sphere above-base
# Create Atoms and Groups for Al Structure
create_atoms    1 region core
create_atoms    2 region base
group           core region core
group           base region base

# Change Lattice to Si
lattice         diamond         5.43

# Define Regions for Si Shell
region          shell block INF INF ${Base} $(v_Base+v_Thick) INF INF units box
region          core-void sphere $(v_Sim/2) ${Base} $(v_Sim/2) ${Radius} side out units box
region          shell-skirt intersect 2 shell core-void
region          above-skirt block INF INF INF $(v_Base+v_Thick) INF INF side out units box
region          shell-sphere sphere $(v_Sim/2) ${Base} $(v_Sim/2) $(v_Radius+v_Thick) units
box
region          shell-cap intersect 3 shell-sphere above-skirt core-void
region          shell-structure union 2 shell-cap shell-skirt

# Create Atoms and Group for Si Shell
create_atoms    3 region shell-structure
group           shell-structure-cr region shell-structure       # Creates a shell of crystalline Si
variable        NumAtoms equal count(shell-structure-cr)    # Calculates the number of atoms in
the crystalline shell
create_atoms    3 random ${NumAtoms} 25  shell-structure
group           shell-structure region shell-structure
delete_atoms    group shell-structure-cr
group           shell-structure-cr delete

# Delete atoms that are too close in the a-Si shell
delete_atoms    overlap 1.5 shell-structure shell-structure

# Shift processor grid for increased efficiency
balance         1.1 shift xz 5 1.0

# Screen and file output
thermo          10
thermo_style    custom step ke pe etotal temp fmax fnorm
compute         csym all centro/atom fcc
compute                 pnrg all pe/atom
dump            cg all custom 1000 CSN.min id type x y z c_csym c_pnrg
```

```
# Freeze the lower layer of the substrate
fix                 1 base setforce 0.0 0.0 0.0


# Minimize total structure
min_style       cg
min_modify      line backtrack
minimize        1.0e-6 1.0e-8 3000 100000
undump                  cg

# Delete atoms that are too close at core/shell interface
delete_atoms    overlap 2.0 shell-structure core
delete_atoms    overlap 2.0 shell-structure base

# Equilibrate to Desired Temperature
velocity        all create $t 239427349 dist gaussian
velocity        base set 0.00 0.00 0.00 units box
fix             2 all nvt temp $t $t 0.05

# Output commands
thermo          200
thermo_style    custom step ke pe etotal temp
thermo_modify           lost warn flush yes
dump            1 all custom 2000 CSN.eqil id type x y z c_csym c_pnrg

# Run Equilibration
reset_timestep 0
run             30000
undump          1

# Indent
variable        YMax equal bound(all,ymax)
variable        Iy0 equal (${YMax}+${IndentR})
#variable       YMax delete
variable        y equal ${Iy0}+1-${IRate}*step*dt
fix             3 all indent 10 sphere $(v_Sim/2) v_y $(v_Sim/2) ${IndentR} units box

compute         strs core stress/atom NULL
compute         s11 core reduce sum c_strs[1]
compute         s22 core reduce sum c_strs[2]
compute         s33 core reduce sum c_strs[3]
compute         s12 core reduce sum c_strs[4]
compute         s13 core reduce sum c_strs[5]
compute         s23 core reduce sum c_strs[6]
```

```
thermo          500
thermo_style    custom step temp pe v_y f_3[1] f_3[2] f_3[3] c_s11 c_s22 c_s33 c_s12 c_s13
c_s23
thermo_modify   lost warn flush yes
reset_timestep 0
dump            2 all custom 2000 CSN.indent id type x y z c_csym c_pnrg c_strs[1] c_strs[2]
c_strs[3] c_strs[4] c_strs[5] c_strs[6]
run             162000
undump 2

# Retract Indenter
dump            3 all custom 2000 CSN.retract id type x y z c_csym c_pnrg c_strs[1] c_strs[2]
c_strs[3] c_strs[4] c_strs[5] c_strs[6]
variable        y0 equal $y
variable        y delete
variable        y equal ${y0}+${IRate}*elapsed*dt
run             162000
##########################################
```

CSR Script:

```
##########################################
log             CSR.log
# 3d Al/a-Si Core-Shell Rod Structure

units           metal
boundary        p m p
atom_style      atomic
processors      * 1 *

# Define Variables for Geometry and Simulation Parameters
variable        Base equal 10.0                 # Base Height in Angstroms
variable        Length equal 100                # Length of Rod (minus caps) in Angstroms
variable        Radius equal 100                # Radius of Rod Caps in Angstroms
variable        Thick equal 100                 # Shell Thickness in Angstroms
variable        Lat equal 4.05          # Lattice parameter of the Base Material in Angstroms
variable        MaxDim equal 3*(${Radius}+${Thick})+${Length}
variable        Sim equal floor((${MaxDim}/${Lat}))*${Lat}      # Size of Simulation Cell in
Angstroms
variable        IndentR equal 1000              # Radius of spherical Indenter in Angstroms
variable        IRate equal 0.5                 # Indent rate in Angstroms/1000 timesteps
variable        t equal 300                     # Desired Simulation Temperature

# Create Simulation Box with FCC Al Lattice
lattice         fcc ${Lat}
region          box block 0 ${Sim} 0 ${Sim} 0 ${Sim} units box
```

```
create_box      3 box

# Al-Si MEAM Parameters from Jelinek et al.
pair_style      meam

pair_coeff      * * meam.meamf AlS SiS MgS CuS FeS meam.alsimgcufe AlS AlS SiS

# Define Regions for Al Core and Rigid Substrate
region          base block INF INF INF ${Base} INF INF units box
region          above-base block INF INF INF ${Base} INF INF side out units box
region          core-cyl cylinder x ${Base} $(v_Sim/2) ${Radius} $(v_Sim/2-v_Length/2)
$(v_Sim/2+v_Length/2) units box
region          core-shaft intersect 2 core-cyl above-base
region          LofCyl block INF $(v_Sim/2-v_Length/2) ${Base} INF INF INF units box
region          RofCyl block $(v_Sim/2+v_Length/2) INF ${Base} INF INF INF units box
region          LCap-sphere sphere $(v_Sim/2-v_Length/2) ${Base} $(v_Sim/2) ${Radius} units
box
region          RCap-sphere sphere $(v_Sim/2+v_Length/2) ${Base} $(v_Sim/2) ${Radius}units
box
region          LCap intersect 2 LofCyl LCap-sphere
region          RCap intersect 2 RofCyl RCap-sphere
region          core union 3 core-shaft LCap RCap

# Create Atoms and Groups for Al Structure
create_atoms    1 region core
create_atoms    2 region base
group           core region core
group           base region base

# Change Lattice to Si
lattice         diamond         5.43

# Define Regions for Si Shell
region          shell block INF INF ${Base} $(v_Base+v_Thick) INF INF units box
region          core-void union 3 core-shaft LCap RCap side out
region          shell-skirt intersect 2 shell core-void
region          above-skirt block INF INF INF $(v_Base+v_Thick) INF INF side out units box
region          shell-cyl cylinder x ${Base} $(v_Sim/2) $(v_Radius+v_Thick) $(v_Sim/2-
v_Length/2) $(v_Sim/2+v_Length/2) units box
region          LofCyl-shell block INF $(v_Sim/2-v_Length/2) $(v_Base+v_Thick) INF INF
INF units box
region          RofCyl-shell block $(v_Sim/2+v_Length/2) INF $(v_Base+v_Thick) INF INF
INF units box
region          LCap-shell-sphere sphere $(v_Sim/2-v_Length/2) ${Base} $(v_Sim/2)
$(v_Radius+v_Thick) units box
```

```
region          RCap-shell-sphere sphere $(v_Sim/2+v_Length/2) ${Base} $(v_Sim/2)
$(v_Radius+v_Thick) units box
region          LCap-shell intersect 2 LofCyl-shell LCap-shell-sphere
region          RCap-shell intersect 2 RofCyl-shell RCap-shell-sphere
region          shell-cylinder union 3 shell-cyl LCap-shell RCap-shell
region          shell-cap intersect 3 shell-cylinder above-skirt core-void
region          shell-structure union 2 shell-cap shell-skirt

# Create Atoms and Group for Si Shell
create_atoms   3 region shell-structure
group          shell-structure-cr region shell-structure        # Creates a shell of crystalline Si
variable       NumAtoms equal count(shell-structure-cr)   # Calculates the number of atoms in
the crystalline shell
create_atoms   3 random ${NumAtoms} 25  shell-structure
group          shell-structure region shell-structure
delete_atoms   group shell-structure-cr
group          shell-structure-cr delete

# Delete atoms that are too close in the a-Si shell
delete_atoms   overlap 1.5 shell-structure shell-structure

# Shift processor grid for increased efficiency
balance        1.1 shift xz 5 1.0

# Screen and file output
thermo         10
thermo_style    custom step ke pe etotal temp fmax fnorm
compute        csym all centro/atom fcc
compute        pnrg all pe/atom
dump           cg all custom 1000 CSR.min id type x y z c_csym c_pnrg

# Freeze the lower layer of the substrate
fix            1 base setforce 0.0 0.0 0.0

# Minimize total structure
min_style      cg
min_modify     line backtrack
minimize       1.0e-6 1.0e-8 3000 100000
undump         cg

# Delete atoms that are too close at core/shell interface
delete_atoms    overlap 2.0 shell-structure core
#delete_atoms    overlap 2.0 shell-structure base

# Equilibrate to Desired Temperature
velocity       all create $t 239427349 dist gaussian
```

```
velocity        base set 0.00 0.00 0.00 units box
fix             2 all nvt temp $t $t 0.05

# Output commands
thermo          200
thermo_style    custom step ke pe etotal temp
thermo_modify           lost warn flush yes
dump            1 all custom 2000 CSR.eqil id type x y z c_csym c_pnrg

# Run Equilibration
reset_timestep 0
run             20000
undump                  1

# Indent
variable        YMax equal bound(all,ymax)
variable        Iy0 equal (${YMax}+${IndentR})
#variable       YMax delete
variable        y equal ${Iy0}+1-${IRate}*step*dt
fix             3 all indent 10 sphere $(v_Sim/2) v_y $(v_Sim/2) ${IndentR} units box
thermo          500
thermo_style    custom step temp pe v_y f_3[1] f_3[2] f_3[3]
thermo_modify   lost warn flush yes
reset_timestep 0
dump            2 all custom 2000 CSR.indent id type x y z c_csym c_pnrg
run             162000

# Retract Indenter
variable        y0 equal $y
variable        y delete
variable        y equal ${y0}+${IRate}*elapsed*dt
run             162000
########################################
```

Al Nanodot Script:

```
########################################
log             AlND.log
# 3d Al Hemispherical Nanodot
units           metal
boundary        p m p
atom_style      atomic
processors      * 1 *

# Define Variables for Geometry and Simulation Parameters
variable        Base equal 10           # Base Height in Angstroms
```

```
variable        Radius equal 100        # Metal Core Radius in Angstroms
variable        Lat equal 4.05          # Lattice parameter of the Base Material in Angstroms
variable        Sim equal floor((4*${Radius})/${Lat})*${Lat}       # Size of Simulation Cell in
Angstroms
variable        IndentR equal 1000      # Radius of spherical Indenter in Angstroms
variable        IRate equal 0.5         # Indent rate in Angstroms/1000 timesteps
variable        t equal 300             # Desired Simulation Temperature

# Create Simulation Box with FCC Al Lattice
lattice         fcc ${Lat}
region          box block 0 ${Sim} 0 ${Sim} 0 ${Sim} units box
create_box      3 box

# Al-Si MEAM Parameters from Jelinek et al.
pair_style      meam
pair_coeff      * * meam.meamf AlS SiS MgS CuS FeS meam.alsimgcufe AlS AlS SiS

# Define Regions for Al Core and Rigid Substrate
region          base block INF INF INF ${Base} INF INF units box
region          above-base block INF INF INF ${Base} INF INF side out units box
region          core-sphere sphere $(v_Sim/2) ${Base} $(v_Sim/2) ${Radius} units box
region          core intersect 2 core-sphere above-base

# Create Atoms and Groups for Al Structure
create_atoms    1 region core
create_atoms    2 region base
group           core region core
group           base region base

# Shift processor grid for increased efficiency
balance         1.1 shift xz 5 1.0

# Screen and file output
thermo          10
thermo_style    custom step ke pe etotal temp fmax fnorm

compute                 csym all centro/atom fcc
compute                 pnrg all pe/atom
dump            cg all custom 1000 AlND.min id type x y z c_csym c_pnrg

# Freeze the lower layer of the substrate
fix             1 base setforce 0.0 0.0 0.0

# Minimize total structure
min_style       cg
min_modify      line backtrack
```

```
minimize        1.0e-6 1.0e-8 3000 100000
undump                  cg

# Equilibrate to Desired Temperature
velocity        all create $t 39427349 dist gaussian
velocity        base set 0.00 0.00 0.00 units box
fix     2 all nvt temp $t $t 0.05

# Output commands
thermo          200
thermo_style    custom step ke pe etotal temp
thermo_modify           lost warn flush yes
dump            1 all custom 1000 AlND_10_1B.eqil id type x y z c_csym c_pnrg

# Run simulation
reset_timestep 0
run             30000
undump                  1

# Indent
variable        YMax equal bound(all,ymax)
variable        Iy0 equal (${YMax}+${IndentR})
#variable       YMax delete
variable        y equal ${Iy0}+1-${IRate}*step*dt
fix             3 all indent 10 sphere $(v_Sim/2) v_y $(v_Sim/2) ${IndentR} units box

compute         strs core stress/atom NULL
compute         s11 core reduce sum c_strs[1]
compute         s22 core reduce sum c_strs[2]
compute         s33 core reduce sum c_strs[3]
compute         s12 core reduce sum c_strs[4]
compute         s13 core reduce sum c_strs[5]
compute         s23 core reduce sum c_strs[6]

thermo          500
thermo_style    custom step temp pe v_y f_3[1] f_3[2] f_3[3] c_s11 c_s22 c_s33 c_s12 c_s13
c_s23
thermo_modify   lost warn flush yes
reset_timestep 0
dump            2 all custom 2000 AlND.indent id type x y z c_csym c_pnrg c_strs[1] c_strs[2]
c_strs[3] c_strs[4] c_strs[5] c_strs[6]

run             42000
undump          2

# Retract Indenter
```

```
dump            3 all custom 2000 AlND.retract id type x y z c_csym c_pnrg c_strs[1] c_strs[2]
c_strs[3] c_strs[4] c_strs[5] c_strs[6]
variable        y0 equal $y
variable        y delete
variable        y equal ${y0}+${IRate}*elapsed*dt
run             72000
########################################
```